Electronic Theses and Dissertations   Graduate School

2019

Hydrophobization of Cellulose-Based Fibers for Packaging Applications with Alkyl Ketene Dimers (AKD) and Food-Grade Waxes via Supercritical Impregnation with Carbon Dioxide – Experimental and Thermodynamic Modeling Approaches

Kolawole Adenekan
University of Mississippi

Follow this and additional works at: https://egrove.olemiss.edu/etd

Part of the Chemical Engineering Commons

HYDROPHOBIZATION OF CELLULOSE-BASED FIBERS FOR PACKAGING

APPLICATIONS WITH ALKYL KETENE DIMERS (AKD) AND FOOD-GRADE WAXES

VIA SUPERCRITICAL IMPREGNATION WITH CARBON DIOXIDE – EXPERIMENTAL

AND THERMODYNAMIC MODELING APPROACHES

A Dissertation
presented in partial fulfillment of requirements
for the degree of Doctor of Philosophy
in the Department of Chemical Engineering
The University of Mississippi

by

KOLAWOLE ADENEKAN

May 2019

ABSTRACT

In this study, a combination of thermodynamic modeling and experimental investigation of novel high-pressure impregnation technique were used to create thin films of sizing agents with evenly developed hydrophobicity across the entire thickness of cellulose substrates. In addition to the viability of this common sizing agent, alkyl ketene dimer (AKD), green-based edible waxes (carnauba wax and beeswax) were also assessed as prospects for food-based applications.

A thermodynamic solubility modeling was carried out using the group contribution estimation methods (GCEM) with Peng-Robinson equation of state to gain insights on the optimal regions of enhanced solvating strength of the high-pressure treatments. The modeling showed that there was a significant increase in solubility at lower temperatures (retrograde vaporization) with operating pressures less than the crossover pressure – and with operating pressures higher than the crossover pressure, solubility increased at higher temperatures.

Impregnation of cellulose-based materials with AKD dissolved in n-heptane cosolvent and supercritical carbon dioxide ($scCO_2$), over a wide range of pressures at room temperature, produced a microporous and highly hydrophobic surface with an average CA of $140 \pm 5^{\circ}$. The best hydrophobic performance was found in the region of optimal $scCO_2$ solubility between 100 and 200 bar, and achieved hydrophobic conditions quicker than those at higher and lower impregnation pressures. The surfaces were found to exhibit sticky hydrophobicity after long times since impregnation. The sizing was due to the spreading of AKD across the fiber surface and interactions with the cellulose substrate via hydrogen-bonding. There was little evidence of reaction-based

sizing from FTIR analyses, as the characteristic ketone and ester peaks indicating reaction between AKD and cellulose were not observed.

For food-grade waxes, annealing was used to augment the high-pressure impregnation (200 bar and 22°C) treatments – it lowered the surface energy and increased the roughness profile of the surface. After impregnation, the treated substrates were annealed at 80, 110, 140 and 165°C. The melting and recrystallization of the different components making up the wax caused formation of hierarchical microstructures which further improved the hydrophobicity of the surface via phase separation. Significant increases in hydrophobic properties were observed between 110 and 165°C. Two patterns of hydrophobic development were observed with the food-grade waxes – freshly impregnated annealed at higher temperatures produced a more stable and higher hydrophobicity, and delayed annealing enabled higher hydrophobicity at lower temperatures. The impregnation treatment offered a better resistance to mechanical wear and improved the mechanical robustness (more than five times) of the substrates due to strengthening of the inter- and intra-fiber bonding. This modified material has applications in food packaging, where frequently water-repellant surfaces are required. This method is preferable to traditional coating methods because it sizes across the entire thickness of the substrate rather than just the surface and can be used for non-planar surfaces; uses significantly less material than traditional methods and will be an excellent technique for multilayered and intelligent coating.

DEDICATION

For Gary and Perri Robinette, and Jon and Mary Kangas

ACKNOWLEDGEMENTS

Xiaobing Li of the Jackson Avenue Center for his assistance in training and conducting various mechanical and thermal testing, both from the University of Mississippi.

My first and last roommate in Oxford, Mississippi, Stephen Paul Frye, whose genuine heart replete with love and kindness is second to none. In you, I have not found only a precious friend but also a wonderful brother that will always have my best interest at heart. Another kind of Stephen (and vice-versa) that I encountered here is William Reed Davis, a wonderful guy that I believe is very rare to find. I am always blown away by how much loving you are – which I have both felt, experienced and touched for all these years. And thank you for introducing me to the wonderful Davis family – you all will remain indelible in my heart.

What an irreparable loss will it be to me if I never met Rose Adeola during my program in Oxford? You are simply phenomenal and have impacted every atom of my being. Thanks for your persistent encouragements and unceasing prayers – I am sure that without them things would not have gone the way they did. No doubt, time and space will fail me to painstakingly chronicle the place and role of Osariemen "Osas" Damilola Imafidon in my program as well as my entire life. Osas has reached a place in my heart that is exclusively reserved for selected few. Thank you for having a heart large enough and a memory sufficiently perceptible to remember my deadlines and schedules alongside her crazily demanding chemical engineering classes. It will be nothing shy of a flagrant misnomer if I skip mentioning Angela Jibola Fasuyi. Being around you is very contagiously encouraging as it regards what the future holds

TABLE OF CONTENTS

LIST OF FIGURES

LIST OF TABLES

CHAPTER I

INTRODUCTION

1.1 Introduction

Cellulose paper is one of the commonest materials in everyday life [1]. It is used for everyday printing purposes to packaging materials for gift items and various wrappings but is very hydrophilic in nature due many hydroxy groups in its structure [1,2]. These potential applications are limited by its water-loving tendency. Cellulose papers are usually coated or modified during or after the paper-making process to possess desirable functionalities. The subject of coating is familiar to many – hardly is there any material that is not coated with another material for enhanced or additional functionalities [3]. No matter the mode or type of coating technique employed, the central reason is to add special desirable functionalities to a material (called a substrate in coating science). Coatings have been used for aesthetic purposes; to add enhanced functionalities such as water-repellency to a material surface; to improve the mechanical durability of a surface, inclusion of anti-microbial functionality and thermal resistive applications [4–8]. However, there a number of drawbacks and limitations in the existing method such as uneven coating distribution, use of fluorochemicals, and excessive consumption of sizing chemicals that may be very expensive [2,9].

In this study, the application of coating for water-repellent functionality on cellulose-based materials (CBM) was explored. Specifically, the high-pressure impregnation of AKD (alkyl ketene dimer) and other food-grade waxes (beeswax and carnauba wax) dissolved in supercritical carbon dioxide (scCO$_2$) was the coating technique used to modify cellulose fiber substrates. In some cases, especially with the food-grade waxes, additional annealing treatment was used to improve the hierarchical micro-/nano-structures which are critical in enhancing water-repellency (superhydrophobicity) [10]. Also, a thermodynamic simulation was developed to gain better insight of high-pressure phase equilibria of AKD in CO$_2$ [11].

The following physical and chemical characterizations were conducted to assess the hydrophobic performance other functionalities (including mechanical robustness) of the surfaces:

- scanning electron microscope (SEM) with image analysis using ImagePro
- Fourier Transform Infrared Spectroscopy (FTIR)
- Contact angle (CA) analysis
- Atomic Force Microscopy (AFM)
- Dynamic mechanical and thermal analysis (DMTA)

It is believed that the findings in this study will significantly contribute to the growing efforts in using high-pressure impregnation methods as alternatives to traditional coating techniques [9,12–14]. This study also includes the use of high-pressure impregnation to impart additional functionalities such as mechanical durability, but the primary focus is water-repellency for paper and packaging applications.

The remainder of this chapter will discuss key concepts related to this investigation.

1.2 Superhydrophobicity

Superhydrophobicity had been a subject of research since the early 1900s but has only received more attention recently due to its multifunctional purposes and diverse applications [2,15–20], which include – but are not limited to – self-cleaning, dust-removing, self-healing, wall-climbing, anti-sticking and anti-microbial surfaces [2,10,21–27]. Superhydrophobic coatings have also been found to offer excellent resistance to corrosion activities [28–30]. Two types of water repellency found in nature are roll-off (exhibited by lotus leaves) [2,31–33] hydrophobicity and sticky (observed in rose petals) [2,22] hydrophobicity. Techniques used to produce superhydrophobic surfaces mimic these natural phenomena, and have been successfully created on different surfaces, ranging from paper to durable metallic surfaces [3,34,35]. Most superhydrophobic methods cannot be applied on CBM due to their chemical properties such as hydrophilicity, hygroscopicity and flexibility [1,2,36–40]. Mechanical properties of paper are likely to be affected during hydrophobization processes, and durability is always a major factor to be considered in the fabrication of superhydrophobicity [5,6].

The behavior of water droplets on CBM reveals a lot of information about its texture, chemistry, morphology and geometric structure of the surface [41]. The ease of modification of surface wetting characteristics is a desirable property of CBM because it enhances its functionality [2]. The wettability of a surface in contact with water is governed by many models [42], the three most popular ones are Young, Wenzel, and Cassie-Baxter, depending on the nature of the surface [3,43].

Young's model, given by **Equation 1.1** [44–46], describes the hypothetical behavior of water on a smooth surface. CA is denoted by θ, and γ_{SV}, γ_{SL}, and γ_{LV} are interfacial tensions developed between solid-vapor, solid-liquid and liquid-vapor interfaces, respectively.

$$cos\theta = \frac{\gamma_{SV} - \gamma_{SL}}{\gamma_{LV}} \tag{1.1}$$

Young's model is not sufficient to describe droplet behavior on rough surfaces [30]. A modified version of Young's model, called Wenzel's model, developed in 1936, depicts droplet behavior on rough surfaces more accurately than Young's model [3,30]. Wenzel model (**Equations 1.2 and 1.3**) is given as follows:

$$cos\theta_w = rcos\theta \tag{1.2}$$

Equation 2 above is called Wenzel's model. θ_w is the Wenzel's contact angle on a rough surface, and r is the dimensionless roughness factor (defined by the ratio of the actual area of a rough surface to its flat projected area). Contact angle on a flat surface is denoted by θ_0.

$$r = \frac{\text{actual area of a rough surface}}{\text{flat projected area}} \tag{1.3}$$

4

Cassie and Baxter in 1944 [30] proposed a model that describes droplet behavior on a rough, heterogeneous surface. The surface has two fractional areas; one is occupied by the material of the surface other than by air. The contact angle made on a such a surface is given by **Equations 1.4**.

$$cos\theta = rcos\theta_0 - f(rcos\theta_0 + 1) \tag{1.4}$$

Where r is the dimensionless roughness factor as defined in Equation 3, f is the fractional area occupied by the solid-liquid interface, θ is the contact angle made on a rough heterogeneous surface θ_0 and is the contact angle made on a flat smooth surface. When the surface is completely liquid-filled, $f = 1$. This leads to an absence of liquid-air interface – at this limiting condition, the Cassie-Baxter equation becomes Wenzel equation.
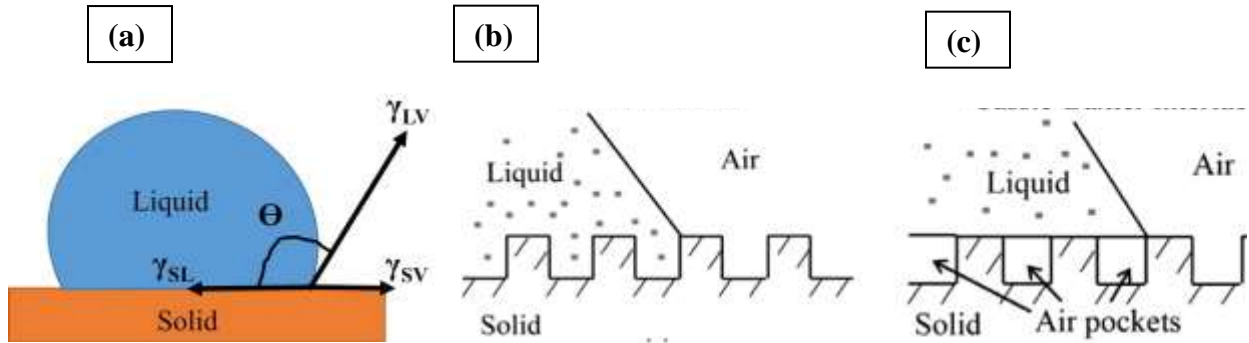
Figure 1.1: Surfaced described by (a) Young interface (b) Wenzel interface (c) Cassie-Baxter interface [3,30].

The technique for fabrication of superhydrophobicity aims at reducing the surface energy by adding low surface energy substances such as waxes and fluorinated compounds [2,10,31,47] and/or increasing the roughness of the surface. Existence of hierarchical micro-/nano-structures on a surface promotes the development of superhydrophobicity [2,10,21,22,29,48]. Deposition of nanoparticles on surfaces have also been reported to promote the dual-scale roughness which imparts excellent water repellency characteristics on the surfaces [15,41,48–52].

Hydrophobic properties of a surface are determined by measuring the CA, contact angle hysteresis (CAH) and sliding angle (SA) of the droplet on the surface [1,44,53–59]. CAs are used to categorize the degree of wetting of a material in contact with water [9,10,13]. A material that has a water CA less than 90° is hydrophilic, and water spreads and wets the surface quickly. The material is "hydrophobic" if the angle ranges between 90 and 150°, where a water droplet does not immediately spread on the surface [10]. A superhydrophobic surface has a CA of 150° and above. If the water droplet rolls off the surface, this is also called a self-cleaning surface, demonstrating the "lotus effect" as described previously [10,16]. For the superhydrophobic requirement to be fully met, the CAH < 10° and SA < 5°. [54,60,61]. If CAH > 10°, SA >> 5°, and CA near but less than 150°, the droplet is likely to be glued to the surface [22,57,60,62], and comes under the sticky hydrophobicity classification.

Droplets that display sticky or roll-off behavior on/from surfaces are governed by two adhesion forces– lateral (F_L) and retentive (F_R) [22,54,63,64]. When a droplet sticks to a surface like that of rose petals, a retentive force of adhesion is developed, and will be counteracted by a lateral force of adhesion. The droplet sticks and stays on a surface until the $F_L \geq F_R$ [22]. The lateral force of

adhesion generates metastable energy and retentive force of adhesion generates barrier energy [22,54,63–65]. Metastable energy is the energy that enhances the ease of movement of a droplet laterally across a surface. Barrier energy is the energy that restricts and binds a droplet to "stick" to a surface. **Equations 1.5 and 1.6** for calculating F_L and F_R [22,62–64], respectively, are given as follows:

$$F_L = \rho g V \, sin\alpha \tag{1.5}$$

$$F_R = kR\gamma_{LV}(cos\theta_r - cos\theta_a) \tag{1.6}$$

where R is the characteristic length representing the shape and size of the droplet; k is a constant of proportionality; γ_{LV} is the interfacial tension between the droplet and the air; θ_a is the advancing CA; θ_r is the receding CA.

1.3 Sizing chemicals

The word "sizing", as used by paper industries, usually refers to two phenomena; one is enhancing the slurry of the paper fibers to be water-resistant and the other is addition of a viscous solution to the surface of paper to enhance its hydrophobicity [66–68]. To clear the ambiguity, the paper and packaging industries generally refer to the slurry enhancement as "internal sizing" while the latter is termed "surface sizing" [6,66,69,70]. The main internal sizing chemicals currently in use around

the world are emulsion-based [66,71,72]. Irrespective of the sizing agent used, the aim is to retain

hydrophobic molecules in the sheet of the paper. Surface sizing aims at imparting additional water-

repellency to the internally sized paper – which establishes a hindrance toward penetration and

spreading of the liquids through the porous structure of paper. Some of the sizing chemicals,

commonly used in paper and packaging industries, are discussed briefly below:

The use of *rosin* to internally size paper dates back several decades according to Hubbe [66]. Rosin

is one of the byproducts of distillation of wood chips, made by kraft pulping processes under

alkaline conditions. Rosin is a mixture of abietic acid ($C_{20}H_{30}O_2$) and other similar wood

components [66]. Abietic acid has three six-membered rings joined together. The hydrophobic

nature of rosin is due to the fact that the rings contain only carbon and hydrogen [66].

AKD is the commonest and most widely used sizing agent in paper and packaging industries

[9,71–77]. AKD ($C_{38}H_{72}O_2$) is a crystallizing wax and has two alkyl groups with 14 and 20 carbons

respectively [13]; its melting point is between 40 and 60 ^{o}C [78–81], depending on the chain length

of the dimers. AKD can size under neutral [73] or alkaline conditions [9], and is also less reactive

towards cellulose [9,71]. AKD may take up to two weeks to develop sufficient sizing [9,77], and

has also been used together with other substances that are not intrinsically hydrophobic by

themselves, such as starch [82,83]. Starch has affinity for water but its desirable property as a

renewable organic makes it a good additive. Starch is one of the best candidates of organic fillers

to replace inorganic fillers in paper, and it can also be used on its own as a surface agent [83].

AKD has been used to tune the hydrophobicity of starch microcellular foam particles added on

paper [70,83,84]. The addition of AKD to starch improves the performance and functionality to the paper [83,85].

Paraffin wax, ever since its discovery in 1830, has been used for a number of industrial and domestic applications ranging from illuminant materials to electrical conductors [86]. Paraffin wax is also known to exhibit resistance to water penetration and proofing characteristics for porous materials [86]. Paraffin waxes are mixtures of saturated straight-chain hydrocarbons. Solid alkanes are generally referred to as paraffin waxes [87]. They are excellent substances for phase change applications such as thermal storage materials and cooling devices in electronic gadgets [88]. Their properties vary with chemical compositions, which could range from 10 to more than 30 carbon atoms with a melting point between 46 and 68 $^{\circ}$C [89].

The need to make materials green and sustainable has popularized the use of *beeswaxes* in the food packaging industries [90]. In addition to beeswax exceptional antimicrobial properties, it also offers very strong resistance to water and water vapor penetration [90]. Beeswax is made of different natural components, consisting mainly of long chain alcohols, fatty acids and ester compounds [90]. Beeswax is becoming a favorite sizing chemical in food packaging industries and offers great prospects for other industries such as pharmaceuticals, pulp and paper, and cosmetics, due to its excellent properties [90].

1.4 Supercritical fluids applications

The use of supercritical fluids (SCF) for several chemical processes is a well-known alternative practice in some chemical industries and research communities [91,92,101–103,93–100]. Their applications extend to pharmaceuticals, pulp and paper, oil and gas, food processing, and chemical processes [13,98,99,104–109]. SCF exist at temperatures and pressures above their critical points. They possess high densities close to those of liquids, gas-like viscosities, low surface tension and very high diffusion coefficients, resulting in more efficient mass transfer and higher solvating power [9,93,114–117,95,96,106,107,110–113]. SCFs also offer new pathways to sustainable technologies [110]. Solubility increases with density and pressure – thus, SCF have high absorption capacity [93]. The unusually high mass transfer rates between a solute and a SCF are owing to their gas-like properties [93].

Table 1.1: Critical properties of various solvents [93]

Solvent	Molecular weight (g/mol)	Critical temperature (K)	Critical pressure (atm)	Critical density (g/cm^3)
CO_2	*44.01*	*304.1*	*72.8*	*0.469*
Water	18.015	647.096	217.755	0.322
Methane	16.04	190.4	45.4	0.162
Propane	44.09	369.8	41.9	0.217
Propylene	42.08	364.9	45.4	0.232
Ethanol	46.07	513.9	60.6	0.276
Acetone	58.08	508.1	46.4	0.278

The use of SCF in various chemical processes such as purification, recrystallization and environmental mitigation, has reduced or eliminated the use of organic solvents [93]. As compiled by Nautiyal [93], **Table 1.1** compares the properties of the most commonly used solvents in various chemical processes. As can be seen, CO_2 has the highest density at critical conditions. **Table 1.2** [93] shows density, diffusivity and viscosity for typical liquids, gases and SCF. In addition to the enhancement of physical properties of SCF at supercritical conditions, thermal properties are also enhanced [93].   Experimental methods for calculating density of SCF are tedious and difficult to carry out [105]. **Equation 1.7** [105] may be used for estimating the density.

$$ln\rho = -27.091 + 0.609\sqrt{T} + \frac{39.66170}{T} - \frac{3.445P}{T} + 0.401\sqrt{P} \tag{1.7}$$

In Equation 8, ρ is the density of the SCF at a temperature T and pressure P, respectively.

Table 1.2: Critical properties of various solvents [93]

Substance	Density (kg/m^3)	Viscosity (µPa.s)	Diffusivity (mm^2/s)
Gases	1	10	1-10
SCF	100 – 1000	50 – 100	0.01 – 0.1
Liquids	1000	500 – 1000	0.001

1.4.1 Phase behavior of Carbon dioxide

Carbon dioxide is the most commonly used supercritical fluid because of its relatively low critical temperature and pressure of 31.1 °C and 73.8 bar, respectively [105]. The desirable properties of CO_2 include non-toxic, non-explosive behavior; completely recyclable; inexpensive; and readily available [96,118,119]. With increasing pressure and temperature towards critical the point, the gaseous and liquid phases become increasingly indistinct (become supercritical phase) as shown in **Figure 1.2.** In the SCF region, the fluid has liquid-like density; gas-like viscosity; very low surface tension; also possessing and very high diffusion coefficients [9,93,110,120]. Optimized applications of substances involving SCF depend on a thorough understanding of their phase equilibrium [121,122].
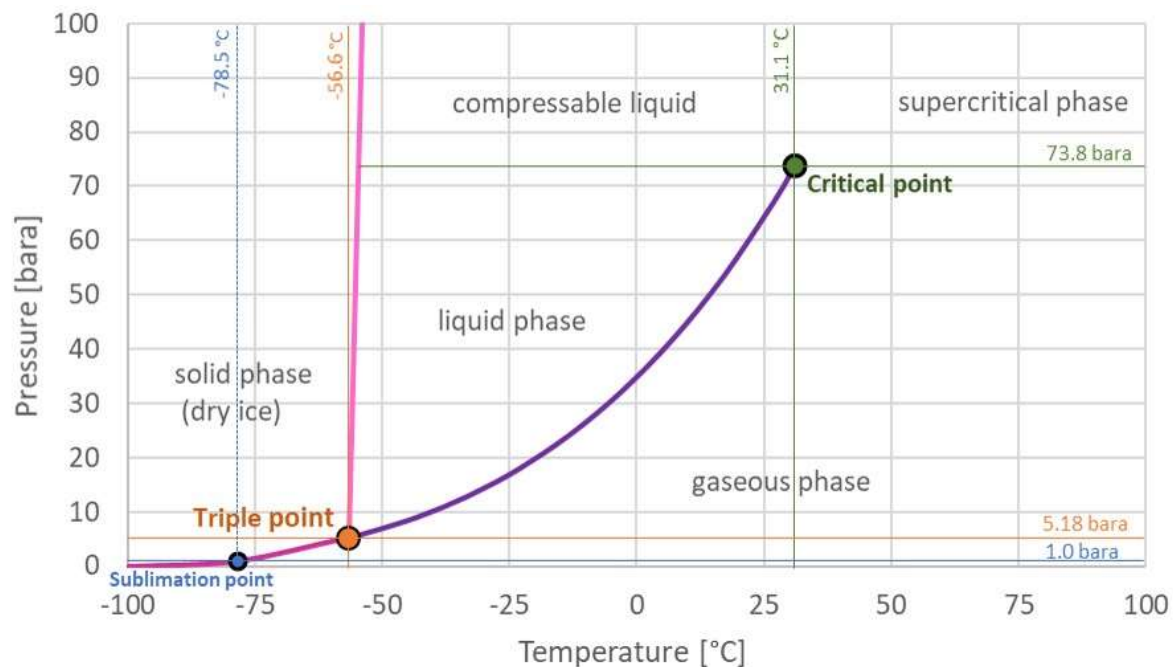
Figure 1.2: Phase diagram of carbon dioxide. Source: The Engineering ToolBox

12

The variation of density of CO_2 with pressure at different temperatures is shown in **Figure 1.3**. Near The critical temperature, density significantly increases as pressure increases. Further away from critical temperature (see for example 50°C in Figure 3), the density-pressure curve is almost a straight line. At much higher pressures and temperatures, the fluid behaves like a gas in the supercritical region. At 31.1 °C and above, carbon dioxide cannot be liquefied, no matter how much the pressure is changed. An increase in density (or decrease in molar volume) is the most important property of a SCF. Since density mostly increases with pressure at constant temperature, solubility generally increases with pressure, especially in the SCF region [93,123–125].
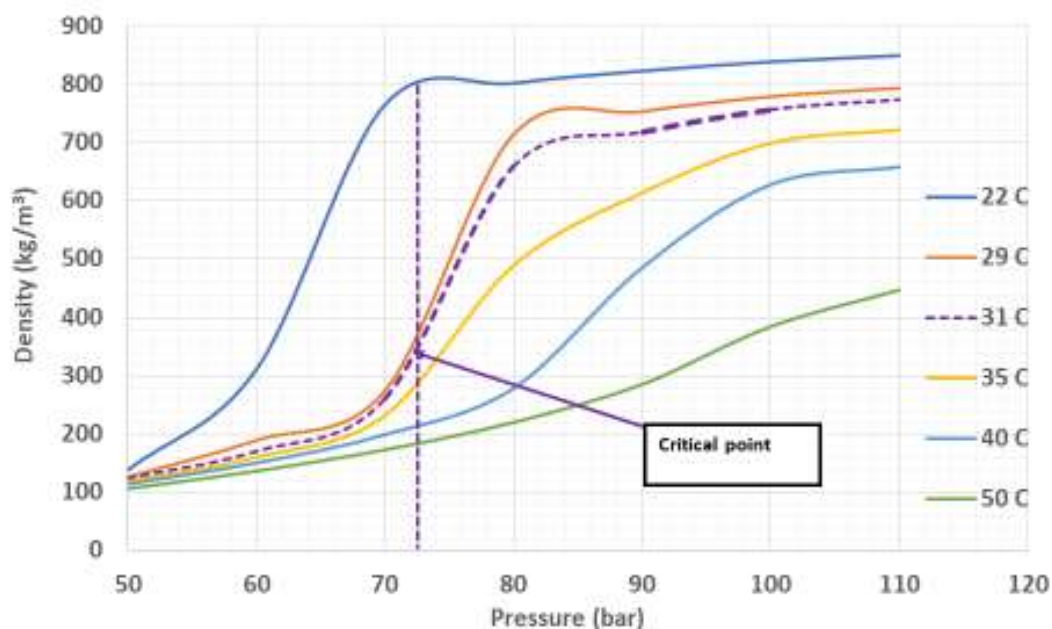
Figure 1.3: Density-pressure phase diagram of Carbon dioxide.

1.4.2 The roles of cosolvents in supercritical fluid applications

Carbon dioxide is not a very good solvent for high molecular weight compounds such as AKD [93,126–128]. Solubility of these high molecular weight waxes are enhanced by addition of

cosolvents, also known as modifiers or entrainers [9,93,110,129–133]. The presence of cosolvents may significantly increase the chemical interactions with the polymeric substances and high pressure fluid systems [93,110,134]. Though CO_2 has a number of desirable properties, its polar index is less than most of the waxes used as sizing chemicals [135]. For example, CO_2 has a solubility parameter of 6.5 $(cal/cm^3)^{1/3}$ at a very high pressure of 200 bar and 35 $^{\circ}$C which is still less than the solubilities of some liquids [135]. Cosolvents increase the solvating power of supercritical fluids either by increasing the polarity of CO_2 or reducing the effective polarity of hydrated polymeric compounds [93,110]. According to Dobbs, Wong and Johnston [135], addition of a cosolvent should not only enhance the solvating strength of the supercritical fluid but also preserve the sensitivity of the solute with respect to temperature and pressure.

1.5 Fabrication of Hydrophobic/superhydrophobic cellulose-based materials

A number of methods for fabricating hydrophobic and/or superhydrophobic surfaces have been reported [2,3]. Due to their chemical nature, not all of the methods are applicable to cellulose papers [1,2]. Typically, any method to fabricate water repellency on surfaces aims at altering the surface energy and surface roughness [2,3,10,22,43]. Darband, Aliofkhazraei, Khorsand and Soskhanhar [3], in their review article on science and engineering of superhydrophobic coatings and surfaces, schematically demonstrated some of the methods for fabricating superhydrophobic surfaces, as shown in **Figure 1.4**. These methods are desribed briefly below:
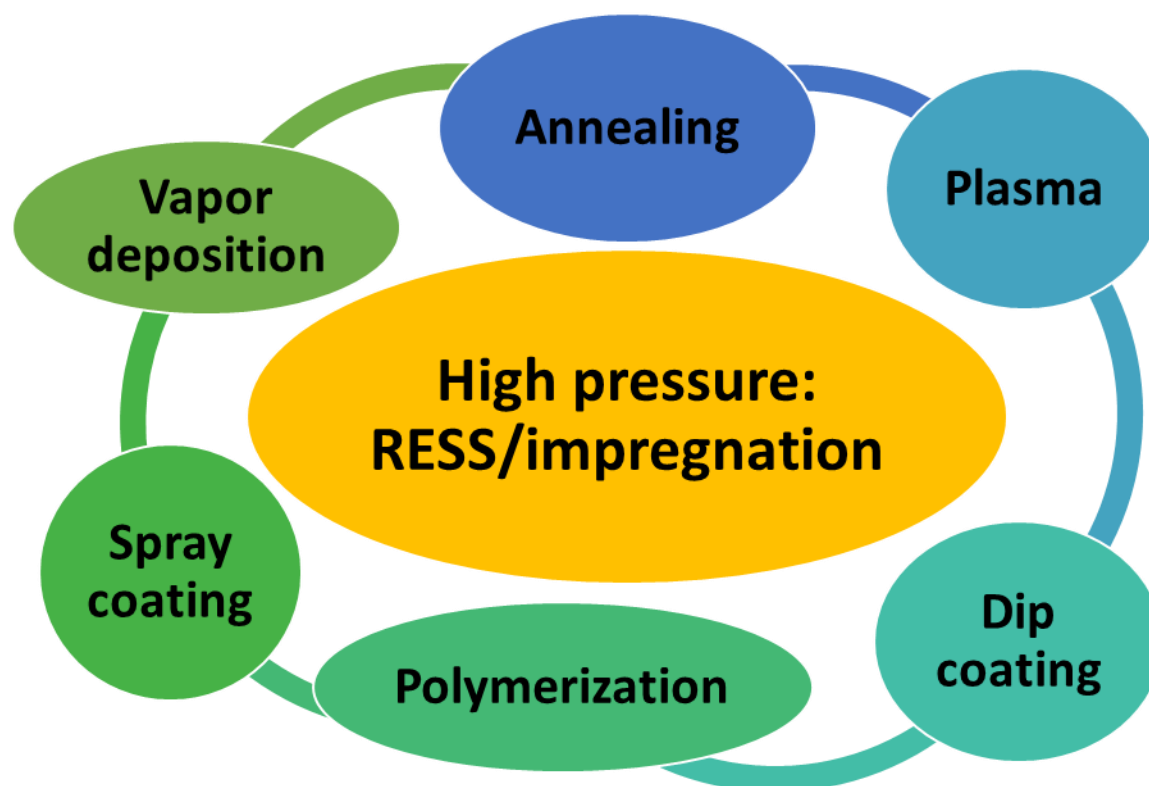
Figure 1.4: Some commonly used hydrophobization techniques for cellulose substrates.

Plasma treatment involves two main steps, namely; etching of the surface and roughening of the etched surface [2,3]. Jiang, Tang, Clinton, Breedveld and Hess [25] carried out a two-step process to create superamphiphobic paper by plasma etching. In this study, oxygen plasma etching was used to produce multiscale roughness on the fibers by thinning the fibers. These surfaces showed strong repellency characteristics for low surface-tension liquids such as Hexane (23.8 mN.m^{-1}) and n-heptane (20.1 mN.m^{-1}).

Dip-coating treatments for making superhydrophobic surfaces on cellulose fibers have recently attracted some attention due to their ease of application [2], and are also referred to as *solution-immersion methods* [136]. The method is a relatively simple, and a very effective technique for

applying superhydrophobic coatings to diverse substrates [136]. Shenghai Zhang and Wang [136] carried out a solution-immersion process to fabricate superhydrophobic coatings on cellulose-based materials. The process involved four simple steps, namely; preparation of the solution-coating, dipping of the cellulose fibers in the solution, washing the coated fibers after being removed from the solution, and vacuum-drying. One main advantage of the solution-coatings is that they can be done by various application methods such as dipping, spin-coating or spraying [2]. Dip-coating treatments may impact the strength of hydrophobized surfaces negatively, and therefore it would be helpful to perform some mechanical analyses alongside with the dip-treatment.

Polymerization is another area that has been extensively studied in recent years to promote superhydrophobicity of surfaces [2,8]. The methods range from simple to sophisticated multi-step procedures. Different polymerization routes such as atom transfer radical polymerization and radiation-induced graft polymerization have been successfully used for CBM and having with contact angles of 140° and above [2].

Spray-coating is by far the most common method of making superhydrophobic paper [1–3]. It can either be a dry method (RESS) [13] or a wet method [1]. Ogihara [1] demonstrated a simple wet-method for making superhydrophobic paper by spraying of alcohol suspension containing transparent SiO_2 nanoparticles. The aggregation state of the SiO_2 nanoparticles and SiO_2 particle size were the two main factors that determined the hydrophobic properties. The process is simple and does not require any sophisticated equipment. Another simple spray method is the dissolution of AKD granules in acetone, and then spraying or pouring the solution onto the substrate before

letting the acetone evaporate [13]. The main disadvantages of the latter method are sparse agglomeration of particles and uneven distribution of AKD on the substrate which affect hydrophobic properties adversely.

Chemical vapor deposition (CVD) involves vaporization and re-deposition of the desired sizing chemical onto the substrate [137]. The key application of this technique rests on the possibility of the vapors being able to condense into small pores on the substrate surface [138].

Annealing can be used to alter the morphology of a surface which could promote dual-scale structure [10]. The presence of hierarchical micro-/nano-structure has been linked to the development of superhydrophobicity on most substrates [2,10,22,41,54,139]. As a rule of thumb, lowering the surface energy of a rough surface or roughening a low-energy surface will improve the hydrophobic properties of the surface [3,139]. The surface roughness produced after hydrophobization may not sufficient to meet the requirement for super resistance to water penetration; and additional treatments may be necessary. According Zhang, Lu, Qian and Xiao [10], annealing of waxes at neat the melting temperatures could drastically change the surface morphology so as to increase the surface roughness. Zhang et al. [10] found out that emulsified beeswax and carnauba wax mixtures could separate from the wax mixture upon heating; micron and submicron particles were produced as a result. In a study by Yokoyama and Sugiyama [41], annealing was found to accelerate the ordering of block copolymers which enhanced the hydrophobicity of the surfaces by thickening the surface of fluorinated domains.

In *Rapid expansion of supercritical solutions technique* (RESS), a coating mixture prepared at high-pressure is sprayed onto the substrates at atmospheric conditions [13,112,140]. The application of RESS is predicated on the high solvating power of $scCO_2$ to create fine particulate matter of the sizing solution of choice [2,13,141,142]. Due to the fast transfer of phases from a very high pressure to atmospheric pressure, extremely small particles can be formed on the substrates [143]. According to Quan, Werner, Wagberg and Turner [13], three main factors influence RESS which are spraying distance, pre-expansion temperature and pre-expansion pressure.

The term *impregnation* refers to delivery of the desired chemical (sizing agent) directly into the entire thickness of the substrates rather than the surface, and in this case, directly to the fibers of the paper substrates [9]. Two main mechanisms used to describe impregnation are: deposition and molecular dispersion [110]. In deposition, CO_2-solute mixture fills the pores of the solid polymetric matrix. During depressurization, CO_2 diffuses out of the pores, leaving behind the solute in the matrix. For molecular dispersion, the CO_2-solute mixture is dissolved in the solid-polymeric matrix. During depressurization, as CO_2 leaves, the solute is precipitated within the pores which may lead to swelling and/or plasticization [110]. One of the main advantages of supercritical impregnation is the ease of entirely removing the SCF after the process is complete.

1.6 Solubility studies

Accurate solubility data are integral for the development of most hydrophobization techniques involving supercritical fluids such as RESS, supercritical fluid extraction (SFE), particles from gas

saturated solutions (PGSS) and supercritical impregnation. According to Tang, Jin, Zhang and Liu [109], the reliability analysis of the experimental solubility set-up can be carried out by: (1) taking the measurements three times within $\pm 5\%$ deviation and (2) verifying selected literature data. Another class of solutes used in supercritical fluids is heavy hydrocarbons. Poor solubility of heavy hydrocarbons in supercritical fluids has been reported [144,145]. However, Shi, Jing and Qiao [144] studied the solubility of heavy hydrocarbons with different chain lengths in supercritical carbon dioxide to determine regions of optimum operating conditions.

According to Agustin, Lin, Kurniawan, Ju, Soetardo and Ismadji [118], availability of these solubility data at a wide range of pressures and temperatures is important for designing, optimizing and implementing supercritical processes. Semi-empirical models have also been used to evaluate the solubility of solutes in supercritical carbon dioxide [98,109,130]. In these methods, some physical properties of the solutes are needed, such as enthalpy, fusion temperature and activity coefficients. Because approximations are involved, care must be taken before the data are used and implemented. The degree of deviation of calculated data from experimental data can be evaluated by average absolute relative deviation (AARD) [146].

Solubility also plays a vital role in high-pressure processes such as impregnation techniques – it promotes a faster and a more homogenous impregnation [110]. An increase in solubility at SCF conditions leads to enhanced mass transfer rates between a solute (sizing chemical) and a SCF (CO_2). Therefore, increased solubility will lead to an increase in the amount of the solute impregnated (mass of solute intercalated within the pores of the substrate per unit area) on the substrate. In **section 1.2,** it was pointed out that low surface-energy and/or high surface roughness

favor the development of hydrophobicity. As the amount of the low-energy chemical on the substrate increases due to increased solubility in the SCF, there will be a corresponding increase in the hydrophobic properties of the surface – caused by a reduction in the surface energy and/or an increase in the surface roughness. An increase in solubility will produce an increase in the degree of hydrophobicity [11]. Therefore, a direct relationship can now be made between impregnation (mass/area) and hydrophobicity. CA is a function of the amount of solute impregnated onto the paper (I), which is indirectly a function of the solute's solubility in CO_2 (S). Mathematically, the relationships can be represented as follow in **Equations 1.8 and 1.9**:

$$CA = f(I) \tag{1.8}$$

$$I = f(S) \tag{1.9}$$

Where f is a function.

1.7 Thermodynamic modeling

Information on experimental determination of solubility of AKD in $scCO_2$ appears to be scarce in the literature [11]. Experimental determination of the solubilities of solids in (SCFs) at wide range of temperatures and pressures could be very expensive and time-consuming [11,12,102,113,114,119,147–149]. Although there a number of methods to experimentally determine the solubility, thermodynamic models may sometimes be needed to correlate the experimental data [107]. Therefore, it is important to use the powerful predictive capabilities of thermodynamic models to determine solubilities of various solutes from diverse applications in

supercritical fluids [150]. Thermodynamic models in the form of activity coefficients offer a number of different approaches for evaluating activity of the liquid phases [114,151]. A detailed description of the following activity coefficient models was given by Prausnitz, Lichtenthaler and Azevedo [151]: Redlich-Kister, Barker, Wohl, van Laar, non-random two liquid (NRTL), universal quasi-chemical theory (UNIQUAC) and Wilson's models. These models require some constants that are usually regressed from experimental data. Group contribution methods are alternative models for calculating activity coefficients in the absence of experimental data or physical constants [152–154]. They can be used for calculating activity of AKD in the liquid phase as its physical property constants such as critical pressure and temperature are not known. Another class of models is the equations of state (EOS) – applicable over a wide range of pressures and temperatures but may only be used for inorganic gases and hydrocarbons [155]. EOS are generally preferred to the above activity coefficient models because they incorporate sophisticated calculations that enhance their predictive capabilities [155]. EOS models also have a smooth phase transition and do not require the need to choose an arbitrary reference state which could interfere with their accuracy, but they are not good near critical conditions [113,150,155]. EOS models do require some physical constants in their calculations, however. Therefore, they cannot be used for modeling substances whose physical property constants are not known. EOS coupled with other models such as conductor-like screening model – realistic solvation (COSMO-RS) will improve the prediction capacity accuracy [156]. In the absence of critical constants for organic solutes, EOS models may still be used to determine solubility by using "group-contribution based estimation of pure component properties" [157,158]. The critical constants can be determined by the group contribution method developed by Klincewicz and Reid [159] (originally developed by Lydersen (1955).

1.7.1 Fundamental Thermodynamics of Phase Equilibrium

The starting point for phase equilibrium calculations is fugacity [120,155,160,161]. At equilibrium, the fugacity of a substance must be the same in all the phases. **Equations 1.10 to 1.13** give the fugacity relations of the phases. The solute is denoted by 1.

$$f_1^S = f_1^L = f_1^V \tag{1.10}$$

$$f_1^L = x_1 \gamma_1 f_{1,pure}^L \tag{1.11}$$

$$f_1^V = y_1 \phi_1^V P \tag{1.12}$$

$$f_1^S = P_1^{sub} \phi_1^S \exp\left[\frac{1(P-P_1^{sub})}{RT}\right] \tag{1.13}$$

f_1^L is the fugacity of component 1 in the liquid phase; f_1^S is the fugacity of component 1 in the solid phase; f_1^V is the fugacity of component 1 in the vapor phase; γ_1 is the activity coefficient of component 1; $f_{1,pure}^L$ is the fugacity of pure (subcooled) liquid solute (often taken as the saturated vapor pressure, and is f_1^V is the fugacity of component 1 in the vapor phase; [120]; ϕ_1^V is the fugacity of species 1 in the vapor phase; y_1 is the mole fraction of component 1 in the vapor phase; ϕ_1^S is the fugacity of solid which is usually close to unity due very low sublimation of high molecular weight compounds [108,124,153,162]; P_1^{sub} is the sublimation pressure; v_2^S is the molar volume of pure solute; T and P are temperature and pressure, respectively. The expression, $\left[\frac{v_1^S(P-P_1^{sub})}{RT}\right]$, is called Poynting factor – which is calculated from experimental values.

1.7.2 The phi-phi $(\phi - \phi)$ and phi-gamma $(\phi - \gamma)$ models

An EOS is mostly used to obtain the fugacity of the vapor phase as functions of temperature, pressure and composition. For the liquid phase, there are two ways of computing the fugacity. One is using the same EOS used for the vapor phase to compute the fugacity of the liquid phase, and the other is using an activity coefficient model to compute the liquid phase [155]. When EOS is used to compute both the vapor and liquid phase, it is often referred to as $\phi - \phi$ model. In $\phi - \phi$ model, the highest molar volume should be taken as the vapor volume while the smallest volume as the liquid molar volume. When EOS is used to compute the vapor and activity coefficient for the liquid phase, it is referred to as $\phi - \gamma$ model.

1.7.3 Mixing rules

To use cubic EOS models for predictions and correlations of phase equilibrium mixtures, composition-dependent parameters a and b that account for non-ideal interactions of the species are needed. The relations for the interaction parameters a and b are given in **Equations 1.14 and 1.15**. Mixing rules are used to describe the hypothetical behavior of these interaction parameters in mixtures.

$$a = \sum_i \sum_j x_i x_j a_{ij} \tag{1.14}$$

$$b = \sum_i x_i b_i \tag{1.15}$$

where x is the molar fraction; i and j are the components in the solution

Equations 1.16 to 22 give some of the more common mixing rules:

van der Waals mixing rules (VDWMR) [151,155]

$$a_{ij} = (1 - k_{ij})(a_i a_j)^{1/2} \tag{1.16}$$

Lorentz-Berthelot mixing rules (LBMR) [91]:

$$a_{ij} = 0.45724 R^2 T_{cij}^2 \left(\frac{a_{ij}}{P_{cij}} \right) \tag{1.17}$$

$$T_{cij} = (1 - k_{ij})(T_{ci} T_{cj})^{\frac{1}{2}} \tag{1.18}$$

$$V_{cij} = \left(\frac{V_{ci}^{\frac{1}{3}} + V_{cj}^{\frac{1}{3}}}{2} \right)^3 \tag{1.19}$$

$$P_{cij} = \frac{Z_{cij} R T_{cij}}{V_{cij}} \tag{1.20}$$

$$Z_{cij} = \frac{Z_{ci} + Z_{cj}}{2} \tag{1.21}$$

$$a_{ij} = (a_i a_j)^{\frac{1}{2}} \tag{1.22}$$

24

where k_{ij} is the fitting parameter, also known as the coupling parameter [163]; T is temperature; R is gas constant; T_c is the critical temperature; P_c is the critical pressure; V_c is critical molar volume; Z_c is critical compressibility factor; a and b are interaction parameters; i and j are the components in the solution.

1.8 The research motivation and goals

1.8.1   Motivation for the study

Superhydrophobic coating formulations are used to impart water repellency on various substrates. Unfortunately, several of the coating formulations (and common methods of application) cannot be used on CBM due to the ease of being damaged by the treatment(s) applied.   Also, the coating methods may be too complicated and often involve multi-step processes. Low surface energy organic compounds such as fluoropolymers are sometimes added to augment or tune hydrophobic surfaces made from many traditional methods [2]. Additional functionalities could be added alongside water repellency which necessitate the coating to be thin and light. Impregnation is an alternative technique to from typical coating methods (which coat only the substrate surface) which coats the surface of every fiber making up the substrate. Impregnation methods produce coatings that are very thin, well distributed over the fibers, and evenly sized through the entire thickness of the substrate, with less than 1 g of the sizing chemicals – much lower than that used in surface sizing methods [9]. Also, the weight of the coating is much lower when compared with other coating methods (average coating thickness of most methods is usually greater than 50 μm) [1,6,10,13,142]. Impregnation techniques are capable of rendering the CBM sufficiently water-repellent with a single hydrophobization step and also encourage the inclusion of additional

functionalities to the surface due to its low coating weight. Since it coats the entire thickness of the substrate, impregnation can be used for non-planar surfaces [164]. Impregnation techniques have a potential to improve the mechanical robustness of the CBM [5]. The U.S. Food and Drug Administration (FDA) recommends the use of edible waxes for food-based applications because of possible leaching or diffusion of the coating material into the packaged item [44].

In this study, the viability of food-grade waxes as alternative sizing chemicals is also explored along with AKD wax which is routinely used in papermaking. Where the surface energy of the waxes is not significantly low to achieve the desired hydrophobicity, instead of using of fluoropolymers, annealing treatment is used to enhance the water repellency. Finally, in addition to the experimental investigation, the robustness and predictive accuracy of thermodynamic modeling is investigated to optimize the performance of the waxes in supercritical medium.

1.8.2 Proposed study

The **research goal** is to develop highly water-repellent surfaces on cellulose substrates using supercritical impregnation methods, for food packaging applications. With this in mind, the three key objectives to be pursued are:

(a) Thermodynamically model the solubility of AKD solute in scCO$_2$ to help identify optimal conditions for impregnation. The model can be used to predict unavailable experimental data at of AKD over a wide range of pressures and temperatures.

(b) Assess the hydrophobic performance of these solutes (AKD and food-grade waxes) when impregnated into cellulose substrates. This study will determine the most appropriate solutes for creating highly water-repellent surfaces, and the conditions under which these are obtained (includes supercritical conditions as well as annealing in some cases).

(c) Examine the surface and interfacial energies of various impregnated solutes (AKD, carnauba wax, natural vegetable wax, paraffin wax, beeswax, bees-milk) into cellulose substrates, and their resulting behavior / interactions with water droplets applied to the surface. The examination will reveal the mechanic pathways of the sizing and surface morphology together with the uniform distribution of the sizing chemicals over the fibers, mechanical durability, surface and interfacial energies.

CHAPTER II

THERMODYNAMIC MODELS OF ALKYL KETENE DIMER DISSOLVED IN
SUPERCRITICAL CARBON DIOXIDE

The chapter was submitted for publication to the Journal of Chemical & Engineering Data.

2.1 Abstract

This study investigated solubility modeling of alkyl ketene dimer (AKD) in supercritical carbon

dioxide ($scCO_2$). Group contribution estimation methods were used to determine the critical

properties of AKD, followed by modeling with Peng-Robinson equation of state using van der

Waals mixing rules. The calculated solubilities were less accurate near the critical point, however

showed very good agreement with the experimental data at higher pressures over a wide range of

temperatures. Binary interaction parameters recovered from equilibrium and extraction solubility

measurement methods at the same conditions were different. As a result, data interpretation and

experimental set up should be considered before these results are implemented. These findings

will assist in designing high pressure processes such as rapid expansion of $scCO_2$ solution (RESS)

and $scCO_2$ impregnation of solutes into substrates.

2.2 Introduction

It is both fascinating and expedient for researchers and experts to seek and develop alternative technological processes that are more efficient and environmentally friendly. New process pathways that produce better yields, less toxins, lower energy consumption, and more sustainable economic viability, are considered to be alternative technological methods [95]. The advent of supercritical fluids (SCF) as alternative solvents for various chemical and industrial processes has replaced many organic solvents and increased efficiency [92]. Though they have been a subject of research since the 1800s, they have only seen increased attention in the last few decades [126]. SCF have many applications in pharmaceutics, material and polymer industries, biotechnology, biomedical industry, separation processes, purification treatments, and surface modifications, amongst others [9,91,108,126,165].

Density of SCF is very sensitive to imperceptible changes in temperature and pressure, especially near the critical point. As a result, the solubility of a solute in a SCF can increase by several orders of magnitude by manipulating temperature and pressure, since solubility is directly proportional to density. SCF can diffuse much faster through solids than most liquids, and still possess significantly high solvation strength to solubilize the solute – owing to their gas-approaching viscosity, high diffusivity and liquid-like density [9]. Carbon dioxide is the most commonly used supercritical fluid due to its relatively low toxicity, a critical temperature of $31.1^{\circ}C$, and a pressure of 73.8 bar [105,165]. In addition, it is non-flammable, non-toxic, readily miscible with a number of solvents, and possesses an ease of recovery after processing. Being a small and linear molecule, it has a high diffusion coefficient. CO_2 is not good at solubilizing solutes with high molecular

weights or medium / high polarity [129] – and its own very low polarity reduces solvating strength [133]. Cosolvents, modifiers or entrainers [93] can be added to the SCF to significantly alter its solvating properties and enhance its selectiveness [93,110]. Cosolvents enable more chemical interactions between the solute and SCF which in turn leads to significant enhancement in solubility [110,129–132]. The cosolvent can be a SCF, gas or liquid, polar or non-polar [133].

Solubility data are integral both for the development and optimization of processes involving SCF applications [11,89,160]. The solvating power of SCF can be tuned by adjusting the operating parameters – temperature, pressure and mole fractions [113]. Design and implementation of high-pressure processes requires solubility data [113,165], but unfortunately, this data is not always available or is too expensive to experimentally determine for the solute of interest [113]. Therefore, thermodynamic models are used to evaluate the solubility, and the reliability of the process depends on how well the models can accurately predict unavailable experimental data [11,113].

A variety of models have been proposed for calculating the solubility of solutes in SCF [105,146,151,161,165,166]. Two-parameter cubic EOS models are the most commonly used due their better computational efficiencies and accuracies in modeling both liquid and vapor phases at high pressures, compared with others [167]. The EOS models often involve sophisticated computational calculations and procedures [150], and physical property constants such as critical pressure and temperature, sublimation pressure, acentric factor, and molar volumes of the compounds being modeled [105,165]. It is difficult to know all these physical property constants for a single compound, and these may be estimated using correlations and group contribution estimation methods (GCEM) [91,105,165,168–170]. The estimated values of these physical

constants can significantly affect the accuracy of the solubility predictions [105]. The main source of errors in using EOS models comes from the numerical values of physical property constants [105,171]. For example, a wrong estimate of sublimation pressure could produce an average error up to 35% [105].

EOS models are not good for estimating operating conditions near the critical values due to the large variation in the density of SCF in this region [172]. Accuracy of the EOS models can be increased by using more sophisticated mixing rules that account for various nonideal intermolecular interactions and renormalization group methods as well as scaling of nonanalytic equations of state [167,173,174]. EOS models require mixing parameters that are usually fitted to experimental data. The parameters are a_m (van de Waals energy or attractive parameters) and b_m (covolume parameters) [104,162].

Regardless of the adopted thermodynamic model, the overall objectives of the modeling are: predictive accuracy; improved computational speed; thermodynamic consistency; and wide-range predictive capability [150]. Finally, the actual application should be factored in before a specific thermodynamic model is chosen. However, thermodynamic models that use some experimentally determined data (no matter how few) are generally more accurate.

Alkyl ketene dimers (AKD), one of the most commonly used sizing agents [44,175], was the solute considered in this study, along with supercritical carbon dioxide (scCO$_2$) as the solvent. There are no solubility models developed specifically for AKD in scCO$_2$ to the best of the authors'

31

knowledge – only a few groups who have obtained experimental data [11,12]. AKD is not a pure compound, and consequently its critical conditions are not known because it decomposes before it reaches critical state [13]. A number of GCEM correlations have been proposed for estimating the critical properties, acentric factor and vapor pressure of compounds [159,169,176,177], and were used to predict these properties for AKD. The solubility of AKD in $scCO_2$ can, therefore, be modelled with a cubic EOS after these physical properties have been determined.

AKD solubility in $scCO_2$ was calculated using Peng Robinson equation of state (PREOS) model with van der Waal mixing rules. The typical structure of the AKD considered has C14 and C16 alkyl chain lengths as shown in **Figure 2.1**. Thermodynamic models were compared with experimental data obtained from the pioneering work of Rodriguez-Meiozoso, Werner, Knez and Turner [11], who studied phase behavior of AKD in $scCO_2$ and solubility determination using different measurement methods. It appears there has not been newer work in the literature on AKD solubility in $scCO_2$ since their study. Mathcad was used for thermodynamic computations and
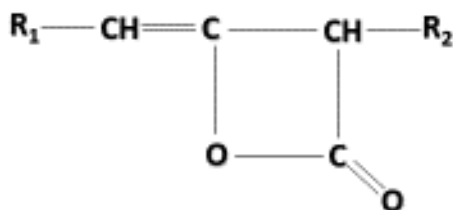
Figure 2.1: Molecular structure of AKD. Note that R1 and R2 are typically in the range of C14 – C16.

calculations of the solute solubilities in $scCO_2$. Mathcad was chosen due to its simplicity, powerful computational robustness and speed. In addition, it allowed solubility modeling to become a routine exercise that can be easily carried out and readily performed without the use of complicated programing packages.

2.1 Model framework

2.1.1. Fugacity of the solid-supercritical fluid phase equilibria

The steps required to calculate the solubility are shown in **Figure 2.2**, and represent the various calculations performed to compute the solubility of AKD in $scCO_2$ at various temperatures and pressures. For the purposes of thermodynamic model development, only a binary mixture was considered where $scCO_2$ and AKD were identified as components 1 and 2 respectively. From the chemical potential standpoint, at equilibrium, the fugacity of the solid and supercritical phases are equal at the same temperature and pressure [91]. Fugacity coefficient of some solids are very close to unity due to very low sublimation of high molecular weight compounds [108,124,153,162]. After simplifying the fugacity equation, the model equation for determining the solubility of AKD in $scCO_2$ is given by **Equation 2.1**.

$$y_2 = \frac{P_2^{vap}}{P\phi_2^{sup}} \exp\left[\frac{v_2^S(P - P_2^{vap})}{RT}\right] \qquad (2.1)$$

where y_2 is the solubility of AKD in CO_2; P_2^{vap} is the vapor pressure of AKD; v_2^S is the molar volume of pure solute; ϕ_2^{sup} is the fugacity of the solute in the supercritical phase; T and P are temperature and pressure, respectively; and R is the universal gas constant. The expression, $\left[\frac{v_2^S(P - P_2^{vap})}{RT}\right]$, is called the Poynting factor.
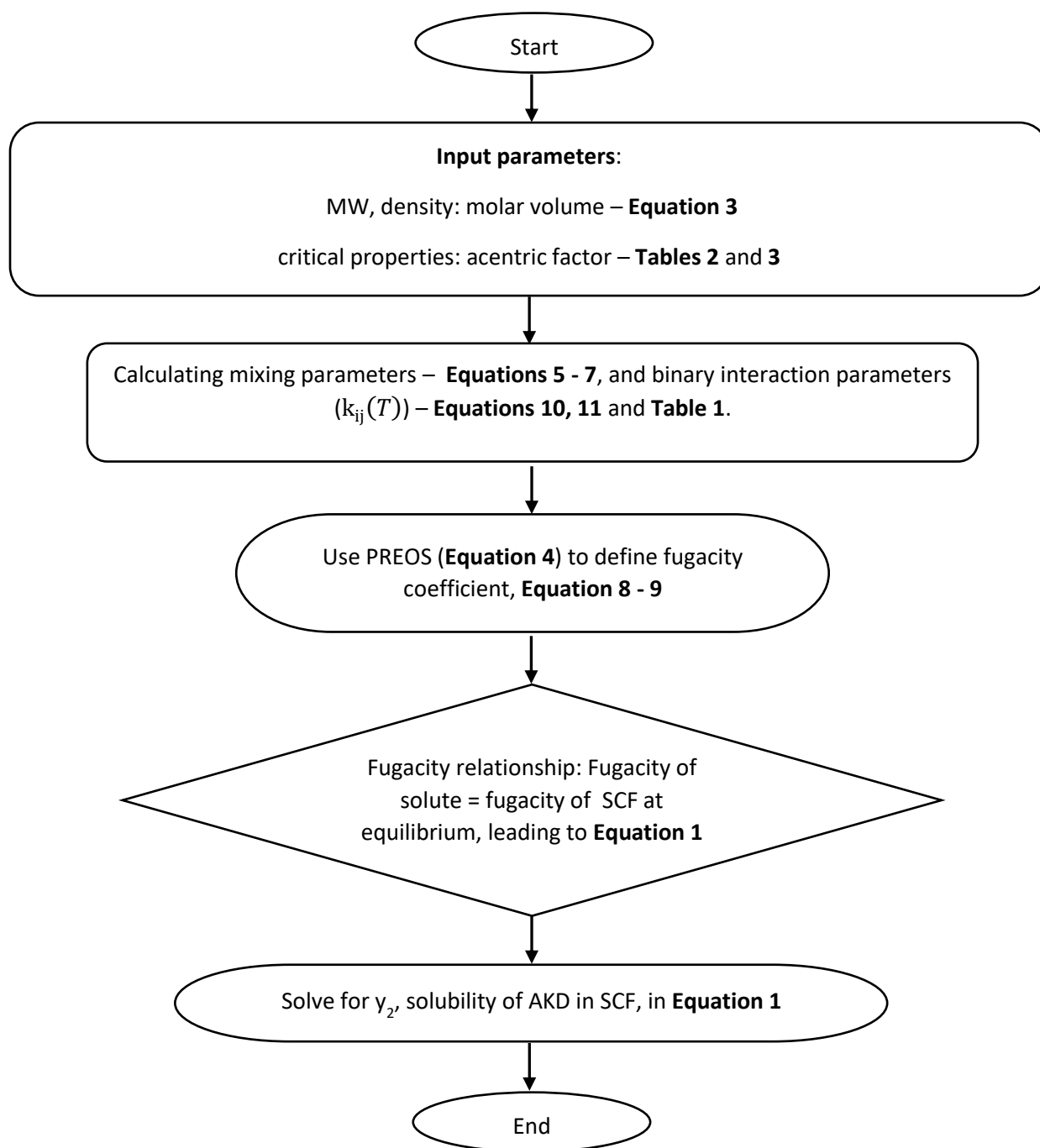
Figure 2.2: Model algorithm.

The vapor pressure of AKD was estimated using the functional group parameters given by Tu [178]. **Equation 2.2** was the result when the vapor pressure for GCEM was simplified for AKD with 14 and 16 alkyl groups.

$$P_2^{vap}(T) = 1.980 \exp\left[8.575 - \frac{95.597}{T} - 3.744\,ln(T) - 0.583T\right] \quad (2.2)$$

where T is temperature in K divided by 100K.

The density of AKD wax (Aquapel^{TM} 364K sizing agent) supplied by Solenis was estimated by a simple laboratory procedure. AKD pellets were melted in an oven and then poured into a petri dish of known dimensions. The liquid was allowed to solidify at room temperature, after which the net mass was obtained. Density of bulk AKD was calculated by dividing the net mass of solidified AKD by the volume of the petri dish. This density value is an estimate 'in the absence of other information', and the average value of three repeat measurements was 768 kg/m$^{3.}$ The molar volume of AKD was then calculated by **Equation 2.3**.

$$v_2^s = \frac{MW}{\rho_{AKD}} \quad\quad (2.3)$$

where ρ_{AKD} is bulk density of AKD and MW is the molecular weight of the solute.

2.1.3 Peng-Robinson Equation of State (PREOS) and mixing rules

The Peng-Robinson equation of state used for the modeling of the SCF is given in **Equation 2.4**, while the mixing rules are shown in **Equation 2.5.** Binary interaction parameters are given in **Equations 2.6** and **2.7.** The fugacity coefficient is given in **Equations 2.8** and 2.**9**.

$$P = \frac{RT}{v - b_m} - \frac{a_m(T)}{v(v + b_m) + b_m(v - b_m)} \qquad (2.4)$$

$$a_m = \sum_i^n \sum_j^n y_i y_j a_{ij} \ , \ \ b_m = \sum_i^n x_i b_i \qquad (2.5)$$

$$a_{ij} = \sqrt{(a_i a_j)}(1 - k_{ij}) \ , \ \ a_i = \frac{0.457235 \alpha_i R^2 T_{ci}^2}{P_{ci}} \ , \ \ b_i = \frac{0.077796 RT_{ci}}{P_{ci}} \qquad (2.6)$$

$$\alpha_i = [1 + (0.37464 + 0.54226 \omega_i - 0.26992 \omega_i^2)(1 - \sqrt{T_{ri}}]^2 \qquad (2.7)$$

$$\phi_2^{sup} = \exp\left[\frac{b_2}{b}(Z - 1) - ln(Z - B) - \frac{A}{2\sqrt{2}B}\left[\left[\frac{2[(1 - y_2).a_{12} + y_2.a_2]}{a_m} - \frac{b_2}{b_m}\right] ln\left[\frac{v + (1 + \sqrt{2}).b_m}{v + (1 + \sqrt{2}).b_m}\right]\right]\right] \qquad (2.8)$$

$$A = \frac{a_m P}{(RT)^2} \ , \ B = \frac{b_m P}{RT} \qquad (2.9)$$

where v is the molar volume of the SCF: Z is the compressibility factor; ω is the acentric factor; and P_c, T_c and T_r are critical pressure, critical temperature and reduced temperature, respectively.

2.1.4 Binary interaction parameters

The binary interaction parameters $k_{ij}(T)$ are determined by minimizing the objective function (**Equation 2.10**) in terms of calculated and experimental solubilities which are then used to fit a_{12}

in **Equation 2.11** to the experimental data. Binary interaction parameters regressed from experimental data of AKD/scCO$_2$ from cloud-point and extraction methods for various temperatures are given in **Table 2.1**.

$$\Sigma_{i=0}^{n}\left[y_{exp} - y_{cal}\right]^2 = 0 \qquad (2.10)$$

$$a_{1,2} = a_1 a_2(1 - k_{1,2}) \qquad (2.11)$$

where y_{exp} is the experimental solubility and y_{cal} is the calculated solubility from Equation 1. Note that y_2 in Equation 1 is the same as y_{cal} in Equation 2.10.

Table 2.1: Binary interaction parameters regressed from experimental data of AKD/SC-CO2 of cloud-point and extraction methods.

AKD-CO$_2$ System	Temperature (K)	$k_{i,j}$
Cloud-point method	323.15	-0.05754
Cloud-point method	333.15	-0.10912
Cloud-point method	343.15	-0.14223
Cloud-point method	353.15	-0.17443
Extraction method	313.15	-0.05196
Extraction method	333.15	-0.13817
Extraction method	353.15	-0.24207

2.1.5 Critical properties

The critical properties of CO_2 are given in **Table 2.2**. The results of the different GCEM used to determine the physical properties of AKD are given in **Table 2.3**. In this case, the critical temperature and pressure that have the best correlation of the AKD experimental data are Fedors and Lydersen, respectively. Acentric factor was calculated from the temperature and pressure using Edminster correlation [179]. Variation and over-estimation of critical properties are well known in GCEM [171].

Table 2.2: CO2 critical properties

Functional group	T_c, K	P_c, bar	ω	Ref
CO_2	304.21	73.8	0.225	[180]

Table 2.3: Group contribution estimation of AKD critical properties. Tb is the estimated boiling temperature of AKD. Corrected Tb from Stein and Brown [176] are used from sets 2-5

Sets	T_b (K)	T_c (K)	P_c (bar)	ω	Estimation Methods	References
1	1050	1333.2	21.9	1.12	Joback and Reid	[169]
2	800.2	1024.9	*7.54*	0.33	*Lydersen*	[159]
3	*800.2*	*900.9*	-	*1.91*	*Fedors*	[159]
4	800.2	944.7	9.77	1.332	Ambrose	[159]
5	800.2	1021.9	21.9	1.062	Joback and Reid	[169]

2.2 Results and Discussion

2.2.1 Modeling of cloud-point pressure determination of solubility

The cloud-point solubility measurements were performed within a pressure range of 10-30 MPa, and temperature of 50-80ºC. The experimental solubilities and pressures are plotted in **Figure 2.3** together with calculated solubilities. The prediction of the solubilities is better at higher than lower pressures, as confirmed by the experimental data. As Hezaze et. al. [108] pointed out, EOS models usually produce worse estimations of solubilities at regions near the critical pressure and temperature, but are more accurate further from these conditions. This is often attributed to the transient behavior of SCF density in this region. The calculated data showed several orders of magnitude lower than predicted at this region. However, this transient-behavior effect on the estimated solubilities can be improved if more representative data and more sophisticated EOS are used [153]. RESS [13] and impregnation [14] processes are often performed at higher pressures where the modelled data better matched the experimental data. This study will therefore be integral in designing such processes. **Table 2.4** compares the experimental and calculated data. The data at 323.15 K show good comparisons between experimental and modeling data at all pressures except for 11 MPa. At 333.15 K, good agreement was found at 22 MPa and above, while a similar pattern is observed for the other temperatures in the higher-pressure range as well. The average error between actual and calculated solubilities at the higher pressures (italicized error conditions in Table 4) was 16%, which demonstrates a reasonably good prediction of the model for AKD solubilities overall. The model was clearly able to predict a similar trend for all experimental data at higher densities.

Figure 2.4 shows isotherms of calculated solubilities at various pressures using binary interaction parameters regressed from cloud-point pressure solubility data. The trajectory of the solubility for each isotherm is similar although the solubility decreased with increasing temperature at a given pressure, for most pressures shown. Upper crossover pressures [181] were observed at approximately 24 and 28 MPa, after which solubility began to increase when temperature decreased. Foster et. al. [182] reported that sufficient accurate experimental data around the critical point are needed for isotherms to have a common crossover pressure. For experimental data to be considered 'reliable and consistent', a plot of solubility vs pressure should have a common crossover pressure [182]. However, in this study, a common crossover pressure is not observed because of unavailability of experimental data in the vicinity of the critical point. The temperature range of the modelled isotherms also includes the melting point of AKD (between 313.15 and 333.15 K [13], meaning that the solute was solid for some cases and liquid for others. Common cross-over pressures are additionally not observed in these cases [182]. At 30 MPa, each temperature condition appeared to plateau and converge to a similar solubility.
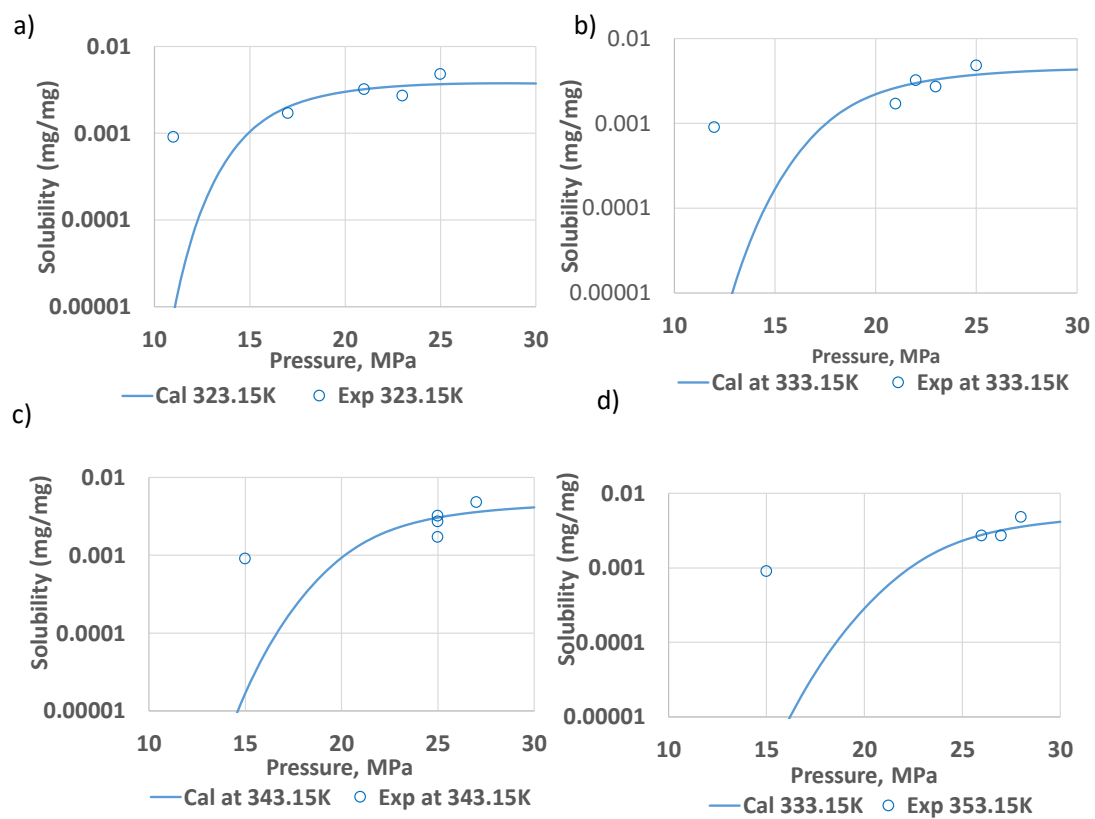
Figure 2.3: Comparison of cloud-point solubility of AKD in scCO₂ [16] with the modeling at a) 323.15K, b) 333.15 K, c) 343.15 K, and d) 353.15 K.

Table 2.4: Comparison of the calculated solubilities with data obtained from cloud-point determination method. All AKD solubility experimental data were taken from Rodríguez-Meizoso et. al. [11]

Pressure (MPa)	Experimental solubility (mg/mg)	Calculated solubility (mg/mg)	Standard deviation (mg/mg)	Relative standard deviation %	Absolute relative error %
T = 323.15K					
11.00	9.00E-04	6.54E-06	6.32E-04	139.38	99.27
17.00	1.70E-03	2.01E-03	2.19E-04	11.82	*18.24*
21.00	3.20E-03	3.22E-03	1.13E-05	0.35	*0.50*
23.00	2.70E-03	3.51E-03	5.73E-04	18.45	*30.00*
25.00	4.80E-03	3.68E-03	7.94E-04	18.73	*23.40*
T = 333.15K					
12	9.00E-04	1.68E-06	6.35E-04	141	99.81
21	1.70E-03	2.63E-03	6.58E-04	30.4	54.76
22	3.20E-03	2.99E-03	1.48E-04	4.77	*6.53*
23	2.70E-03	3.29E-03	4.19E-04	14	*21.93*
25	4.80E-03	3.75E-03	7.46E-04	17.5	*21.98*
T = 343.15K					
15	9.00E-04	1.68E-05	6.25E-04	136.24	98.13
25	1.70E-03	3.04E-03	9.50E-04	40.07	79.06
25	3.20E-03	3.04E-03	1.10E-04	3.53	*4.88*
25	2.70E-03	3.04E-03	2.43E-04	8.47	*12.74*
27	4.80E-03	3.59E-03	8.56E-04	20.41	*25.23*
T = 353.15K					
15	9.00E-04	2.13E-06	6.35E-04	140.48	99.76
26	2.70E-03	2.77E-03	5.23E-05	136.18	*2.74*
27	2.70E-03	3.19E-03	3.47E-04	113.67	*18.19*
28	4.80E-03	3.56E-03	8.79E-04	85.38	*25.90*
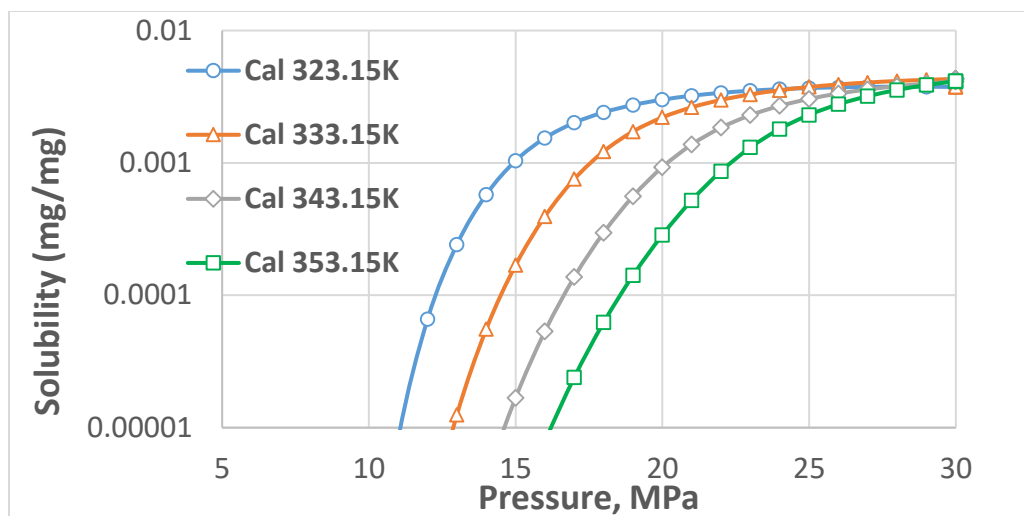
Figure 2.4: Isotherms of calculated AKD solubility in scCO$_2$ with binary parameters regressed from cloud-point pressure solubility data.

2.2.2 Modeling of extraction determination of solubility

The experimental data obtained from extraction methods are the highest of all the solubility measurement methods used – three times as high as those of cloud-point temperature. **Table 2.5** compares calculated and experimental solubility data from the extraction method, and this is also shown in **Figure 2.5**. The calculated solubility shows good agreement with experiment across all temperatures at higher pressures (20 MP and higher). Except for the first data point at 10 MPa, most calculated and experimental solubilities were the same order of magnitude. The overall average error for this data set between experimental and calculated solubilities, and pressures 20 MPa and higher was 21%, as indicated by the italicized errors in the Table. This compares well with the previous data set (Table 4), although is a little higher overall. The model also confirms the increase in solubilities for the experimental data at higher pressures for all temperatures.

43

Figure 2.6 shows isotherms of calculated solubilities using binary interaction parameters regressed from extraction solubility data. With increasing temperature, the predicted solubilities reduced, as expected, but only to about 16 MPa. The model predicted a convergence of solubilities at approximately 17 – 18 MPa, after which higher solubilities were predicted for higher temperatures, even though these conditions were at lower densities and hence had less solvating power. The crossover pressures were predicted at much lower pressures using extraction-based data compared with the cloud-point data (approximately 25 MPa). This trend was also observed experimentally with the extraction data reported, whereas the lower solubilities at higher temperatures was generally observed for the cloud-point data. The dynamic setup of the extraction method caused the quantity of AKD dissolved to depend not only on equilibrium conditions but also its ability to diffuse through the SCF [16]. Consequently, the density effect was more important at lower temperatures with operating pressure less than the crossover pressure while the diffusion kinetics were dominant at higher temperatures with operating pressures higher than the crossover pressure [182,183]. Retrograde vaporization is a phenomenon observed between the lower and upper crossover pressures on a mole fraction vs pressure phase diagram, in which the solubility of the solute decreases with an increase in temperature [182]. On either side of this region, the reverse is true, i.e., the solute solubility increases with increasing temperature [181,183]. Retrograde vaporization was therefore observed at most pressures with the cloud-point solubility determinations (refer Figure 4). Extraction solubility methods however revealed both retrograde vaporization and kinetic effects with an identified upper crossover pressure 17 – 18 MPa, both experimentally and via model prediction (Figure 6). Both of these phenomena led to an increase in AKD solubility.
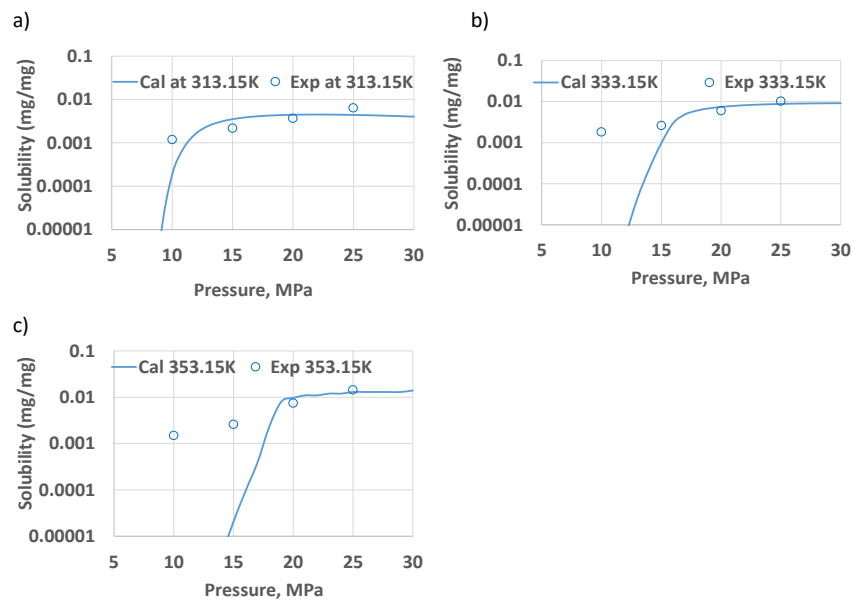
Figure 2.5: Comparison of extraction solubility of AKD in scCO2 [16] with the modeling at a) 313.15K, b) 333.15 K, and c) 353.15 K.
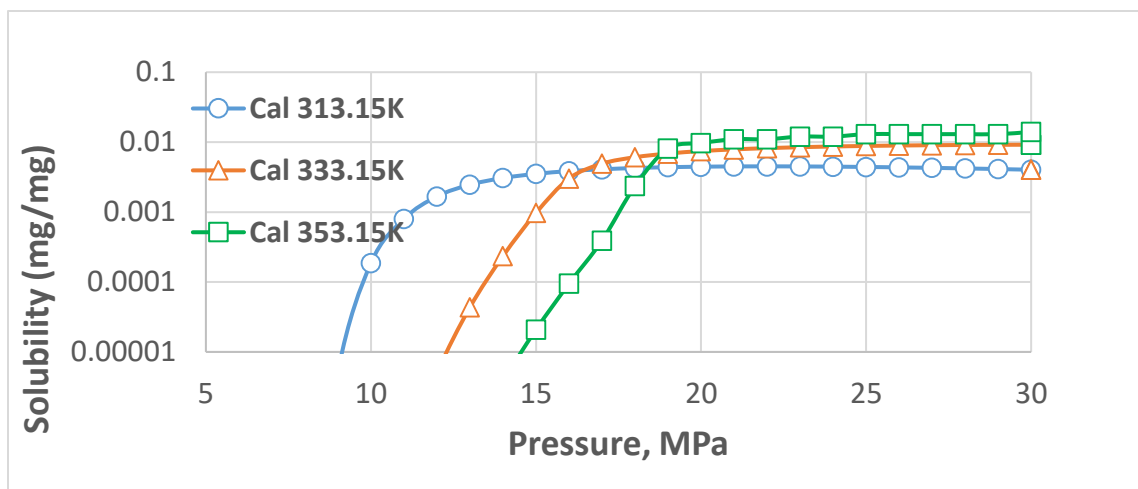
Figure 2.6: Isotherms of calculated AKD solubility in scCO$_2$ with binary interaction parameters regressed from extraction method.

Table 2.5: Comparison of the calculated solubilities with data obtained from extraction method. All AKD solubility experimental data were taken from Rodríguez-Meizoso et. al. [16].

Pressure (MPa)	Experimental solubility (mg/mg)	Calculated solubility (mg/mg)	Standard deviation (mg/mg)	Relative standard deviation %	Absolute relative error %
T = 313.15K					
10	1.20E-03	1.86E-04	7.17E-04	103.39	84.46
15	2.20E-03	3.52E-03	9.33E-04	32.61	59.95
20	3.70E-03	4.45E-03	5.30E-04	13.01	*20.27*
25	6.40E-03	4.41E-03	1.40E-03	25.97	*31.03*
T = 333.15K					
10	1.80E-03	1.67E-08	1.27E-03	141.42	100.00
15	2.60E-03	9.71E-04	1.15E-03	64.52	62.66
20	6.00E-03	7.44E-03	1.02E-03	15.14	*23.98*
25	1.02E-02	8.82E-03	9.78E-04	10.28	*13.56*
T = 353.15K					
10	1.50E-03	1.10E-09	1.06E-03	100.00	100.00
15	2.60E-03	2.08E-05	1.82E-03	97.29	99.20
20	7.40E-03	9.69E-03	1.62E-03	66.78	*31.00*
25	1.43E-02	1.30E-02	9.19E-04	62.58	*9.09*

2.3 The model validation

The aim of this work was to study how accurately the solubility of AKD in $scCO_2$ could be predicted using standard thermodynamic models, given the unavailability of its experimental critical properties and vapor pressure data. According to [104,144,165], a plot of ***ln**(solubility of the modelled data)* vs ***ln**(density or reduced density of pure CO₂)* should be linear for the model to be deemed "reliable". This linear relationship was demonstrated by Khimeche, Alessi Kikic and

Dahmani [104], in their experimental determination and correlation study of diamines solubility in $scCO_2$, where a simple linear plot resulted from *ln(solubility)* vs *ln(density of pure CO₂)*. **Figure 2.7** shows the existence of a linear plot between *ln(solubility)* vs *ln(density of pure CO₂)* for the modelled data correlated for cloud-point experimental data at 353.15 K and pressures from 7 – 30 MPa. The straight line confirms the accuracy and reliability of the model and indicates very good agreement of calculated solubilities with the experimental data. The pure CO_2 density was calculated from the method of Span and Wagner [184].

Figure 2.7: Validation of model showing linear relationship between ln(solubility) of AKD and ln(pure CO_2 density). Data points created with the model were performed at 353.15 K and pressures between 7 and 30 MPa.

2.4 Justification and limitations of the model

The aim of this work was to study how accurately the solubility of AKD in $scCO_2$ could be predicted using standard thermodynamic models, given the unavailability of its experimental critical properties and vapor pressure data. According to [104,144,165], a plot of *ln(solubility of the modelled data)* vs *ln(density or reduced density of pure CO_2)* should be linear for the model to be deemed "reliable". This linear relationship was demonstrated by Khimeche, Alessi Kikic and Dahmani [104], in their experimental determination and correlation study of diamines solubility in $scCO_2$, where a simple linear plot resulted from *ln(solubility)* vs *ln(density of pure CO_2)*. **Figure 2.7** shows the existence of a linear plot between *ln(solubility)* vs *ln(density of pure CO_2)* for the modelled data correlated for cloud-point experimental data at 353.15 K and pressures from 7 – 30 MPa. The straight line confirms the accuracy and reliability of the model and indicates very good agreement of calculated solubilities with the experimental data. The pure CO_2 density was calculated from the method of Span and Wagner [184].

Numerically, the calculated and experimental solubilities do not exactly match as demonstrated in Tables 4 and 5, particularly at lower pressures. Nevertheless, there is good agreement in their trend as well as order of magnitude, especially with the cloud-point solubility data. As pointed out by Rodríguez-Meizoso et. al. [11], the variance between the solubility methods considered in the study could be partly due to the presence of impurities in the solute. This could cause some discrepancies in the estimated solubilities since the likely presence of impurities was not addressed by the model. There is also a possibility of human and equipment error which could further compound the discrepancy between the calculated and experimental solubilities. However, some of the likely sources of errors could be minimized if the experimental data set were much larger – which would lead to regression of more representative binary interaction parameters as well as more accurate calculated solubilities. There is much better agreement of the calculated solubilities with experimental data at high pressures – the region of non-ideality. Most processes involving $scCO_2$ are carried out at high pressures where there are simultaneous effects of liquid-like density, unusually high diffusivity and significant increase in mass transfer [93]. Therefore, this model will be useful in predicting solubilities of solutes in these processes at the conditions mentioned. It should be noted that most of the physical properties used were estimated by GCEM, which might also be a source of error in the calculated solubilities.

2.5 Conclusions

This study shows a simple method to model the solubility of AKD in a supercritical medium in the absence of experimental physical constants. The EOS used provides reasonably good solubility estimates of the AKD-scCO$_2$ system, especially at higher pressures and for all temperatures. It should be noted that different solubility measurement methods produced different results. Therefore, proper understanding of data interpretation as well as knowledge of the experimental kola is set up are needed before applying the results. The solubilities are poorly predicted near the critical point, however showed very good agreement with the experimental data at higher pressures over a wide range of temperatures. Since dissolution of AKD in scCO$_2$ is usually carried out at higher pressures, the model will be very useful to provide reasonable estimates of the solubilities. Different GCEM produce different values of the physical constants, and hence the accuracy of the model hinges on the type and/or combination of GCEM used. Determination of some of these constants experimentally will improve the predictive capacity of the model. The findings in this study will complement the scarcity of experimental solubility data of AKD in scCO$_2$. This work is believed to be the first attempt made in the open literature to model the solubility of AKD in scCO$_2$, and paves the way for future model improvements which may include those at lower pressures or those with the added complexity of cosolvents within the AKD-scCO$_2$ mixture.

CHAPTER III

STICKY HYDROPHOBIC BEHAVIOR OF CELLULOSE SUBSTRATES IMPREGNATED

WITH ALKYL KETENE DIMER (AKD) VIA SUB- AND SUPERCRITICAL CARBON

DIOXIDE

Kolawole Adenekan, B. Hutton-Prager, Sticky Hydrophobic Behavior of Cellulose Substrates

Impregnated with Alkyl Ketene Dimer (AKD) via Sub- and Supercritical Carbon Dioxide,

Colloids and Surfaces A: Physicochemical and Engineering Aspects. 560 (2018).

3.1. Abstract

Cellulose fibers were impregnated with alkyl ketene dimer (AKD) dissolved in n-heptane and

carbon dioxide via sub- and supercritical impregnation techniques. The mechanistic pathways and

hydrophobic performance at short and long times were investigated by contact angle (CA)

analysis, scanning electron microscopy (SEM) with micrographs analyzed using Image-Pro

Premier, and Fourier Transform Infrared (FTIR) analysis. The sizing development was significant

after two days of treatment, and hydrophobic performance became uniform after two weeks

regardless of the impregnation conditions investigated. Samples prepared at 100 and 200 bar

produced more rapid development than those at higher and lower impregnation pressures, with the

average CA at 200 bar and 21°C being 140±5°. 'Sticky' hydrophobicity was observed on surfaces

treated at 200 and 250 bar at long times (> 140 days), and adhesive forces between the droplet (> 20 µL) and surface were observed at surface tilt angles between $0 - 180^o$. SEM micrographs of impregnated samples showed a reduction in substrate pore-size area (PSA) as hydrophobicity developed with time. There was little evidence of reaction-based sizing as the characteristic ketone and ester peaks were not observed in FTIR studies. The lactone ring remained intact. The 200 bar sample showed highest peak intensity for various hydrocarbon bonds observed – suggesting the optimal solubility of AKD in supercritical carbon dioxide ($scCO_2$). Spreading of AKD across the fiber surfaces appeared to be the main sizing pathway, and identification of hydrogen bonding between AKD and cellulose fibers suggested a possible attachment method.

3.2. Introduction

There has, in more recent years, been a shift in research from hydrophobic surfaces (contact angle, CA $\geq 90^o$) towards the development of superhydrophobic surfaces (CA $\geq 150^o$) in keeping with a generic theme for 'smart', 'innovative' or 'multifunctional' coatings [2,10,22,56,57,62]. These surfaces have been described as exhibiting the lotus effect [2], in line with early superhydrophobic studies of the lotus leaf. High water-repellency has also been reported on rose petals, though they have lower CA than superhydrophobic surfaces [2,22]. Surfaces that possess high water repellency have low surface energies and/or nano- or microscale roughness [10,25]. These properties are of particular importance as they impart desirable functionality on the surface such as self-cleaning; dust-removal; transport of microdroplets; anti-corrosion; anti-stick or anti-microbial capabilities [2,10,21,22]. Another area of particular interest is that of food packaging applications using paper substrates, where a highly water repellant surface would assist greatly in minimizing food spoilage.

Packaging materials are required to retain their specific properties for long times in order to maintain freshness of the food [90].

Additional measurements to quantify the hydrophobic property of a surface are contact angle hysteresis (CAH) and tilt angle or sliding angle (SA), especially for near or fully superhydrophobic surfaces [22,55,56,59,63]. CAH arises from an interfacial energy imbalance – when the required energy to form a new surface is less than the needed energy to separate the existing surface. It is determined by the difference between advancing and receding CAs. The difference in CAH for various hydrophobic surfaces arises from the contributing effects of physical and chemical modifications [54,60]. Roughening a surface physically modifies it while chemical modification is achieved by breaking or forming new active bonds [60]. The fabrication of mildly to highly hydrophobic surfaces is determined by CAH. As a rule of thumb, in addition to the CA requirement, true superhydrophobic surfaces also have CAH < 10$^\text{o}$ and SA < 5$^\text{o}$ [57]. If CAH > 10$^\text{o}$, SA >> 5$^\text{o}$, and CA near but less than 150$^\text{o}$, the droplet may stick to the surface like that of rose-petals [22,57,60,62]. Rose petals' relatively high CAH and SA as well as its textured morphology favor the development of high-water adhesion [2].

Droplets stay on tilted surfaces when the gravitational force is balanced by the force of adhesion [64]. Adhesion of a droplet to a surface is a function of CAH. Adhesion of droplets to substrates follows two theoretical models [64] which are: contact-area; and length of the liquid-solid interface models. The forces of adhesion – lateral (F_L) and retentive (F_R) – generate metastable and barrier energies respectively [22,54,63,64]. These energies arise from chemical heterogeneity, surface roughness, contact line topography and the area occupied by the droplet [54,60] which are functions of both lateral and retentive forces of adhesion. Metastable energy is developed from the

fraction of contact area between liquid-solid interfaces and chemical modifications and describes the energy that enables a droplet to laterally move across a surface. Barrier energy is the ability of a droplet to "stick" to a surface [22]. Surfaces where $F_L \geq F_R$ generally describe superhydrophobic surfaces, while surfaces where $F_R \geq F_L$ describe "sticky" hydrophobic surfaces.

Cellulose (paper) substrates by default exhibit high surface energies due to high polarity from the –OH groups in their molecular structure, and internal sizing is frequently performed in the papermaking industry to improve water repellency [2]. These –OH groups have high affinity for water to create hydrogen bonds. Therefore, cellulose is a water-loving substance by its chemical nature. Preparation of hydrophobic surfaces on highly hydrophilic materials such as cellulose relies on utilizing the rough and porous structure to achieve sufficient hydrophobic development [2]. As a common practice, all the techniques and methods for increasing hydrophobicity of any material aim at lowering the surface energy and increasing the surface roughness [1,36].

Alkyl ketene dimer (AKD), a waxy material derived from fatty acids, is a sizing agent typically introduced into the wet end of the papermaking process at $0.1 – 0.5\%$, dispersed within water-soluble cationically modified starch [75,79]. The melting point of AKD ranges between 40 - 60°C depending on the dimer chain lengths which are typically 14 to 20 carbons [11,13,79]. Much of it is lost during the dewatering and paper-forming stages, although as little as 4% fiber surface coverage is required for sufficient hydrophobic development of the fibers [185].

Alternative methods of AKD sizing have been explored to develop superhydrophobic surfaces over cellulose fibers with more uniform distribution. Some of these methods include sub- and

supercritical impregnation of AKD onto cellulose fibers [9,11,13,94,117]; rapid expansion of a supercritical solvent (RESS) [13,74,143,186]; and the addition of specific nanoparticles in the AKD mixture to promote the hierarchical multi-scale roughness [1,27,41]. These methods have frequently resulted in substrates being more hydrophobic than those prepared via traditional methods. While nanoparticle addition assists in improving the surface roughness [15,29,52,110], impregnation methods with sizing agents promote significantly better diffusion and hence penetration into the substrates [23]. The agent itself will be more uniformly distributed over the fibers with much greater efficiency than the more traditional 'wet-end' methods of soaking fibers in a mixture of chemicals [187]. The CO_2 diffusivity is a factor 100-1000 times larger than most liquids [188], and therefore can better penetrate into the pores of the substrate [2,151].

Given the growing body of researchers using high pressure impregnation techniques to generate superhydrophobic surfaces, it is advantageous to explore the surface and interfacial phenomena surrounding these surfaces. Specifically, this study focuses on identifying (a) the surface energy behavior of cellulose substrates with time as a result of high-pressure CO_2 impregnation treatment with AKD; (b) the structural changes occurring on the substrate after treatment; and (c) the chemical interactions occurring both on the surface and between AKD and cellulose fibers, providing information on possible sizing mechanistic pathways. CA, CAH and SA studies were utilized to gain relevant surface energy information of the treated surfaces and also identify unusual surface behavior. Scanning Electron Microscope (SEM) imaging and subsequent image analysis enabled structural changes with time to be identified, and Fourier Transform Infrared (FTIR) measurements provided key information regarding both interfacial and surface chemistry.

3.3. Material and Methods

3.3.1 Materials

AKD wax (Aquapel^{TM} 364K sizing agent) was supplied by Solenis, containing chain lengths of C_{16}/C_{18}. AKD/heptane solutions (1.8 g/L) were prepared from recrystallized AKD wax and analytical grade *n*-heptane (99.5%, Sigma Aldrich). Supercritical fluid grade carbon dioxide, scCO$_2$ (<50ppm moisture, Airgas USA, LLC) was used as the carrier fluid to dissolve the AKD/heptane solutions, while heptane represented the cosolvent [9,11,13,127–129,135]. Whatman filter paper no.1 was used as the cellulose substrate in these experiments. **Figure 3.1** shows molecular structures of AKD, its fatty acids and hydrolyzed form (β-keto acid), and some likely attachments of AKD to the cellulose substrate.

3.2.2 Methods

Supercritical impregnation of cellulose substrates was conducted using supercritical equipment built in-house. **Figure 3.2** shows a schematic diagram of this set-up. Briefly, CO$_2$ was pressurized to predetermined pressures of 50, 100, 150, 200 and 250 bar, and then pumped around the circulating loop containing vessel 1, which held the AKD/heptane solution. This circulating loop was maintained at a constant temperature of 21°C within a water bath unless otherwise indicated. The circulation was maintained for 10 min, and then valve V2 was opened to allow the combined solution into vessel 2, which held the Whatman filter paper. After 15 minutes of impregnation time, the CO$_2$ was released into the fume hood during depressurization by opening valve V3, and

the treated paper sample collected for further analysis. The hydrophobic development was monitored up to 140 days after the impregnation treatment.
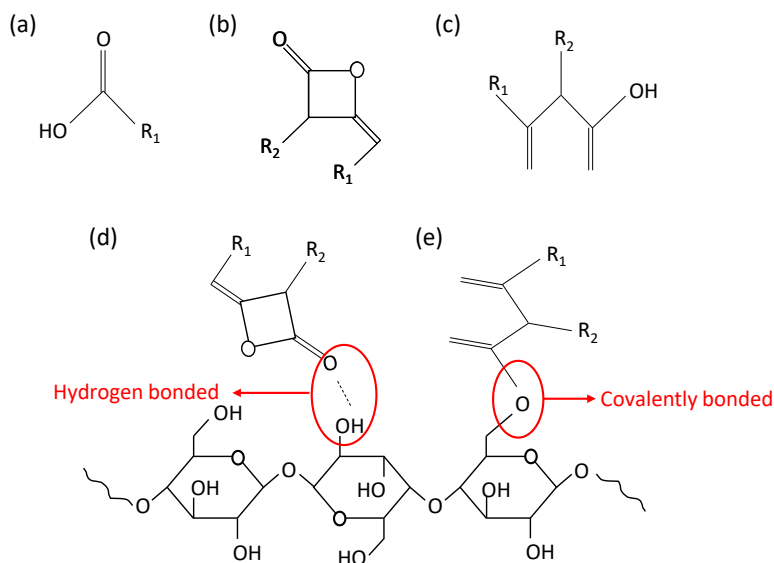
Figure 3.1: Molecular structure of (a) unreacted fatty acids making up AKD; (b) AKD; (c) hydrolyzed form of AKD, or b-keto acid; (d) AKD hydrogen-bonded to cellulose; and (e) reacted form of AKD covalently bonded to cellulose. Note that R1 and R2 are typically from C16-C18. These diagrams are representative only.
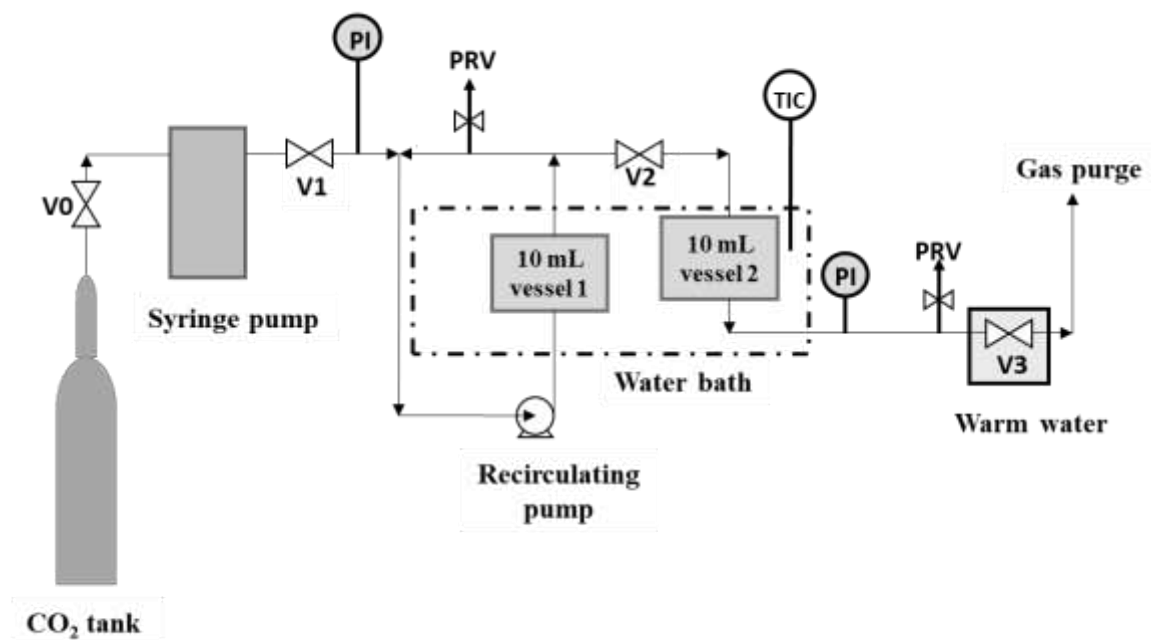
Figure 3.2: Schematic diagram of the supercritical rig designed in-house to undertake impregnation studies.

FTIR Spectroscopy using a Cary 630 (Agilent Technologies) was used to capture changes in the sizing development of the treated substrates over time. Attenuated Total Reflectance (ATR) mode was used, in which the incident light was totally-internally reflected and sufficiently interacted with the sample. Transmittance data was analyzed to identify critical peaks relating to AKD and chemical bonds between AKD and cellulose fibers.

Sessile drop experiments enabled the determination of static and dynamic CA, using a Biolin Scientific OneAttension Theta CA Analyser, coupled with a single-liquid automatic dispenser, inbuilt NAVITAR (model 520931) and OneAttension software. The droplet volume was measured at 10 μL for all measurements (CA, CAH and SA), while the drop rate was kept at 1 μL/s.

58

Deionised water was used as the working fluid. CAH was measured by a volume-changing method [54,55,60,61] from 2 to 10 µL. Advancing and receding CAs were measured at the same volume. CAH was then calculated from the difference between advancing and receding CAs. The SA was measured by placing a 10 µL droplet volume on the treated substrate with the aid of the Biolin Scientific OneAttension. A tweezer was then used to lift the substrate from the stage. The SA is 0° when the sample is horizontal and 90° when vertical in accordance with Extrand and Moon [58]. Greater than 20 µL droplets were applied to treated substrates to assess the F_R. The SAs were estimated with respect to the horizontal and vertical directions, and not accurately positioned. The sample was manually shaken slowly, parallel to the SA, until the droplet became detached from the sample.

The *surface morphology* of the treated cellulose samples was examined periodically after the impregnation treatment until complete hydrophobicity was achieved, using a JSM-5600 SEM (JEOL USA Inc., Peabody, MS). Samples were pre-coated for 120s with gold particles using a Hummer 6.2 sputter coater (Anatech USA, Union City, CA) – the coating was done under near-vacuum conditions to ensure effective coating. The images were taken at different magnifications (x70, x200, x1000, x3000) using an accelerating voltage of 5kV.

Image analysis was performed using Image-Pro Premier (version 9.3.3, Media Cybernetics, Rockville MD) to process and characterize the SEM images of impregnated substrates as the sizing developed with time. Changes in the microporosity of the substrate were examined and quantified [189]. A combination of thresholding and bitmapping techniques were used to quantify the pore-size distribution and porosity. With thresholding, the images were converted to gray scale between

0 and 255. A level of 0 indicated a pure black color while one at 255 was pure white. Gray values of 0 to 62 were representative of the substrate pores for untreated cellulose at x70 magnification, determined by manually adjusting the threshold level within the software until all pores were included. Demonstration of the thresholding technique is shown in **Figure 3.3**. Untreated samples were expected to have the largest pore areas compared with impregnated samples. Bitmapping allowed every pixel within an image to be assigned a gray value. The proportion of pixels falling within the pore-size category as determined by thresholding was calculated using **Equation (3.1)**:

$$\%PSA = \frac{P_P}{P_{TOT}} * 100 \qquad\qquad (3.1)$$

In this Equation, %PSA is the percentage pore size area; P_P is the number of pixels representing the pores; and P_{TOT} is the total pixel size of the image. %PSA is not a measure of true porosity of the cellulose substrate but a technique to quantify the changes in the micro pores as hydrophobicity develops.
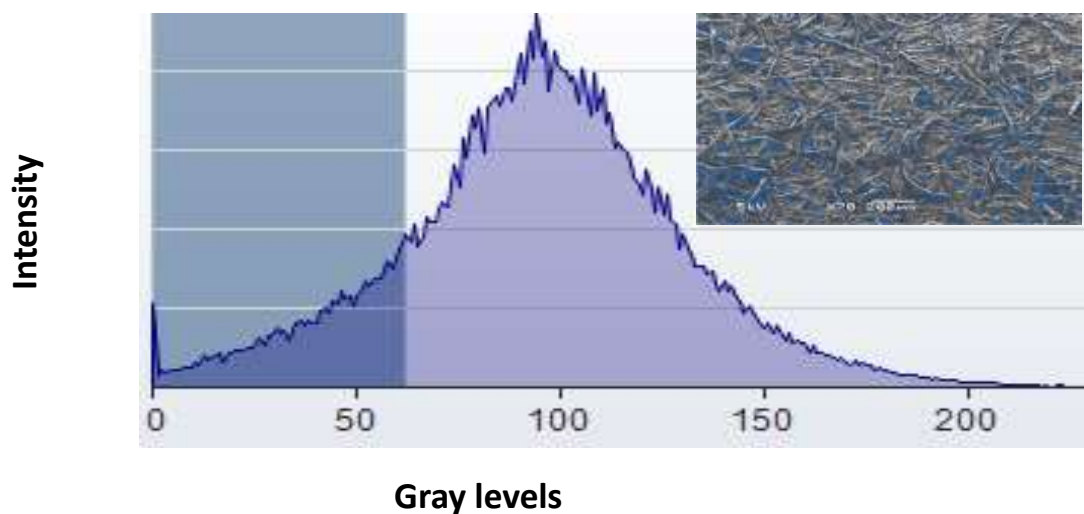
Figure 3.3: Demonstration of the thresholding technique showing a normal distribution from image analysis of untreated cellulose substrates. The highlighted gray values between 0 and 62 identify the pore areas in the processed image.

3.3 Results and discussion

3.3.1 Surface Energy Behaviors of Treated Substrates

Changes to roughness and chemical heterogeneity of a surface alter its wettability. Low energy surfaces with high roughness will lead to an improvement in the hydrophobic behavior of the surface, and these effects can be captured by CA measurements of impregnated substrates and compared with untreated substrates.

3.3.1.1 CA development with time

CA measurements were taken periodically to capture the hydrophobic development of the treated substrates. **Figure 3.4(a)** compares CA on an untreated substrate with one immediately after AKD impregnation treatment at 250 bar. The untreated surface started with a CA of about 30º and

61

quickly dropped to nearly zero after 3 seconds. The treated surface started with a CA of about 130°

but equaled that of the untreated surface after 1 second; they both dropped to nearly zero after 3

seconds. This result confirms that although there were small surface changes, there is no

appreciable hydrophobicity created immediately after treatment.

Two days later, as shown in **Figure 3.4(b)**, CA measurements of treated cellulose over the four

pressures investigated (50, 100, 200, 250 bar) had increased substantially. The treatments at 100

and 200 bar created the most hydrophobic surfaces at this time, with steady-state CA values

between approximately 118 – 124°. The highest and lowest pressure conditions indicated less

hydrophobic development. This tends to indicate an optimal solubility of AKD/heptane in scCO$_2$

at the intermediate pressures of 100 – 200 bar.

The hydrophobic development over much longer periods of time is shown in **Figure 3.4(c)**. Here,

the four treatment pressures are again compared, up to 133 days from impregnation. Between 0-

20 days there is variation observed among the different conditions; between 20-40 days these

variations have started to settle; and from 40 days onward, all surfaces, regardless of their

impregnation treatment, appear to have approximately similar hydrophobicity. All CAs vary

within about 10° at 133 days. Repeatability studies of CA show a typical variation of identical
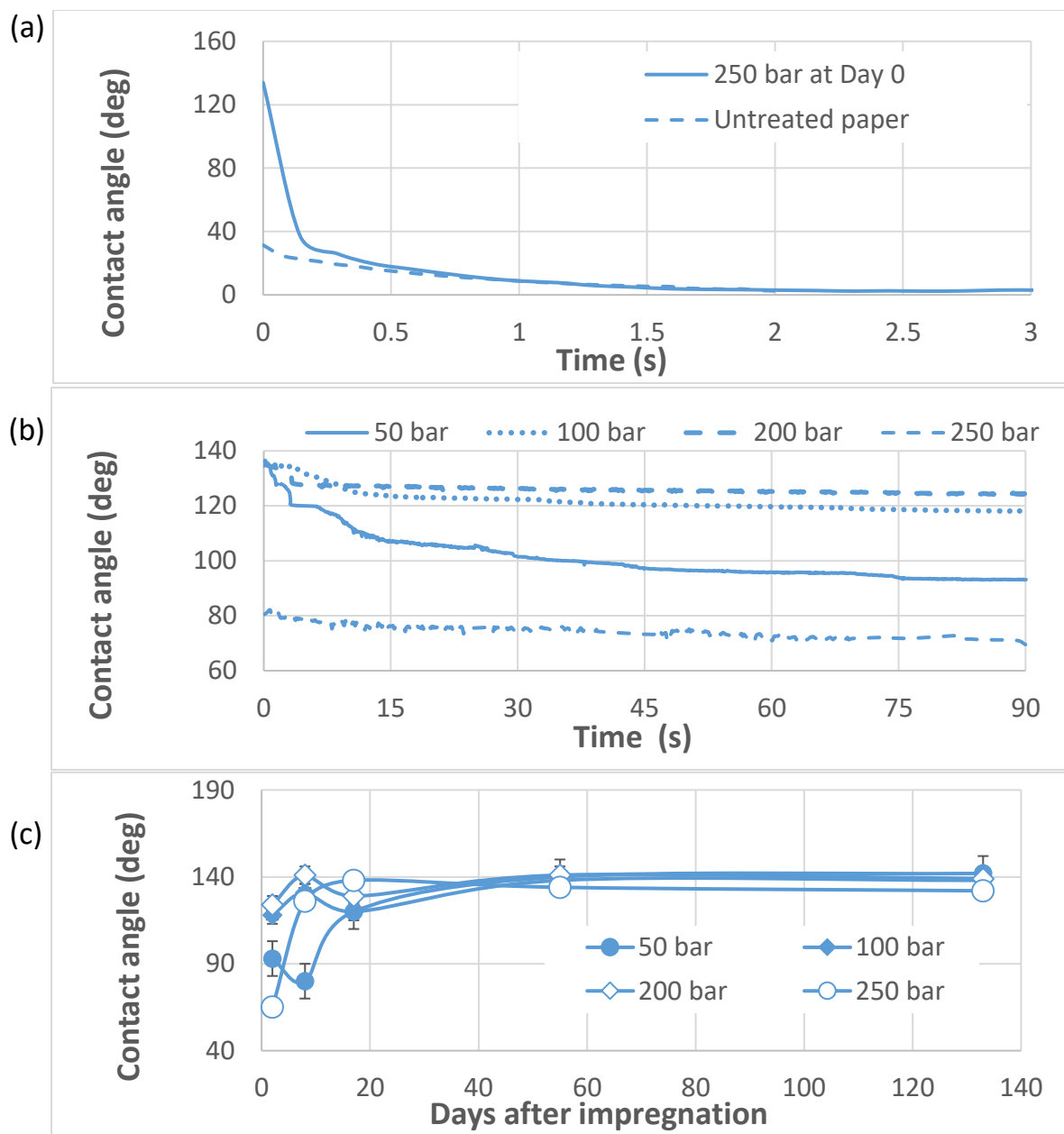
Figure 3.4: (a) Dynamic CA analysis immediately after AKD impregnation treatment on day zero (scCO$_2$ / AKD / heptane, 250 bar), compared with untreated cellulose. (b) CA analysis of hydrophobic development two days after AKD impregnation treatment (scCO$_2$ / AKD / heptane) at various pressures. (c) Rate of hydrophobic development of substrates impregnated with AKD at different pressures (scCO$_2$ / AKD / heptane) up to 133 days after treatment.

conditions of $\pm 5^{\circ}$, as indicated by the error bars on this graph. Therefore, the apparent peaks and troughs shown between 0-20 days are mostly within experimental error, and describe more generally an increase in CA from day 0 to steady state following typical power law behavior. These results again suggest optimum solubility between 100-200 bar and a more rapid hydrophobic development to steady state values compared with 50 and 250 bar.

3.3.1.2 Droplet behavior

The difficulty of the droplet breaking away from the syringe on treated cellulose samples at 2-3 days after the impregnation treatment was observed along with a much slower depth of penetration and resistance to horizontal spreading. Droplets placed on untreated substrates had no difficulty breaking away from the syringe due to the high surface energy and relatively large pore size of the cellulose substrates [37]. This was also reported by Hutton and Parker [9]. **Figure 3.5(a)-(c)** shows the patterns of droplet release from the syringe and confirmed the progression of the hydrophobic improvement of untreated and treated substrates at 250 bar. Figure 5(a) shows the behavior of the droplets on untreated cellulose substrates; 3.5(b) for impregnated substrates immediately after treatment; and 3.5(c) for impregnated substrates 154 days after treatment. The droplet behavior on treated substrates indicates the much lower surface energy created by AKD impregnation.

At long times after the impregnation treatment, the behavior of the impregnated surfaces mimic those of rose petals where droplets stick to the surface, even when the CA does not theoretically indicate superhydrophobicity [22]. **Figure 3.5(d)** shows how the droplet appeared glued to the surfaces irrespective of how much it was tilted or rotated, at long times since impregnation. This behavior is attributed to adhesion between the surface and the droplet and the concomitant effect

of roughness and low surface energy [22,26]. Similar observations were reported by Wang and Weiss [22], where petal-like surfaces were created from lightly sulfonated polystyrene (SPS) ionomer particles on silica substrates by rapid evaporation of the solvent from a dilute polymer solution-cast onto silica. It was reported that a particle-textured surface was a necessary requirement for the fabrication of sticky hydrophobicity. Evaporation rate of the solvent was cited as one of the main factors promoting the formation of a submicron to micron particle-textured surface. This effect may be likened to the rapid depressurization and removal of the CO_2-solvent, leaving behind only the solute to create a similar particle-textured surface. In this work, the average CA measured when sticky hydrophobicity was also observed was about 140°, and the CAH of the 200 bar sample was 17 ± 5°, taken 200 days after treatment.

a) 0.5 s — 1.37 s — 1.44 s — 1.66 s

b) 1.30s — 1.73s — 1.87s

c) 4.03s — 4.18s — 4.32s — 4.61s

d) Approx. 90° tilt — 90 – 150° tilt — 180° tilt — 180° tilt
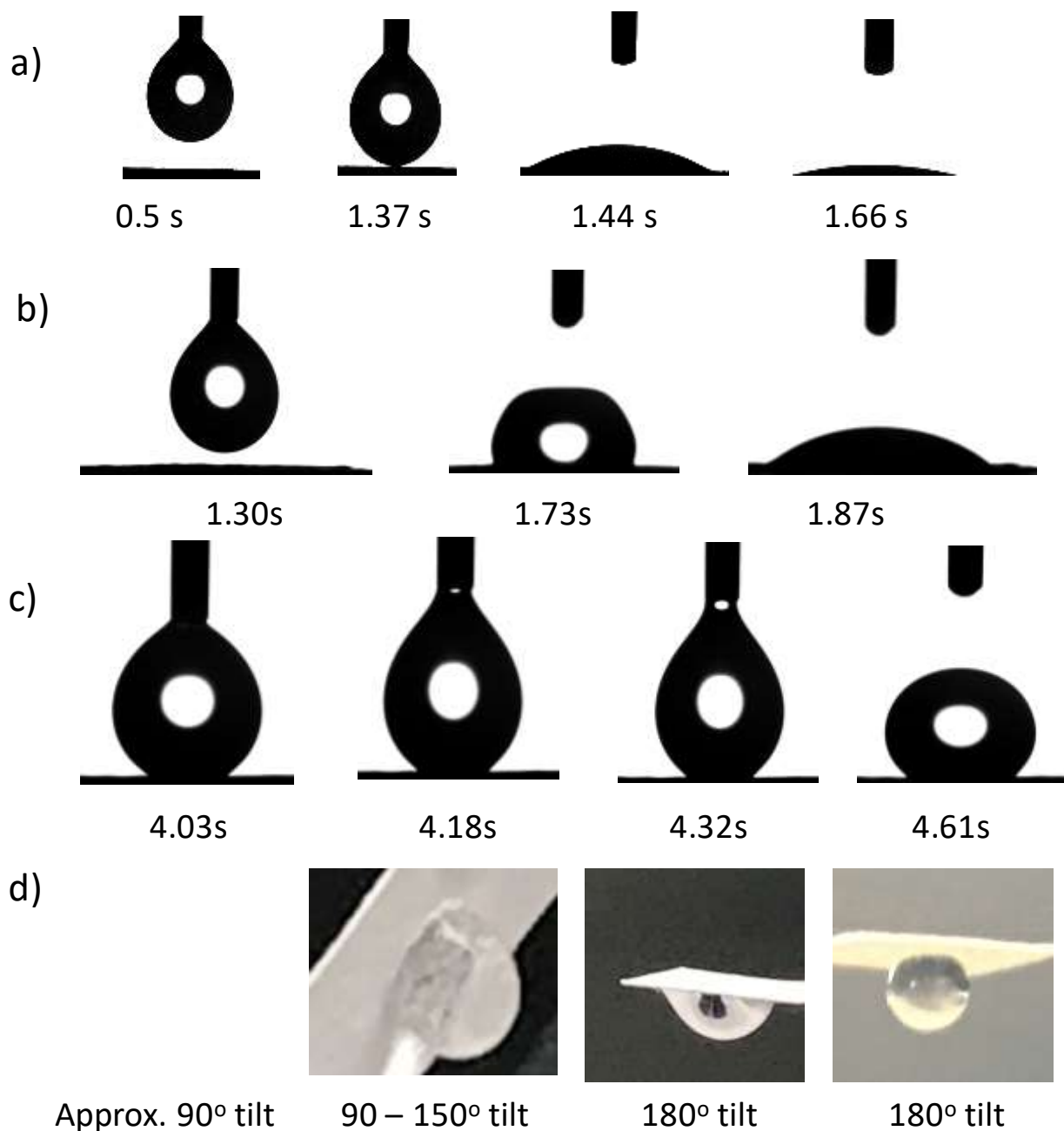
Figure 3.5: Water droplet behavior on different surfaces. (a) untreated cellulose; (b) immediately after impregnation treatment (scCO₂ / AKD / heptane) at 250 bar; and (c) 154 days after impregnation at the same conditions. (d) 'Sticky' hydrophobicity of 10 μL droplets at various tilt angles, taken 6 months after treatment, the final image being at 200 bar impregnation instead of 250 bar.

3.3.1.3 The force of adhesion

The force of adhesion of the 10 µL droplet, as judged by the images in Figure 5(d), was able to withstand a surface tilt to any angle, and remained stuck to the surface even when slowly shaken. The F_L developed when the surface is tilted is given by **Equation (3.2)** [22,63,64], where ρ is the density of water; g is the gravitational acceleration; V is the droplet volume; and α is the SA.

$$F_L = \rho g V \sin\alpha \qquad\qquad (3.2)$$

Equation (3.3) describes the F_R [22,63,64], where R is the characteristic length representing the shape and size of the droplet; k is a constant of proportionality; γ_{LV} is the interfacial tension between the droplet and the air; θ_a is the advancing CA; θ_r is the receding CA.

$$F_R = kR\gamma_{LV}(\cos\theta_r - \cos\theta_a) \qquad\qquad (3.3)$$

Any change in drop volume and/or SA results in a corresponding change in F_L. F_R is characteristic of a surface and does not change when the droplet volume and/or tilt angle are changed. Equation (3.3) is based on the prediction of CAH to determine the SA [64]. Surfaces prepared at 200 and 250 bar, and investigated at long times (>140 days) withstood a maximum of 23 µL droplet volume when tilted to 90°, but with less retention time than 10 µL tilted to the same angle. Using these numbers and Equation (3.2), F_L was calculated to be 225 µN. To create a superhydrophobic surface, F_R must be less than 225 µN to ensure droplet roll off.

Two common models used to describe hydrophobic surfaces are the Cassie-Baxter and Wenzel models. In the Cassie-Baxter model (**Equation(3.4)**), f is the fraction of the air-liquid interface, r is the rough surface area divided by flat projected area, θ is the measured CA on the porous surface and θ_0 is the intrinsic CA on an original smooth surface [10,30,190]. The model demonstrates that the presence of air-pockets at the droplet-solid interface plays a vital role in the observed droplet behavior. When the air-liquid interface fraction is zero (f=0), the Cassie-Baxter model reduces to Wenzel model. According to Nicolas [26], sticky behavior of water on hydrophobic surfaces is governed by Wenzel theory where water droplets follow the path of surface roughness. The effects of capillary and Van der Waals forces favor the retentive adhesion of water to the surface [26].

$$\cos\theta = r\cos\theta_0 - f(r\cos\theta_0 + 1) \qquad (3.4)$$

Balu and Breedveld [54] proposed that the fabrication of sticky and roll-off superhydrophobicity is determined by the difference in metastable state energy and barrier energy. If the droplet makes sufficient contact with a surface, this favors an increase in the energy barrier, and a corresponding low metastable state or lateral adhesion force. SEM studies described in **Section 3.3.2** show that the surface had a multi-scale textured roughness, which favored the sticky hydrophobicity state according to Wang et al. [22]. The reluctance of the droplet to move easily on the impregnated surface indicated that the droplet occupied sufficient contact area and hence was not displaying superhydrophobicity. When the surface was tilted and lightly agitated, more air pockets replaced the solid-liquid contact; and the droplet fell off because the metastable energy overcame the energy barrier.

3.3.2 Structural Changes to Treated Substrates

Figure 3.6 shows the SEM micrographs of untreated and impregnated cellulose fibers at x70 and x1000 magnifications for varying processing conditions. Visual examination of the SEM micrographs showed that the substrate pores were reducing with time. These changes in pore-size area were quantified, and are shown in **Figure 3.7**. The PSA decreased from 16.1% on untreated cellulose to 6.5%, 10 days after the impregnation treatment at 150 bar pressure. The reduction in PSA was matched with a significant increase in the CA, subsequently lowering the surface energy. The CA data shows that the 250 bar sample did not demonstrate as rapid early hydrophobic development compared with 100 and 200 bar (see Figure 3.4(c)). Likewise, this data had higher PSA values compared with 150 bar and 200 bar, at 10 days after impregnation. The PSA for the 200 bar condition showed only a small reduction in PSA between 10 and 23 days (approximately 2%) with a final value of just over 2%. Although there is some experimental variation in CA during this time, at long times, the CA has similar values to those recorded between 10-23 days. Hence, porosity of around 2% seems sufficient for complete sizing development to near superhydrophobic values.
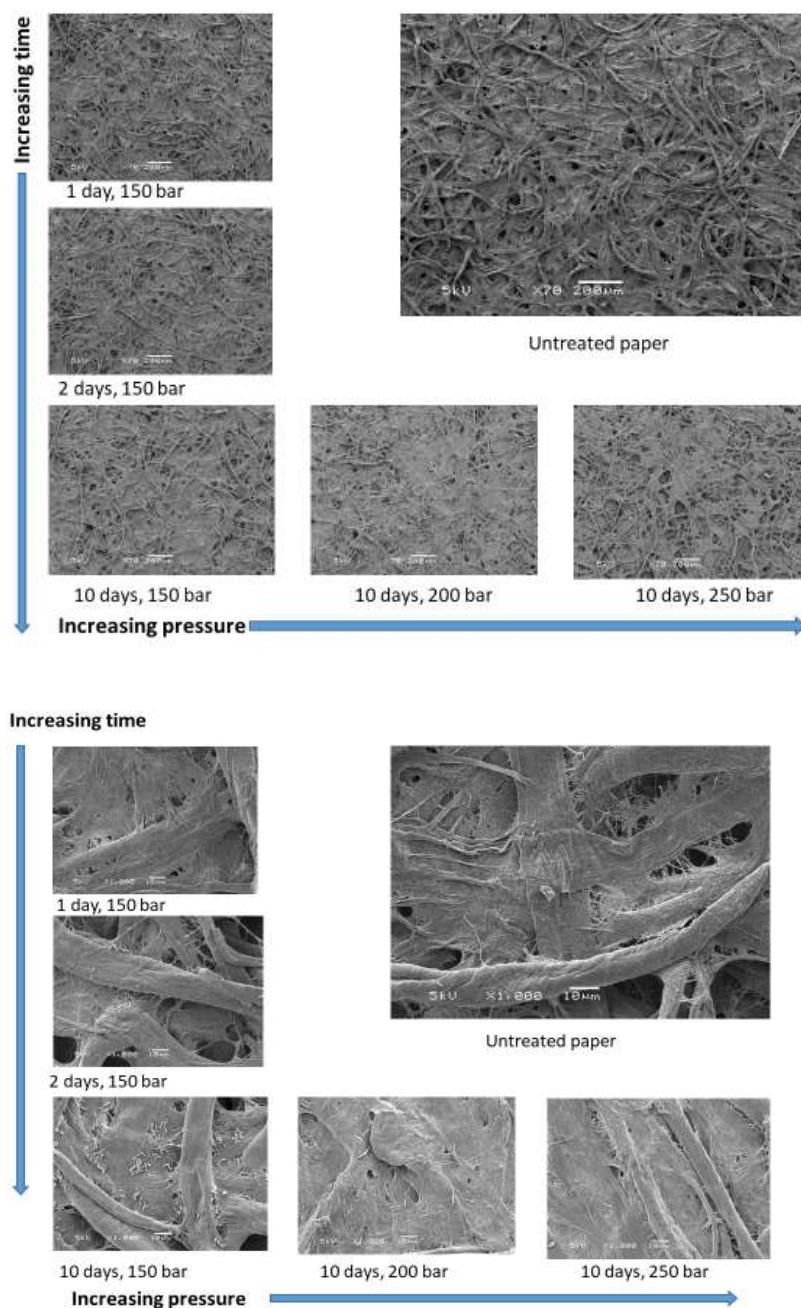
Figure 3.6: SEM micrographs of AKD impregnated substrates at (a) x70 and (b) x1000 magnifications. Vertical variation is with time at 150 bar pressure. Horizontal variation is with pressure at 10 days. These are compared with untreated cellulose substrates. Note the minimum porosity at 200 bar, 10 days, and the gradually reducing porosity with time at 150 bar.
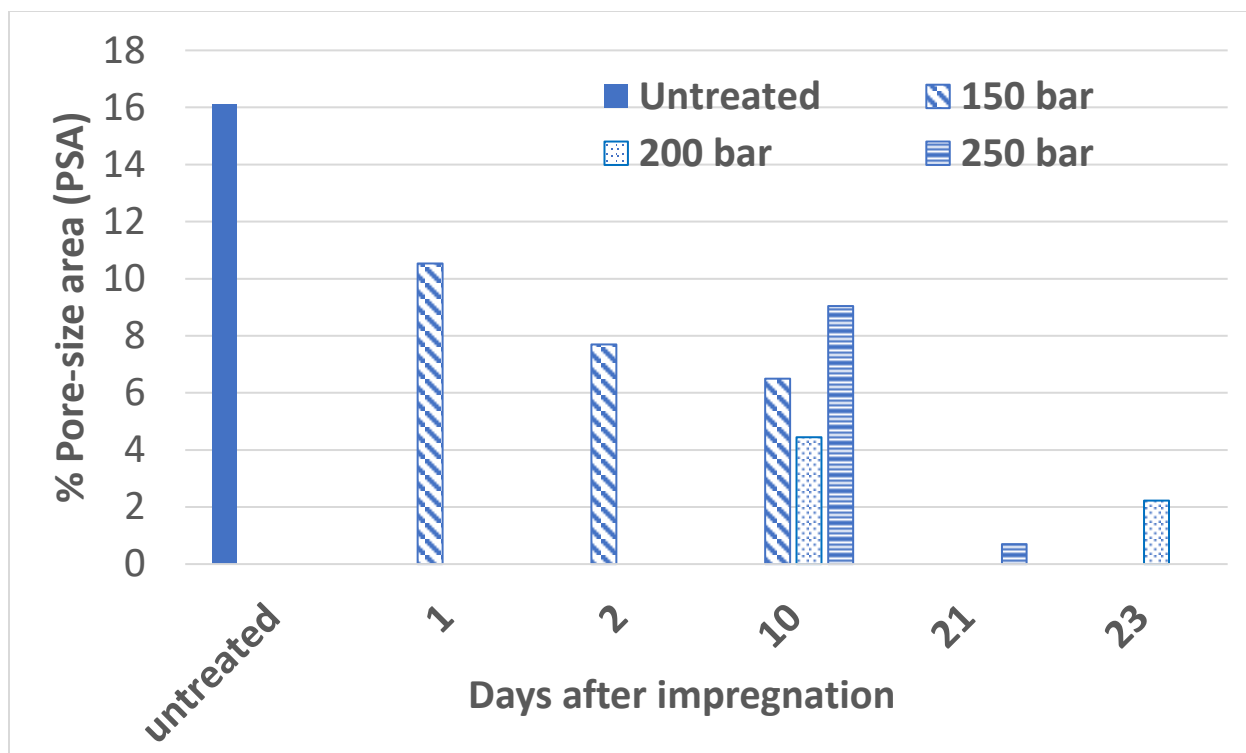
Figure 3.7: Image analysis using the thresholding technique, showing a reduction in pore size area (PSA) as AKD progressively covers the cellulose substrate pores at different impregnation pressures. The %PSA is based on Equation (1).

Zhang, Lu, Qian and Xiao [10] pointed out that hierarchical micro-/nano-structure has a pronounced effect on the sizing development. Jiang, Tang, Clinton, Breedveld and Hess [25], however, established that micro porosity influences superamphiphobic and/or superhydrophobic development more than nanoscale roughness [25]. Dual-roughness (micro and nano) and low surface energy are believed to be key determinants in the fabrication of water repellency [2,13], as are textured surfaces [22]. The presence of AKD on the substrate lowered the surface energy, and observed reduction of the pores with time enhanced roughness. The sizing was attributed to the AKD migrating across the fiber surfaces with time, increasing the hydrophobicity of the substrate

and matching the observed increase in CA. Although some pores reduced in size, sufficient porosity was maintained.

3.3.3 Surface and Interfacial Chemical Bond Identification

3.3.3.1 AKD and related peak identification

The same impregnated samples prepared and analyzed for CA studies underwent FTIR analysis at similar time periods from impregnation: 3, 9, 18 and 69 days. A baseline, plain cellulose scan taken on the same day as the trials was subtracted from the scans in order to *identify key peaks relating to AKD*. Those of interest were the $-CH_2$ bending (1465-1469 cm^{-1}) and $-CH$ stretching (2850-2960 cm^{-1}) [191]; hydrolyzed AKD or ketone peaks at 1704-1708 cm^{-1} [138]; ester peaks due to reaction of AKD with the cellulose at 1735 cm^{-1} [191]; and evidence of the lactone ring in AKD via C=C (1719-1723 cm^{-1}) and C=O (1842-1850 cm^{-1}) [138]. A final set of peaks of interest were broad bands occurring between 2500-2800 cm^{-1} representing $-OH$ stretching vibration from unreacted fatty acids [138], and another between 3200-3600 cm^{-1}, representing $-OH$ stretching vibration from alcohol $-OH$ [192]. This latter peak was described as being broad due to contributions from hydrogen bonding.

Figure 3.8 shows an example of the FTIR peaks with the cellulose baseline subtracted, three days after AKD impregnation treatment at 50, 100, 200 and 250 bar. These scans have been vertically translated to separate them from each other. Some of the key peaks outlined above are identified on this Figure in the shaded regions. There is little evidence of ketone peaks at 1704 cm^{-1} or ester peaks at 1735 cm^{-1} indicating a lack of hydrolyzation of AKD and subsequent reaction with the –

OH groups from the cellulose (refer Figure 1). Small but definite peaks appear at around 1719 cm^{-1} and 1848 cm^{-1}, which are representative of the C=C and C=O bonds present in the lactone ring, respectively. This is particularly obvious for the case performed at 200 bar, and also suggests that the AKD ring has not been broken to form β-keto acid (hydrolyzed form of AKD). Strong evidence of bending and –CH stretching is observed in all FTIR scans, as expected given the long hydrocarbon tails present on AKD. No peaks relating to –OH groups from unreacted fatty acids were observed; however, broad peaks between 3000-3400 cm^{-1} were frequently observed, potentially indicating hydrogen bonding between –OH groups from the cellulose and C=O from the AKD lactone ring (not shown in Figure 3.8).
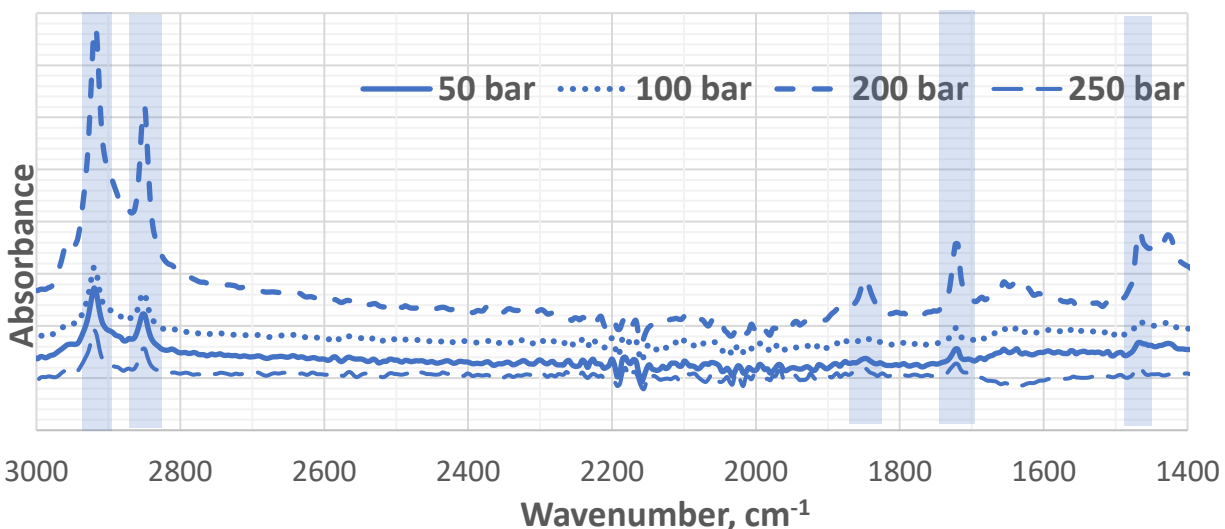
Figure 3.8: Example of AKD FTIR traces obtained three days after impregnation treatment (scCO$_2$ / AKD / heptane) and varying pressures, with cellulose baseline removed. The shaded areas refer to key AKD peaks as described in the text.

3.3.3.2 Distribution of AKD through the cellulose substrate

The absorbance heights representing concentration were more difficult to interpret, and essentially do not follow any observed trends. High pressure impregnation treatments are *assumed* to uniformly distribute the solute throughout the substrate matrix [21], and while this assumption is plausible, fiber porosity is itself random and deposits would therefore be randomly distributed within these pores. Additionally, the mechanistic pathways of AKD sizing (whether by reaction or spreading) are known to take up to two weeks [187], and hence there is a slow movement of AKD within the substrate with time. Since small portions were cut from the prepared samples for FTIR testing, it is possible, particularly at early times after treatment, that the portions removed may have contained substrate regions that were not yet populated by AKD. Likewise, it is also possible that a portion removed may have contained a large AKD deposit that had not yet had time to spread to other regions of the substrate. This explanation is depicted in **Figure 3.9**, where 3.9(a) shows AKD uniformly dispersed onto cellulose fibers soon after impregnation, and the dotted line areas represent portions removed for FTIR analysis. At some time later (Figure 3.9(b)), the initial deposits of AKD have spread further across the fibers and again the dotted line areas represent possible portions removed for analysis.

This AKD-spreading description is well-matched to the SEM images and analyses in Section 3.2, where progressive spreading with time results in a reduction in porosity. Hence direct trends such as increases in absorbance vs time at key wavenumbers was not expected. The only exceptions would be an increase in absorbance of the ketone peak representing hydrolyzation of AKD (an intermediate for AKD reaction with cellulose); and the ester peak demonstrating reaction of AKD

with cellulose –OH groups. The broad –OH bands representing hydrogen bonding between AKD and cellulose would register as a reduction in intensity coupled with a red-shift of the peak [193].
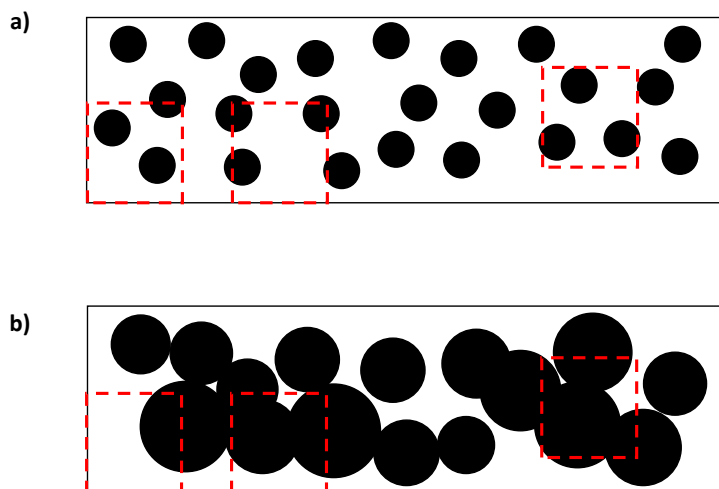
Figure 3.9: Schematic diagram demonstrating the sampling technique of cellulose substrates impregnated with AKD, and the potential implications on the peak intensities observed. (a) dashed square sampling portion of the total substrate at early times after impregnation; (b) dashed square sampling portion of the total substrate at long times after impregnation. The small black dots represent initial AKD deposits onto the cellulose fibers, and larger dots represent joining of these deposits as the AKD spreads across the surface.

3.3.3.3 Progression of key peaks with time

Figure 3.10 shows absorbance vs time of key wavenumbers at different operating pressures. These have been graphed using the same vertical scale to better compare absorbance heights. Figures (a)-(c) all show appreciable absorbance peaks for most of the conditions investigated, indicating the presence of the long hydrocarbon chains on the AKD molecule (refer again to Figure 1 where its structure is shown). As described earlier, there is no obvious trend for a given set of conditions over a period of time; however, frequently the 200 bar case featured as a more significant peak. Figures 3.10 (d) and 3.10 (e) show small but measurable absorbance peaks of the C=O and C=C lactone rings, suggesting that the ring was not broken in a reaction with the cellulose. Again, the conditions at 200 bar often featured in the highest intensities observed, and this may indicate – as with the CA studies – that these conditions promoted optimal solubility of AKD/heptane solutions into $scCO_2$ solvents. By contrast, Figure (f) showed virtually no absorbance activity at the ketone peak absorbance, and there was none at all of the ester peak, regardless of time. Finally, Figure 3.10 (g) shows the absorbances of the broad bands representing –OH stretching and the likely existence of hydrogen bonding. It is somewhat significant that intensities were more abundant at the various operating conditions tested from 18 days onwards, entering the time in which sizing development of AKD is considered mostly complete (refer Figure 4(c)). Additional data at 133 days testing continued to show dominant –OH peaks in the FTIR traces.
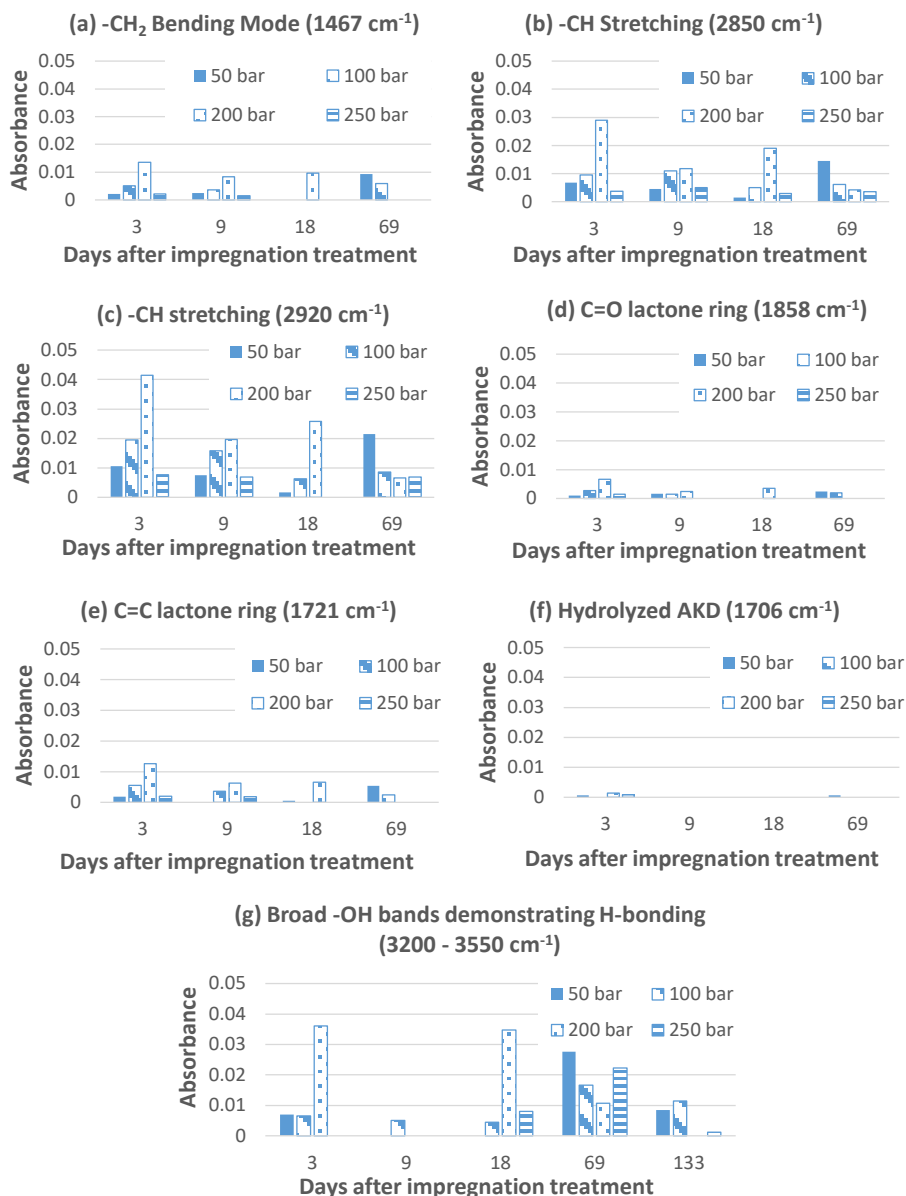
Figure 3.10: Absorbance vs time of various AKD wavenumbers at different impregnation pressures (scCO2 / AKD / heptane). (a) – (c) bending or stretching modes of alkane chains on AKD; (d) – (e) evidence of the AKD lactone ring showing C=O and C=C respectively; (f) lack of absorbance at the ketone peak; (g) broad bands of –OH stretching, potentially demonstrating the existence of hydrogen bonding.

3.3.3.4 Importance of the –OH broad-band peak

Absorbance bands were compared between 'AKD/cellulose' and 'only AKD' for the 50 and 100

bar data (**Figure 3.11**) in the region 2,700-3,600 cm^{-1}. The AKD proportion towards this band

height was between 35-40% of the AKD/cellulose peak and is therefore significant. This vibrational band is not a result of unreacted fatty acids, and AKD molecules do not contain any –OH groups. While there could potentially be some hydrolyzed AKD present from moisture interference after such a long time period, there was no evidence of ketone or carboxylic acid peaks which would additionally confirm this theory. The 'only AKD' traces were obtained by subtracting untreated cellulose from the combined AKD/cellulose trace, and if there was no hydrogen bonding between AKD and cellulose, then there should be no resulting intensity in this wavenumber region. The fact that there is a definite peak in this region indicates that the resulting 'only AKD' trace is actually a combination of AKD and hydrogen bonds between AKD and cellulose. Pure AKD wax FTIR traces do not contain any peaks whatsoever in this region [138]. The broad –OH band observed in the plain cellulose trace also shown in this Figure is a result of the many –OH groups on cellulose rings. Additionally, given the large degree of hydrogen bonding between cellulose chains, additional vibrations occur on the –OH groups which contribute to the broadening observed [193]. The FTIR trace of cellulose incorporating the –OH vibrations and those associated with hydrogen bonds, once subtracted from the AKD/cellulose trace, can only leave AKD and any additional hydrogen bonds between AKD and cellulose. Hence the AKD traces in Figure 11 also identify the presence of hydrogen bonding with the cellulose.
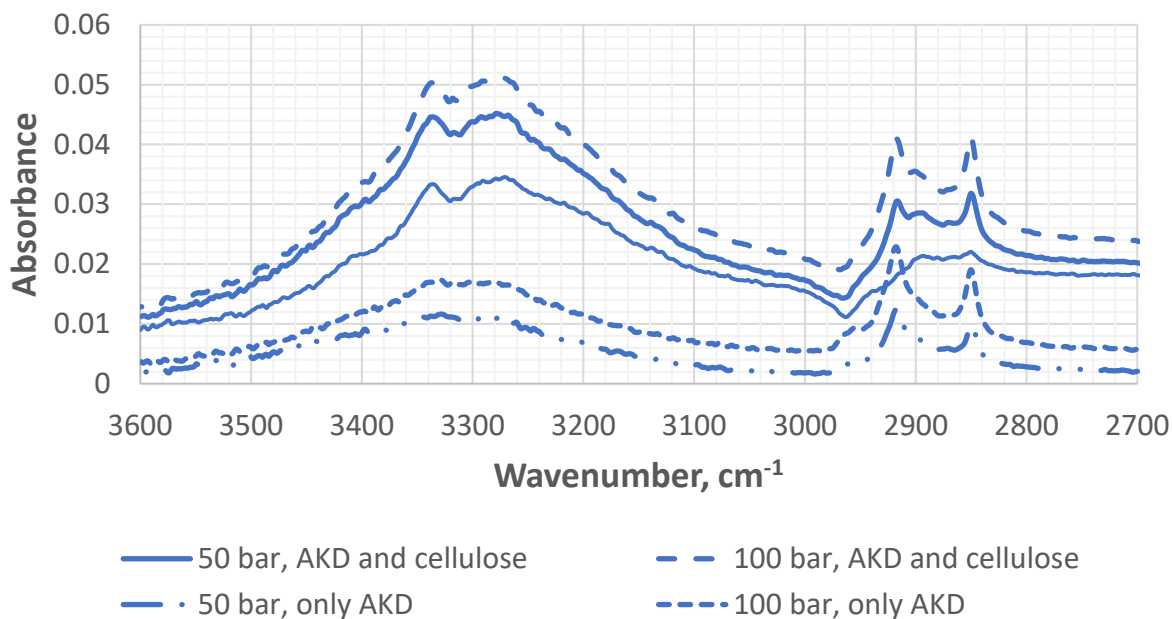
Figure 3.11: Broad band –OH stretching taken at 133 days, 50 and 100 bar impregnation pressures (scCO2 / AKD / heptane), showing contributions of 'AKD/cellulose'; 'only AKD'; and untreated cellulose.

A study by Gonjo, Futami, Morisawa, Wojkic and Ozaki [193] demonstrated that the influence of hydrogen bonding tended to shift the wavenumber of the peak to lower values (red-shift), accompanied by a reduction in peak intensity and broadening of the peak. A small reduction in wavenumber and intensity was observed for the 200 bar case in the lower of the two wavenumbers observed within this region, but this was not consistent across all process conditions studied. Figure 10(g) however definitely shows an overall trend downwards of the *average* intensity over all conditions investigated with time, particularly from 18 days onwards, also matching relatively constant CA results (see Figure 4(c)).

An important review by Nibbering, Dreyer, Kuhn, Bredenbeck, Hamm and Elsaesser [192]. reported studies on acetic acid dimer $(CH_3-COOH)_2$ using FTIR to investigate contributions of

hydrogen-bonding to the overall FTIR spectra in –OH stretching peaks [192]. This system was used as a reference system to determine the behavior of the intermolecular hydrogen bond on non-linear vibrational modes observed within FTIR. Three mechanisms of vibrational coupling from the hydrogen bonds were identified: anharmonic coupling of O—H stretching modes from high to low frequency; Fermi resonance of O—H stretching to fingerprint mode; and a combination of both. The acetic acid dimer broad spectrum between $2400 - 3400$ cm^{-1} was further examined to determine the influences of the three vibrational mechanisms from hydrogen bonding on these peaks. The combination of hydrogen-bonding vibrational modes best described the spectra observed, with its most intense peak occurring at 2920 cm^{-1}. The hydrogen bonds within the acetic acid dimer consist of two –C=O --- H–O–C arrangements. This combination of atoms and bonds can also be observed between an AKD molecule (C=O lactone ring) and an –OH group on a cellulose ring, connected via hydrogen bonding. It is fortuitous to note that the strongest contribution of hydrogen bonding in the acetic acid dimer occurred at 2920 cm^{-1}, a strong peak also observed in the current AKD-cellulose system, but usually assigned alkane -CH stretching [191]. In Figure 11, this peak has red-shifted to 2915 cm^{-1} for the 50 bar case, suggesting a steady decrease in position across the times investigated.

3.4 Conclusions

High-pressure CO_2 impregnation of cellulose substrates with AKD dissolved in n-heptane produced microporous, sticky, and near superhydrophobic substrates. The hydrophobic performance was not established within 24-hours but was significant 2-3 days after treatment. The average CA for samples impregnated at 200 bar and 21ºC was $140 \pm 5º$, while the CAH was $17 \pm$

5°. Optimal solubility of AKD/heptane in scCO$_2$ was found between 100-200 bar which was also consistent with literature data. The retentive force of adhesion developed between the droplet and fiber surfaces prepared at 200 and 250 bar at > 140 days was able to withstand more than 20 μL of droplet volume when tilted to 90°.

Analysis of the SEM micrographs showed a maximum reduction in pore size of about 14% when impregnated with AKD at 200 bar, corresponding to an increase in the CA, and potentially confirmed migration of AKD over the surface. The initial retention of AKD on the substrate together with the progressive fiber coverage with time lowered the surface energy as well as substantially increased the hydrophobicity of the impregnated surfaces.

The presence of characteristic AKD and cellulose peaks identified with FTIR provided vital information on the mechanistic pathways for sizing development. Only small intensities of ketone and ester groups were observed, indicating a lack of hydrolyzation of AKD and direct reaction with cellulose –OH groups respectively. While migration of AKD over the fiber surface was the main sizing mechanism, hydrogen bonding between the lactone ring (C=O) of AKD and –OH groups on the cellulose ring appears to be a method of attachment. This work represents some unique insights into the sticky hydrophobicity created on cellulose surfaces impregnated with AKD using high pressure techniques.

CHAPTER IV

HIGH PRESSURE IMPREGNATION AND ANNEALING OF CELLULOSE FIBERS WITH

FOOD-GRADE WAXES: HYDROPHOBIC AND MECHANIAL PROPERTES

INVESTIGATION

This chapter will be submitted for publication to the Journal of Applied Materials and Interfaces.

4.1 Abstract

U.S. Food and Drug Administration (FDA) recommend the use of edible coatings for food-based packaging applications. In this study, high-pressure carbon dioxide (200 bar and 22°C) was used to impregnate food-grade waxes (yellow beeswax and yellow carnauba wax) onto cellulose substrates. After the treated substrates were annealed at 80, 110, 140 and 165°C (mostly above the melting point of the waxes), a highly hydrophobic surface was formed, with a maximum CA being about 135° at 165 ^{o}C conditions. Significant increases in hydrophobic properties were observed between 110 and 165°C. The mechanical properties of the impregnated and annealed surfaces were investigated with dynamic mechanic analysis, and compared with untreated samples. The impregnation treatment improved the mechanical robustness of the substrates due to strengthening

of the inter- and intra-fiber bonding, but no observable additional improvement was found with the annealing. The method is novel and uses no toxic material or any substance classified as unsafe for direct food contact. Impregnation techniques offer an additional advantage for making ultrathin surfaces.

4.1 Introduction

Superhydrophobic surfaces can be fabricated using methods ranging from mere surface deposition [1] to complex processes such as plasma methods [2,25]. These methods aim at manipulating the surface chemistry and geometry of the substrates to which they are applied [41]. Many of these methods cannot be applied to cellulose-based materials (CBM) because of their hydrophilic nature as a result of many hydroxyl groups in their structure [1]. Typically, there are two factors that determine the wetting characteristics of a surface – surface roughness, and surface energy [29,41]. The existence of hierarchical structures has been found on most superhydrophobic surfaces [2]. The superhydrophobic surfaces found in nature on lotus leaves exhibit this hierarchical nano/micro structure which was said to be more dominant in the formation of its superhydrophobicity than surface energy [2,194]. Several studies have reported how to mimic the hierarchical nano/micro structure of lotus leaves on different surfaces [10,22]. Therefore, modification of a surface to achieve superhydrophobicity is accomplished by lowering the energy of a surface and/or enhancing its roughness [10]. Multiple treatments may be needed to achieve these properties [2]. These treatments are usually very expensive and often include an addition of fluoropolymers due to their low surface energy [2].

The use of edible waxes for food-based applications to replace organic and fluorine-derived compounds has been on the increase [44,175,195]. US. Food and Drug Administration controls (FDA) regulates the use of coatings in food-based products. Unfortunately, many sizing chemicals that are used in the fabrication of water-repellent packaging materials are not classified as food-compatible [44], but are acceptable provided they do not come into contact with the food itself. However, the use of food-compatible waxes either within the coating or as a coating alternative provides an added level of safety for the consumer, and potentially expands the food packaging industry to new areas of application. Because edibles waxes have higher surface energy than fluorocompounds, they may require further processing for efficient performance [44].

Wax coatings permitted for use in food-based applications, according to the FDA, are classified as 'edible coatings' [44,175], of which beeswax is one. Beeswax is one of the few food-grade waxes that is is being considered as alternative sizing agents for paper and packaging products [196,197]. It is chemically made up of long chain hydrocarbons, alcohols, free acids and esters, and is naturally superhydrophobic due to the presence of internal chain methylene units (more than 95%) in its structure [197,198]. Beeswax is primarily composed of palmitate, palmitoleate and oleate esters [199,200]. Therefore, the chemical structure of beeswax is represented by that of esters – an approximate chemical formula for beeswax is $C_{15}H_{31}COOC_{30}H_{61}$ [200]. In addition to water-repellent properties, it also possesses excellent antibacterial properties and offers some resistance to water vapor transmission [90]. Carnauba wax is another type of food-grade wax that is commonly used as fruit coating due its ability to extend shelf-life [201]. It has excellent moisture barrier properties and poses no threat to food items [202]. Carnauba wax contains mainly fatty esters (80-85%), free alcohols (10-15%), acids (3-6%) and hydrocarbons (1-3%) [203].

Most waxes used as sizing agents are made of different components. Upon heating, wax phases separate out at different temperatures – components with lower melting points flow out first [10]. During re-solidification, the polymorphic phase separation would likely lead to a formation of a new surface morphology and roughness profile. Curing of wax-coated paper substrates at certain temperatures often leads to improvement in their hydrophobic properties due to phase separation of the waxes upon applied thermal heat load [10]. Structural and morphological changes are also observed with other chemicals such as proteins [196,204,205] and silica films [194]. Thermal treatment of protein molecules causes them to unfold as they denature, exposing their sulphydryl and hydroxy groups, often leading to enhancement of surface hydrophobicity [196]. Surface hydrophobicity of silica films can be enhanced by an annealing treatment [194]. Specifically, trimethylchlorosilane (TMCS) was used as a silylating (silanizing) agent for surface chemical modification of silica films [194]. It was reported that the heat treatment improved the adherence and surface hydrophobicity of the silica films [194]. Similarly, thermal treatment of metal acetylacetonate (Fe-acetylacetonate and Cu-acetylacetonate) with methylmethoxy silane (MTMS) based coating can be used to enhance the surface hydrophobicity of silica films [194]. Additionally, the hydrophobicity of silica aerogels can be further enhanced by heating them to certain temperatures [206]. The surface modification of silica aerogels is attributed to the grafting of methyl groups during the curing process [206].

The technique of using high-solvating power of supercritical carbon dioxide ($scCO_2$) has been demonstrated to be very effective in creating superhydrophobicity on CBM [13,74]. Due to their liquid-like density; gas-like diffusivity; gas-approaching viscosity; high mass transfer and low surface tension, $scCO_2$ has enhanced capacity to insert and uniformly distribute wax components

onto the cellulose fiber surface [13,93]. The ultra-high solvating power of $scCO_2$ has been reported as an efficient and novel method of surface-sizing CBM [9].The two main methods that use $scCO_2$ are rapid expansion of supercritical solutions (RESS) [13] and impregnation techniques [14] – both studies focused on modifying cellulose fibers with alkyl ketene dimer (AKD).

In this study, the fabrication of highly hydrophobic surfaces was achieved by exploiting the solvating power of $scCO_2$ to uniformly distribute the food-grade waxes onto cellulose substrates before curing them at different temperatures for the enhancement of surface hydrophobicity. The hydrophobic performance and mechanical impact of the processes was assessed by conducting the following characterizations: (a) the surface energy behavior of impregnated/heat-treated cellulose; and (b) effects of the treatment on the mechanical robustness of the surfaces. Surface and interfacial properties of the substrates were investigated by CA studies. Dynamic and Thermal Mechanical Analysis (DMTA) provided vital information on the mechanical properties of the surfaces [207]. The goal of this study was to produce highly water-repellent surfaces on cellulose substrates with food-grade waxes via high pressure and annealing methods, and subsequently investigate their mechanical properties. The findings in this study will contribute to the on-going research efforts in using FDA-approved edible waxes for hydrophobic modification of food containers or packaging materials

4.3 Material and Methods

4.3.1 Materials

Yellow Beeswax (BW) (*#423*) and Yellow Carnauba wax (CW) were supplied by Koster Keunen with melting points of 63.5 ^{o}C and 83 ^{o}C, respectively. 10 g/L solutions of the wax mixture (1:1) were prepared from analytical grade *n*-heptane (99.5%, Sigma Aldrich), while individual wax solutions in heptane used a concentration of 10 g/L. Carbon dioxide (<50ppm moisture) supplied by Airgas USA, LLC was used as the carrier fluid to dissolve the waxes/heptane solutions, and heptane was the cosolvent. The cellulose substrate used for all the experiments was Whatman filter paper no.1 (Sigma Aldrich).

4.3.2 Methods

Supercritical impregnation of cellulose substrates was conducted at 22°C and 200 bar using methods and equipment built in-house, and described elsewhere [14].

Heat treatments of the impregnated surfaces were performed at 80, 110, 140 and 165°C for 4 hours each (and 24 hours in one case) and were carried out in an oven manufactured by Precision Scientific Inc. Division (Winchester, Virginia). The oven is rated 1300 Watts (120 volts and 11.3 AMP and with a frequency of 50/60 Hz) and is operable between 65 and 200 ^{o}C. The heat treatment process was begun immediately after the cellulose substrates were impregnated.

Sessile drop CA experiments enabled the determination of static and dynamic CA, using a Biolin Scientific OneAttension Theta CA Analyser, coupled with a single-liquid automatic dispenser, inbuilt NAVITAR (model 520931) and OneAttension software. The droplet volume was 10 μL for all CA measurements, while drop rate was ket at 1 μL/s. Deionised water was used as the working fluid. All CA experiments were performed within 4hr, 24 hr and 3 days after heat treatment or impregnation for non-annealed samples. Both CA measurements and annealing treatments were performed in a periodic manner to investigate the sizing mechanistic development with time.

Thermal and mechanical properties of both treated and untreated samples were determined by measuring storage moduli, loss moduli and tan delta using a Q800 Dynamic Mechanical Analyzer, DMA (TA Instruments, DE, USA). A frequency of 1 Hz was used at a temperature range of 20–150°C with a heating rate of 5°C/min. The film tension mode was used. The dimensions of the samples were 7.35–19.60 mm long, 4.06–6.06 mm wide and 0.15–0.175 mm thick after cutting the specimens. The time delay between sample preparation (impregnation and heat treatment) and DMA testing was not formally controlled but all tests were conducted within 2-3 days after heat treatment or impregnation for non-annealed samples.

4.4 Results and Discussion

4.4.1 Surface Energy of Impregnated and Annealed Cellulose Substrates

Hydrophobic development on a surface is linked to an increase in surface roughness and/or substantial decrease in surface energy [22]. The impregnation of food-grade waxes over the cellulose fibers lowered their surface energy and increased the surface roughness. However, additional annealing treatment was used to augment the surface profile of the substrates which further improved their hydrophobicity due to phase separation of the wax components. CA measurements of the impregnated surfaces with and without heat treatments were taken to quantify the hydrophobic properties at the surface.

4.4.1.1 Surface energy of impregnated substrates prior to heat treatment

Fig. 4.1 shows the CA behavior of cellulose substrates impregnated with BW-only, CW-only and their mixture, without heat treatment, taken immediately after the impregnation treatment. All wax samples exhibited a higher CA compared with untreated substrates. However, these measurements were still in the hydrophilic range (CA < 90º) and the substrates could not offer sufficient resistance to water droplet penetration with time. Wax-mixture samples had slower rates of droplet penetration than individual waxes. The behavior of the droplets on impregnated surfaces without additional heat treatment revealed inherently lower surface energy than the untreated substrate. Therefore, the surface energy of the treated substrates was mainly indicative of the chemical properties of the waxes. Other studies that used these same waxes to impart water repellency on a surface had to augment the hydrophobic performance with heat treatment before the surfaces

turned superhydrophobic [10,22]. When pure individual waxes – rather than the BW-CW combination – were melted and hand-coated on the substrates forming a continuous layer, the surfaces were almost superhydrophobic (results not shown) without an additional heat treatment. The impregnation technique, however, has the unique property of uniformly coating and distributing much smaller quantities of waxes over the cellulose fibers making up the substrates [9,14].
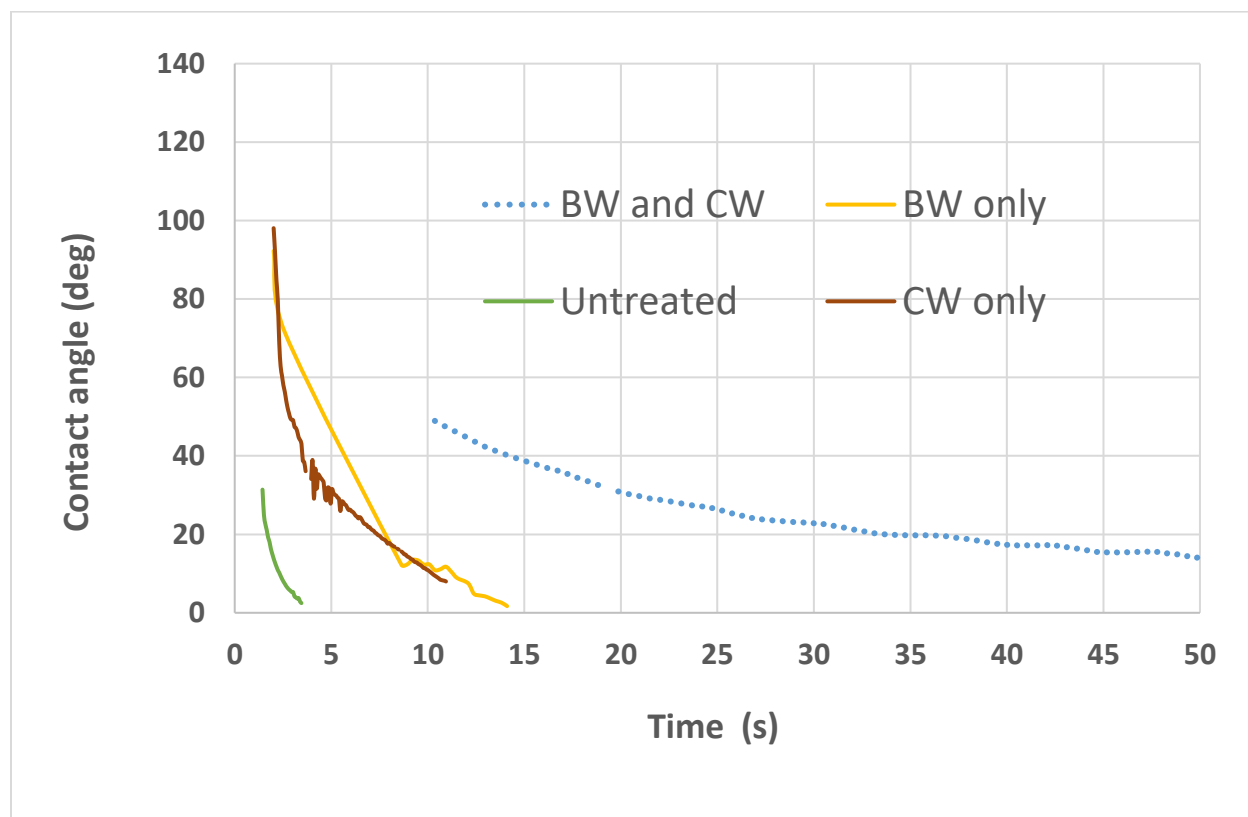
Figure 4.1: Dynamic CA analysis without annealing after impregnation (scCO2 / heptane, 200 bar and 22 OC) of the waxes (BW only, CW only, and BW and CW) as compared with untreated substrate.

4.4.1.2 Influence of heat on the hydrophobic performance

After impregnation of the wax mixture (BW-CW) at 200 bar and 22 $^{\circ}$C, the treated substrates were subject to additional heat treatments at 80, 110, 140 and 165 $^{\circ}$C for 4 hours. **Fig. 4.2** shows that annealing the "untreated substrate" at 140 $^{\circ}$C does not improve its hydrophobic properties, as expected – and any changes to the surfaces with heat treatment were due to the formation of microstructure caused by the phase separation process of the waxes. In **Fig. 4.2**, it is shown that annealing of impregnated substrates with the wax mixture substantially improved their hydrophobic performance, resulting in stable CA of approximately 95° for the sample annealed at 80°C; 129° at 110°C; 114° at 140°C; and 133° at 165°C. Each of these CA has an error of $\pm$ 5° as determined from previous studies. Hydrophobic properties of the samples annealed at higher temperatures than their melting point range of the waxes (63.5 and 83°C) further improved after annealing due to characteristic phase separation of individual waxes.
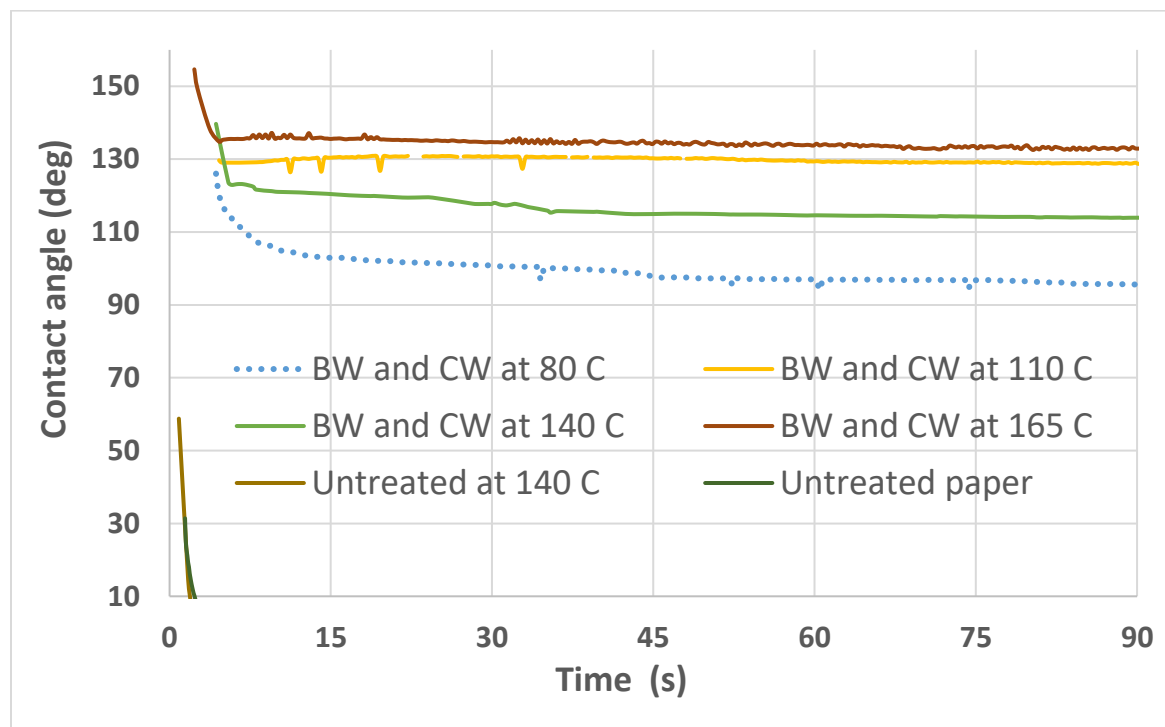
Figure 4.2: Dynamic CA analysis of impregnated BW-CW at 200 bar and 22 ^oC) after annealing at 80, 105, 140 and 165 ^oC as compared with untreated substrates (without annealing and annealed at 140 ^oC.

In a study by Zhang, Lu, Qian and Xiao [10], 10 g of molten wax mixture (carnauba and beeswax) in 40 mL cetytrimethyl ammonium bromide (CTAB) solution was coated on an A4 copy paper applied via a roll-coating method. After drying, the coated paper was then cured at different temperatures for 12 hours to create a new morphological structure of the wax coating layer during the phase separation and reorganization of the wax particles. Surfaces coated with the wax mixtures turned superhydrophobic after annealing at about 60-70 ^oC for 12 hours. The wax mixture (1:1) annealed at 60 ^oC had the highest CA of 167.7 $\pm$ 3.6^o. The amount of wax coated on the paper was 10 g/m^2. It was not stated whether the substrates were cured immediately after drying or not. In the current study, samples cured at 80 ^oC three days after the impregnation treatment were more hydrophobic that those cured immediately (see **Fig. 4.3**), with the best condition

providing a CA of approximately 118°. The time delay of three days allowed an increase in CA of 23°. Although these figures are much less than that reported by Zhang. Et. al. [10], the amount of wax impregnated on the substrate was five times less, at approximately 2 g/m^2.

The higher CAs reported by Zhang et. al. [10] could be due to the formation and development of self-assembled monolayers (SAMs) of wax molecules via self-organization of long chain hydrocarbons of the wax onto the surfaces of the substrates. This is particularly the case with beeswax, which are esters with two long-chain hydrocarbons [208,209]. Consequently, the resultant effect of the terminal alkyl groups (tail ends) facing up while the ester groups attached to the surface caused the development of a highly hydrophobic surface. In this present study, however, the much lower quantities used and the lower CA obtain suggest that some of the terminal alkyl groups may have still been pointing laterally (parallel to the substrate surface). Some days after impregnation treatment, an increase in CA was observed, and it is possible that with time, more wax molecules adopted a stand-up orientation. According Bhushan [209], upwards-pointing

terminal alkyl groups are the backbone of SAM formation – and the attachment of more of these

terminal alkyl chains enhances the hydrophobicity of a surface.
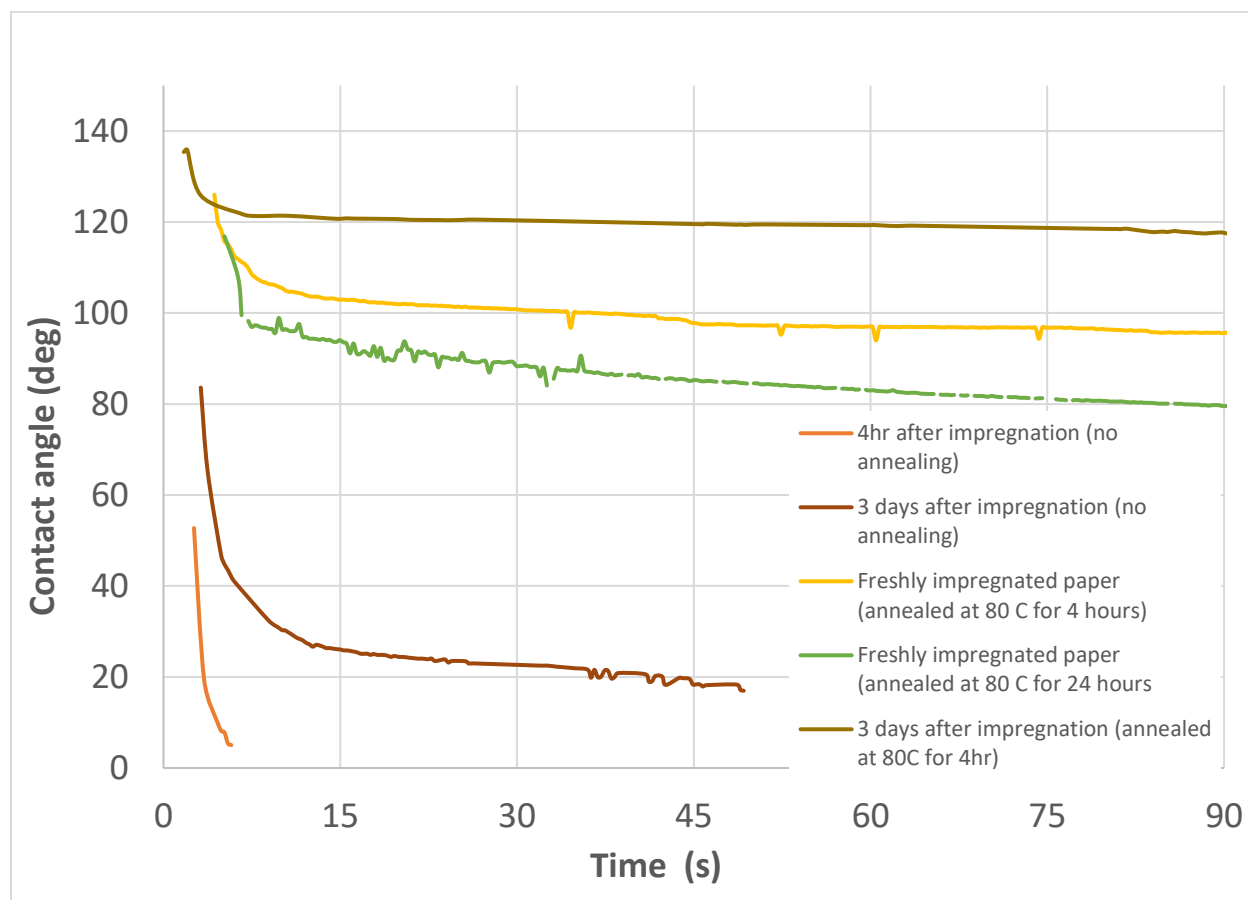
Figure 4.3: Dynamic CA of paper substrates treated with the following conditions; 4hr after impregnation without annealing; 3 days after impregnation without annealing; freshly impregnated paper (annealed at 80 °C for 24 hours); 3 days after impregnation (annealed at 80 °C for 4 hours). All impregnated substrates were done at (scCO₂ / BW-CW / heptane, 200 bar and 22 °C).

The samples annealed at 80 and 110 °C as shown in **Fig. 4.2** had significantly higher

hydrophobicity than impregnated-only sample. The trend of the sample annealed 80 °C was stable

but indicative of incomplete hydrophobic development.

The hydrophobic performance of samples annealed at higher temperatures can be described as "stable and fully developed". The sample annealed at 165 °C produced the highest and most stable hydrophobic surface with average CA of 134° for the entire analysis time. More repetitions of CA measurements are needed confirm the trends of the hydrophobic performance in **Fig.4.2**, especially for 140 and 165 °C conditions.

4.4.1.3 Droplet behavior

Untreated "Whatman filter paper no. 1" was completely wetted within 2 seconds, and the droplet broke away from the syringe with ease. For the substrate impregnated with the wax mixture (without heat treatment), its droplet behavior was similar to that of untreated substrates but took a longer time to be completely wetted. **Fig. 4.4** shows the droplet behavior of the untreated substrate as compared with those annealed at elevated temperatures after impregnation treatment of the wax mixture. The droplet behaviors of samples annealed at 80 and 110 °C follow similar trends to each other and were maintained at a steady CA of about 100° and 117°, respectively, for more than 90 seconds. At 140 °C, far away from the melting temperature range [10] and not too close to the boiling temperature range of BW [204], the effect of phase separation(s) and polymorphic phase transitions of the wax mixture appeared to be more significant in this region. The droplet maintained a stable and high CA beyond the duration of the experiment. Repeats of CA measurements will be done to confirm the trends of the droplet behavior in **Fig. 4.4**, specifically for 140 and 165 °C conditions.
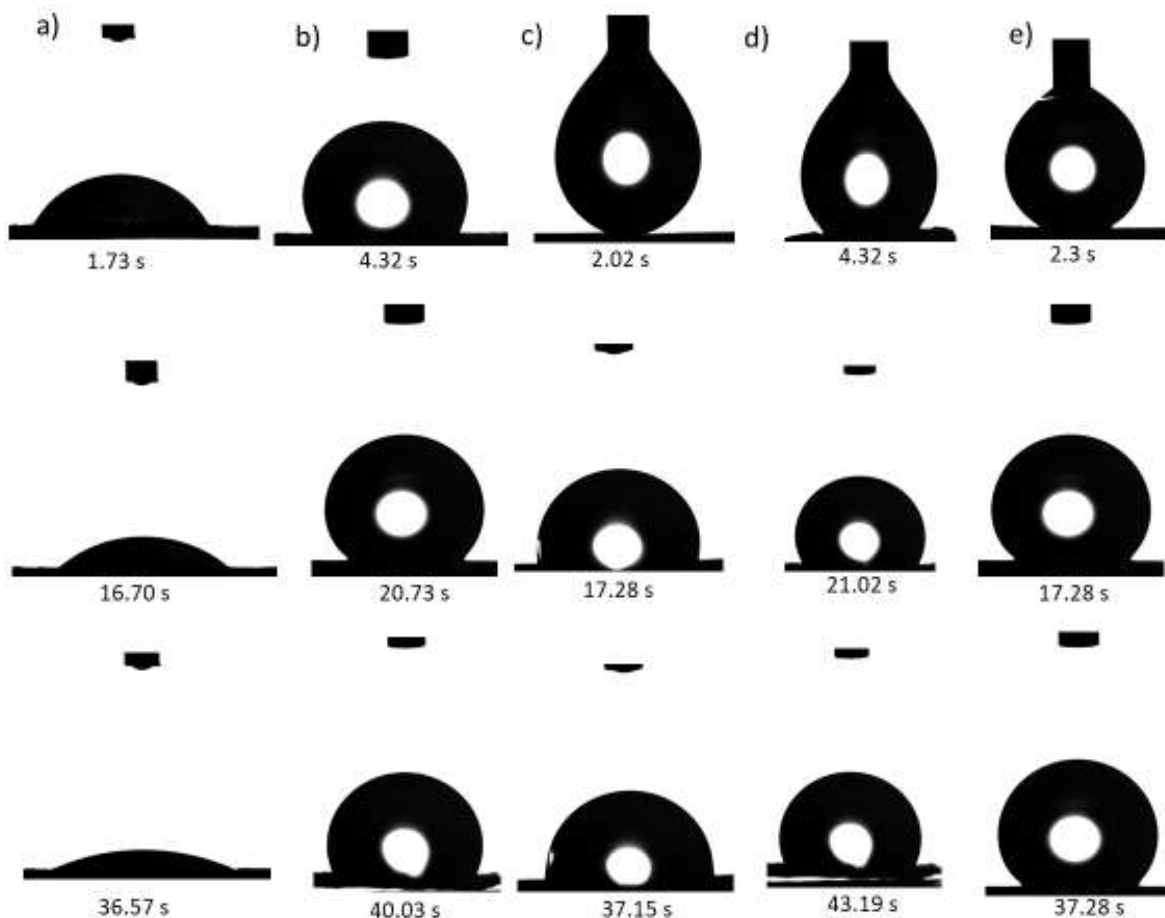
Figure 4.4: Water droplet behavior on surfaces annealed at different temperatures after impregnation treatment (scCO$_2$ / BW-CW/ heptane) at 200 bar and 22°C; (a) no heat treatment; (b) 80 ^{o}C ; c) 105 ^{o}C ; d) 140 ^{o}C and (e) 165 ^{o}C.

In this current study, the CA measurements showed that the surfaces were not superhydrophobic, but the force of adhesion was strong enough to support a 10 μL droplet tilted to any direction. The phenomenon whereby droplets stick to the surfaces of substrates was extensively studied elsewhere, and is known as sticky hydrophobicity [14]. Both the impregnation and annealing treatments altered the surface energy.

4.4.2 Thermal and Mechanical Properties of the Treated Surfaces

The hydrophobic properties of most waxes are mainly due their richness in esters, long-chain fatty acids and long-chain alkanes [10]. The components of waxes respond to heat differently. As their thermal properties change upon heating, their mechanical properties are also affected. In addition, it is likely that the high-pressure process could alter the mechanical properties. A connection has been found to exist between mechanical properties and how droplets penetrate CBM either by absorption on the surface, or by the penetration of the lumen [5,6]. Specifically, Kassem et. al. [5], reported that cellulose papers with low-surface-energy polymer coatings can significantly improve their breaking length and mechanical robustness. In the current study, the storage modulus, loss modulus and tan delta of untreated, wax-impregnated and annealed impregnated substrates were determined. It should be noted that the DMA data are preliminary results, and further measurements and tests are needed to confirm the trends of the viscoelastic behavior of the substrates.

4.4.2.1 Storage modulus

Storage modulus is a measure of the stiffness of a material [210] – and is often referred to as the tendency of a material to store up the energy applied to it for a later use. **Fig. 4.5** compares the changes in the storage modulus of untreated, impregnated-only, and cured-impregnated substrates. The high-pressure wax impregnation treatment increased the storage modulus of the untreated substrate by almost five times in the lower temperature test region (approximately 35 – 45 ^{o}C) and hence agrees with Kassem et.al. [27] findings on the improvement of mechanical robustness of cellulose papers. Subjecting the impregnated-only substrate to a curing temperature of 80°C for 4

hours further altered the mechanical properties. A gradual increase in storage modulus as curing temperature increases is a resultant effect of a tighter network structure and higher stiffness as Rashid, Leman, Jawaid, Ghazali and Ishak [211] pointed out. During the annealing process (phase separation), the rearrangement and spreading of the waxes to more porous areas could have caused the gradual decrease in the storage modulus. The difference between the storage modulus of 140 $^\circ$C sample and those of other treated samples was only significant in the lower temperature region – for the rest of the region, the variation was within experimental errors. The excellent mechanical performance of hydrophobic coatings on CBM is largely attributed to their inherent structural features (suitable microscale roughness) [49]. Torun et. al. [49], in their study on "robust superhydrophobicity on paper", reported that cellulose papers outperformed glass in resistance to mechanical wear, though both were treated with the same coating formulation.

Figure 4.5: Storage modulus of untreated paper, impregnated-only (scCO$_2$ / BW-CW / heptane, 200 bar and 22 ^{O}C) paper (without annealing) and impregnated (scCO$_2$ / BW-CW / heptane, 200 bar and 22 ^{O}C) paper annealed at 80 and 140 ^{o}C.

4.4.2.3 Loss modulus

The viscous response of a material to mechanical force imposed on it is termed "loss modulus" [210,212]. The loss modulus arises from internal friction and is often used to quantify the energy loss under stress or deformation (energy dissipated as heat) [207,210,212]]. **Fig. 4.6** illustrates how loss modulus of untreated, impregnated and annealed paper substrates change with temperature. As it can be clearly seen, the untreated substrate exhibited the lowest modulus (about 15 MPa for the entire regions). The increase in loss moduli was more significant at lower temperatures for the impregnated and annealed samples. The loss modulus of the sample annealed at 80 ^{o}C was the

highest across the entire temperature range investigated with an average error of about ± 5 MPa. As a result, there would be an increase in interlocking bonding between the wax and the fiber. The phase separation in the melting range (for the sample annealed at 80 $^{\circ}$C) could trigger the removal and migration of wax molecules from on point to another – resulting in large variation in loss modulus between lower and higher temperature regions compared with other annealing conditions. All impregnated and annealed substrates showed relatively higher values of loss modulus as compared with untreated substrates which suggests strong interfacial bonding to the substrate according to Rashid et. al. [211].
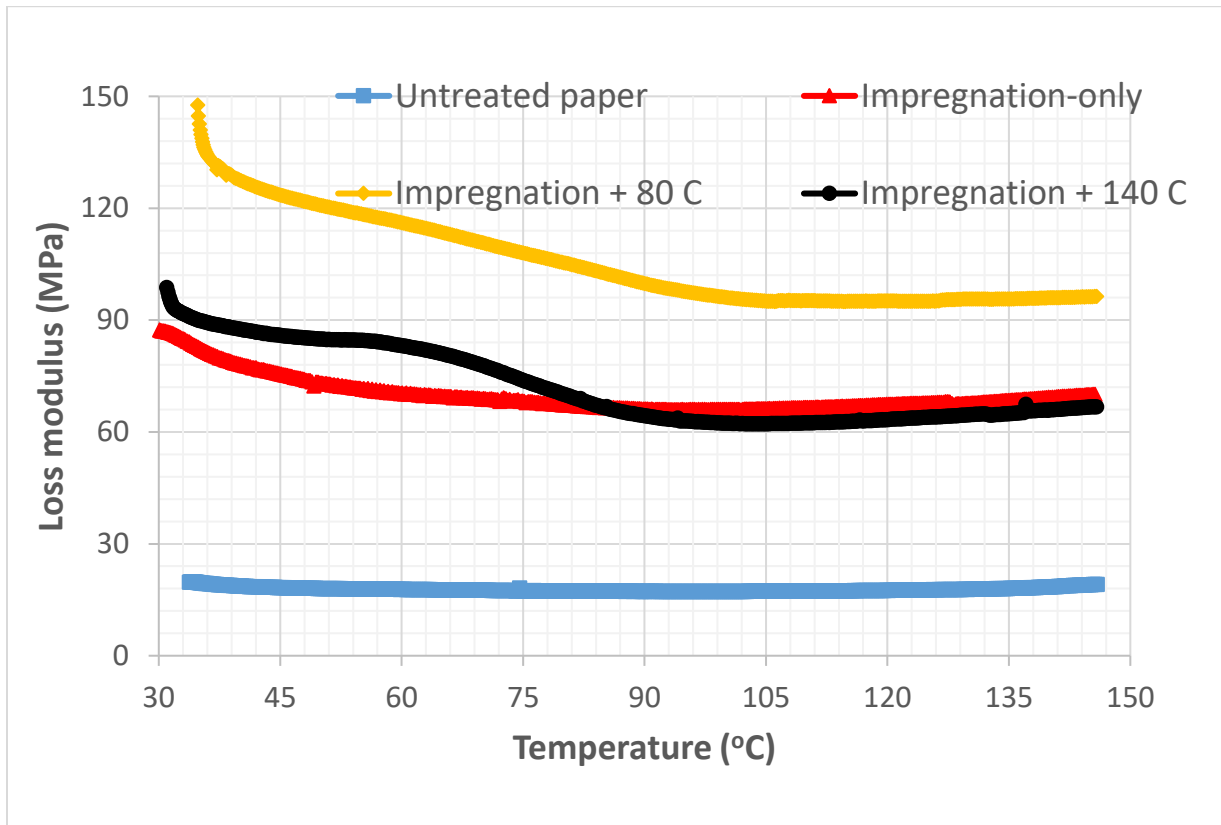
Figure 4.6: Loss modulus of untreated paper, impregnated-only (scCO₂ / BW-CW / heptane, 200 bar and 22 ^{O}C) paper (without annealing) and impregnated (scCO₂ / BW-CW / heptane, 200 bar and 22 ^{O}C) paper annealed at 80 and 140 ^{o}C.

4.4.2.3 Damping Factor

The resultant effect of storage and loss modulus on a material in the "damping factor or tan delta". Tan delta is a dimensionless number (the ratio of loss to storage modulus). The region or point where tan delta approaches a maximum value indicates the glass transition temperature [207]. Glass transition temperature is the temperature range where a material begins to change from a "glassy" or hard state to a more easily pliable (softer) or "rubbery" state [210]. At the glass transition temperature, there is a possibility of a reversible transition from a hard-brittle state to a viscous (rubbery-elastic) state. The tan delta plot in **Fig. 4.5(c)** does not show a maximum value, indicating the conditions were outside the transition region.

In a study by Destro, Gramaccioli and Simonetta [213] on the investigation of thermal transitions in cellulose, three transition zones exist which are -30 ^{o}C; 20–25 ^{o}C and 200 –250 ^{o}C. The existence of multiple glass transition temperatures in nano cellulose composites has been reported elsewhere [214]. Rashid et. al. [211] describes a number of factors that influence the variation in tan delta, which include fiber breakage, fiber-matrix interlocking, matrix cracking, presence of interphase zone, and frictional resistance. In addition, tan delta can be used to determine the curing behavior of composites [211].

The tan delta plot shows no notable change between treated and untreated substrates (all within same experimental error) – all three curves are virtually on top of each other, except the sample annealed at 80 ^{o}C. Materials with lower damping factors have better load-bearing properties [211]. Therefore, all the treated samples will have similar mechanical durability with an average error of

about ± 0.01. Similarly, Saba et. al. [27] attributed reduction in damping factors to an increase in the fiber-matrix interface bonding due to decreased mobility of molecular chains at the interface. The sample annealed at 80 ºC (closest to the melting range of the wax mixture) had the lowest wax-fiber bonding because of its highest damping factor, and hence, would have lowest load-bearing capacity. This sample also showed the least hydrophobic development.
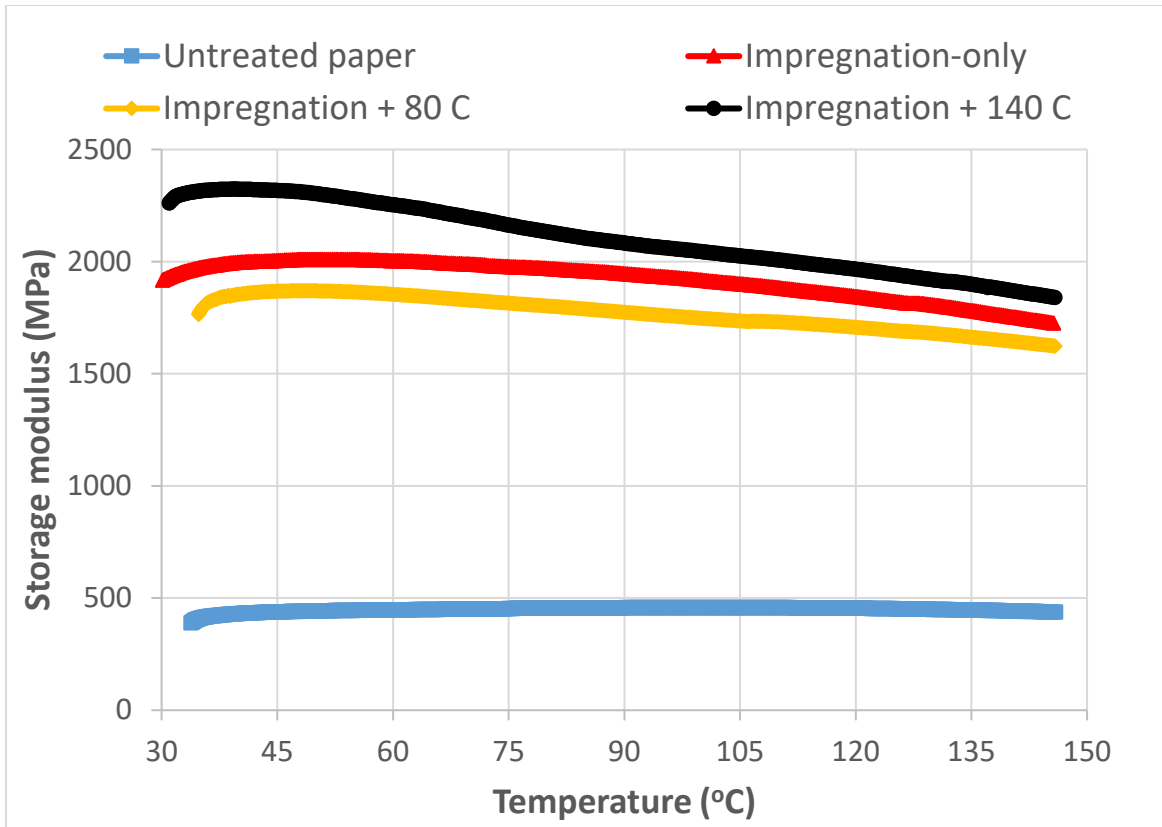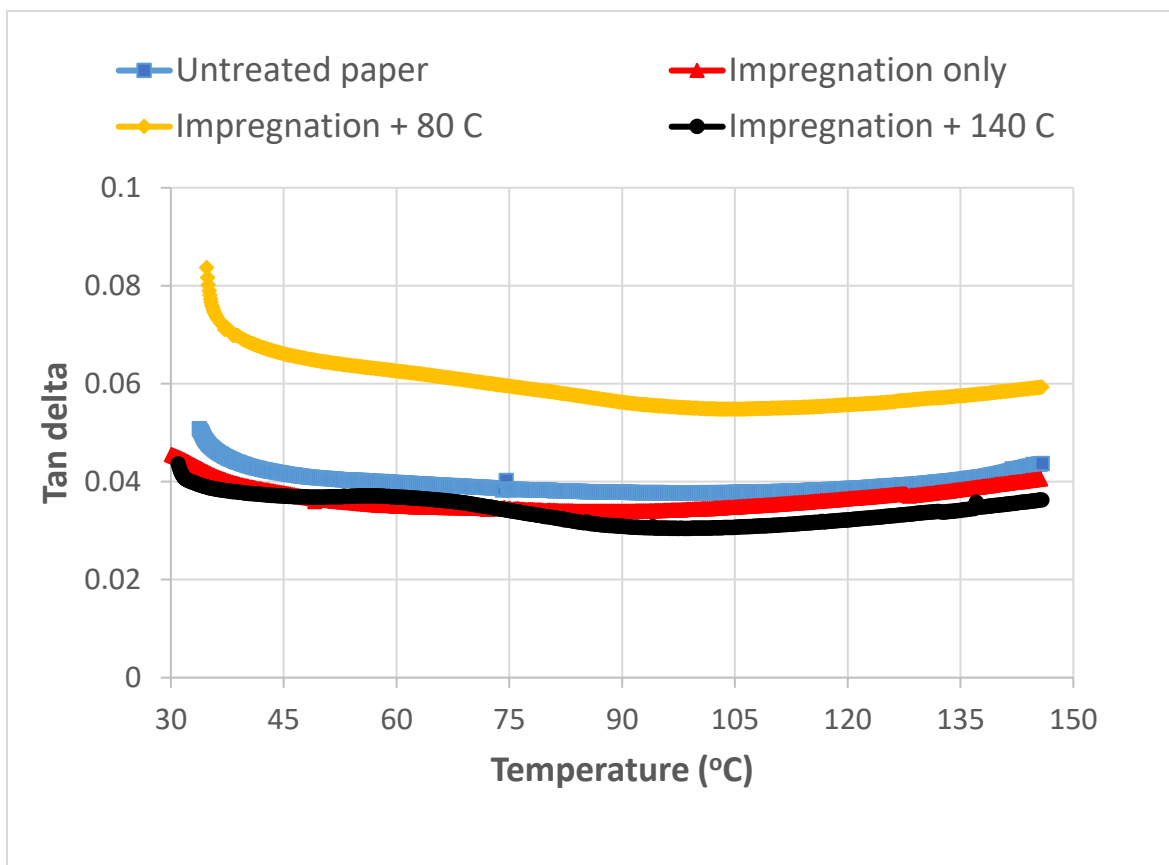

Figure 4.7: Tan delta plot of untreated paper, impregnated-only (scCO$_2$ / BW-CW / heptane, 200 bar and 22 ^{O}C) paper (without annealing) and impregnated (scCO$_2$ / BW-CW / heptane, 200 bar and 22 ^{O}C) paper annealed at 80 and 140 ^{O}C.

4.5 Conclusions

In this work, a highly hydrophobic surface was created by impregnation of edible waxes (yellow beeswax and yellow carnauba wax) on paper surfaces via $scCO_2$, followed by a heat treatment to augment and speed up the rate of hydrophobic development. The melting and recrystallization of the wax components upon heating and cooling, respectively, caused formation of hierarchical microstructures which further improved the hydrophobicity of the surface. CA measurements taken immediately and three days after treatments showed that the sizing development was progressive. For samples annealed immediately after the impregnation treatment, higher hydrophobicity was attained at higher temperatures (140 and 165 ^{o}C). Lower temperature annealing at 80 ^{o}C (within the melting range of the waxes) applied to samples three days after impregnation produced an average CA of 130°. Two patterns of hydrophobic development were observed. First, freshly impregnated samples needed to be annealed at higher temperatures to produce a more stable and higher hydrophobicity. Secondly, delayed annealing from impregnation treatment enabled higher hydrophobicity at lower temperatures (just around the melting range of the waxes).

DMA properties of untreated, impregnated, annealed-impregnated substrates were assessed in terms of variation in storage modulus, loss modulus and tan delta with temperature. The high storage modulus values indicated higher stiffness of the treated substrates compared with plain cellulose paper. Also, they offered better resistance to mechanical wear. The loss moduli of the treated substrates were much higher than untreated substrates, suggesting strong bonding strength between the substrates and waxes. All annealed-impregnated substrates exhibited high-water

repellency as well as showing very high durability. The tan delta plot shows that all substrates are more elastic than viscous. Moreover, further investigation is needed to establish the exact relation between hydrophobicity, and mechanical properties, although preliminary data suggests that hydrophobic development may be the linked to the mechanical durability.

CHAPTER V

CONCLUSIONS AND RECOMMENDATIONS

5.1 General conclusions

The goal of this study was to develop highly water-repellent surfaces on cellulose substrates using supercritical impregnation methods, for food packaging applications. From the goal of this study, three objectives were clearly defined that formed the bedrock of the findings. Therefore, from each objective, a set of conclusions were drawn. The main conclusions from all findings are given below under each objective:

The first objective was to "Thermodynamically model the solubility of AKD solute in $scCO_2$ to help identify optimal conditions for impregnation". The model was used to predict unavailable experimental data of AKD over a wide range of pressures and temperatures.

- The Peng-Robinson EOS provided reasonably good solubility estimates of the AKD-$scCO_2$ system as compared with experimental data, especially at higher pressures and for all temperatures – typically in the regions where high-pressure hydrophobization method is carried out. Since dissolution of AKD in $scCO_2$ is usually performed at higher pressures,

the model will be very useful to provide reasonable estimates of the solubilities at these conditions.

- Solubilities were poorly predicted near the critical point (a limitation well known with EOS method).

- Different group contribution estimation methods (GCEM) produced different values of the physical constants, and hence the accuracy of the model hinges on the type and/or combination of GCEM used. Experimental determination of some of these constants will improve the predictive capacity of the model.

The second objective was to "Assess the hydrophobic performance of these solutes (AKD and food-grade waxes) when impregnated into cellulose substrates". This study determined the most appropriate solutes for creating highly water-repellent surfaces, and the conditions under which these were obtained (includes supercritical conditions as well as annealing in some cases).

- Impregnation treatment with AKD sufficiently modified the surface energy and surface roughness of untreated substrates. The average CA for AKD samples impregnated at 200 bar and 21°C was $140 \pm 5^{\circ}$, while the CAH was $17 \pm 5^{\circ}$. Nevertheless, for AKD, irrespective of the pressures investigated (from 50 to 250 bar), the hydrophobic development was not immediate but fully developed within 2 weeks after impregnation treatment.

- Annealing treatment further promoted the hydrophobic performance of food-grade-impregnated paper either by increasing the rate of hydrophobic development and/or promoting the hierarchical surface roughness, especially for food-grade waxes that did not become sufficiently hydrophobic after the impregnation treatment.

The third objective was to "Examine the surface and interfacial energies of various impregnated solutes (AKD, carnauba wax, natural vegetable wax, paraffin wax, beeswax, bees-milk) into cellulose substrates, and their resulting behavior / interactions with water droplets applied to the surface". This examination revealed some interesting surface and interfacial energy behavior; the mechanistic pathways of the sizing; and the surface morphology, together with the uniform distribution of the sizing chemicals over the fibers. Mechanical durability of some food-grade wax-treated substrates was also measured to gain an understanding of the mechanical behavior of these substrates.

- The measured CA indicated near-superhydrophobic conditions, and the CAH influenced droplets being glued to the surface like that of water droplets on rose petals. High-pressure impregnation with the waxes dissolved in n-heptane produced highly hydrophobic substrates. In some cases (especially for AKD), the droplets were sticking to the substrates, and were able to withstand more than more than 20 μL of droplet volume tilted to any direction. This means that the retentive force of adhesion was greater than the lateral force of adhesion.
- SEM micrographs showed a reduction in pore size with time as the hydrophobicity developed, and this increase potentially confirmed migration of the waxes, especially AKD

over the surface. Although some pores reduced in size, sufficient porosity was maintained which contributed to surface roughness and high contact angles.

- Migration of AKD over the fiber surface was the primary sizing mechanism. However, the migration was matched by an increase in hydrogen bonding between the lactone ring (C=O) of AKD and –OH groups on the cellulose rings, believed to be a possible means of attachment. This attachment, in turn, rendered the hydrophobic tails of AKD upward to promote hydrophobicity.

- The melting and recrystallization of the food wax components upon heating and cooling, respectively, caused formation of hierarchical micro structures which further improved the hydrophobicity of the surface.

- DMTA properties of treated, impregnated, and annealed impregnated substrates were assessed in terms of variation of storage modulus, loss modulus and tan delta with temperature. The high storage modulus values indicated higher stiffness of the treated substrates compared with plain cellulose paper. Also, they would offer better resistance to mechanical wear. The loss moduli of the treated substrates were much higher than untreated substrates – suggesting good bonding strength between the substrates and waxes.

5.2 Recommendations for Future Work

5.2.1   Future work: AKD

- Subcritical hydrophobization (pressure ranges from 10-60 bar and all at 22 ºC) of cellulose fiber for packaging applications via CO_2 by impregnation of alkyl ketene dimer (AKD) and

investigation of its sizing development." The hydrophobic performance will be assisted by annealing treatment. Characterization techniques: FTIR, CA analysis and SEM with ImagePro.

- Development of sticky hydrophobicity cellulose fiber with supercritical impregnation of alkyl ketene dimer (AKD): investigation of parameters and factors. The development of "sticky" hydrophobicity will be monitored with time. Characterization techniques: CA measurements, CA hysteresis, retentive and lateral adhesive forces. Heat treatment may be investigated whether it affects the development or not. Factors and parameters to consider pressures, impregnation time and concentration.

5.2.3   Future work: food-grade waxes

- Supercritical impregnation of cellulose fibers with vegetable wax, and enhancement of its surface hydrophobicity with annealing treatment: hydrophobic development, and study of its sizing mechanism. Characterization techniques: FTIR, DMTA CA analysis and SEM with ImagePro.

- High-pressure Impregnation and Annealing of Cellulose Fibers with Food-grade Waxes: Hydrophobic and Mechanical properties. Characterization techniques: FTIR, DMTA, CA analysis and SEM with ImagePro. (To be submitted for publication).

5.2.3   Future work: thermodynamic modeling

- AKD-CO_2 thermodynamic solubility, modeling solubility in the vicinity of the critical point using UNIFAC/UNIQUAC group contribution methods. The modeling results will be compared with experimental data and a non-analytical model.

- Phase behavior of food-grade waxes dissolved in supercritical carbon dioxide in the presence of heptane as cosolvent. The study will involve two parts. Since most interaction parameters of the ternary system are not yet available in the literature, the first is the experimental investigation of solubility of binary pairs (i.e. food-grade wax/heptane), and then use an appropriate equation of state to the thermodynamic solubility modeling.

5.2.4   Future work: multifunctional surface and other studies

- Investigation of mechanical properties of hydrophobic surfaces (AKD/food-grade waxes) made from high-pressure impregnation methods. It is becoming increasingly important for packaging materials to be resilient and durable. Therefore, the viability of hydrophobization techniques need be examined not only in terms of hydrophobic performance but also assessing their mechanical robustness after the treatments.

- Fabrication of multifunctional surfaces via supercritical impregnation and thermal barrier coatings: hydrophobic and mechanical properties. The individual performance of the following additives with excellent thermal barrier properties (silica aerogel, cellulose nanocrystals, nano titanium oxide and nanoclay) together with impregnation of AKD in $scCO_2$ will be explored. Characterization techniques: thermal barrier tests, FTIR, DMTA, CA analysis and SEM with ImagePro.

- A review study of some characterization techniques for superhydrophobic coatings on cellulose-based substrates. Due to chemical, physical and mechanical properties of cellulose-based substrates, some of the hydrophobization characterization techniques cannot be used. Some applicable hydrophobic testing techniques for cellulose-based substrates will be studied together with their output data and interpretation.

LIST OF REFRENCES

LIST OF REFRENCES

[1] H. Ogihara, J. Xie, J. Okagaki, T. Saji, Simple method for preparing superhydrophobic paper: Spray-deposited hydrophobic silica nanoparticle coatings exhibit high water-repellency and transparency, Langmuir. 28 (2012) 4605–4608. doi:10.1021/la204492q.

[2] H. Teisala, M. Tuominen, J. Kuusipalo, Superhydrophobic Coatings on Cellulose-Based Materials: Fabrication, Properties, and Applications, Advanced Materials Interfaces. 1 (2014) 1–20. doi:10.1002/admi.201300026.

[3] G. Barati Darband, M. Aliofkhazraei, S. Khorsand, S. Sokhanvar, A. Kaboli, Science and Engineering of Superhydrophobic Surfaces: Review of Corrosion Resistance, Chemical and Mechanical Stability, Arabian Journal of Chemistry. (2018). doi:10.1016/j.arabjc.2018.01.013.

[4] X. Wang, X. Hao, L. Ren, T. Qiang, S. Zhang, com Study of the Preparation, Characterization, and Sizing Performance of Modified Collagen Surface Sizing Agent, 9 (2014) 1255–1266. doi:10.4028/www.scientific.net/AMM.271-272.367.

[5] N. Kassem, A.M.A. Nada, Mechanical properties of paper sheets treated with different polymers, Pigment & Resin Technology. 38 (2009) 91–95. doi:10.1108/03699420910940572.

[6] G. Chen, P. Zhu, Y. Kuang, Y. Liu, D. Lin, C. Peng, Z. Wen, Z. Fang, Durable superhydrophobic paper enabled by surface sizing of starch-based composite films, Applied Surface Science. 409 (2017) 45–51. doi:10.1016/j.apsusc.2017.02.201

[7]   J.H. Han, G.H. Seo, I.M. Park, G.N. Kim, D.S. Lee, Physical and mechanical properties of pea starch edible films containing beeswax emulsions, Journal of Food Science. 71 (2006) 290–296. doi:10.1111/j.1750-3841.2006.00088.x.

[8]   T. Rutter, B. Hutton-Prager, Investigation of hydrophobic coatings on cellulose-fiber substrates with in-situ polymerization of silane/siloxane mixtures, International Journal of Adhesion and Adhesives. 86 (2018) 13–21. doi:10.1016/j.ijadhadh.2018.07.008.

[9]   B.H. Hutton, I.H. Parker, A surface study of cellulose fibres impregnated with alkyl ketene dimers via subcritical and supercritical carbon dioxide, Colloids and Surfaces A: Physicochemical and Engineering Aspects. 334 (2009) 59–65. doi:10.1016/j.colsurfa.2008.10.001.

[10]   W. Zhang, P. Lu, L. Qian, H. Xiao, Fabrication of superhydrophobic paper surface via wax mixture coating, Chemical Engineering Journal. 250 (2014) 431–436. doi:10.1016/j.cej.2014.04.050.

[11]   I. Rodríguez-Meizoso, O. Werner, C. Quan, Z. Knez, C. Turner, Phase-behavior of alkyl ketene dimmer (AKD) in supercritical carbon dioxide. the implications of using different solubility measurement methods, Journal of Supercritical Fluids. 61 (2012) 25–33. doi:10.1016/j.supflu.2011.09.010.

[12]   I. Rodriguez-Meizoso, P. Lazor, C. Turner, In situ Raman spectroscopy for the evaluation of solubility in supercritical carbon dioxide mixtures, Journal of Supercritical Fluids. 65 (2012) 87–92. doi:10.1016/j.supflu.2012.03.002.

[13]   C. Quan, O. Werner, L. Wågberg, C. Turner, Generation of superhydrophobic paper surfaces by a rapidly expanding supercritical carbon dioxide-alkyl ketene dimer solution, Journal of Supercritical Fluids. 49 (2009) 117–124. doi:10.1016/j.supflu.2008.11.015.

[14] K. Adenekan, B. Hutton-Prager, Sticky Hydrophobic Behavior of Cellulose Substrates Impregnated with Alkyl Ketene Dimer (AKD) via Sub- and Supercritical Carbon Dioxide, Colloids and Surfaces A: Physicochemical and Engineering Aspects. 560 (2018) (Submitted).

[15] X.Y. Ling, I.Y. Phang, G.J. Vancso, J. Huskens, D.N. Reinhoudt, Stable and transparent superhydrophobic nanoparticle films, Langmuir. 25 (2009) 3260–3263. doi:10.1021/la8040715.

[16] Y.L. Zhang, J.N. Wang, Y. He, Y. He, B. Bin Xu, S. Wei, F.S. Xiao, Solvothermal synthesis of nanoporous polymer chalk for painting superhydrophobic surfaces, Langmuir. 27 (2011) 12585–12590. doi:10.1021/la2018264.

[17] P. Olin, S.B. Lindström, T. Pettersson, L. Wågberg, Water drop friction on superhydrophobic surfaces, Langmuir. 29 (2013) 9079–9089. doi:10.1021/la401152b.

[18] T. Onda, S. Shibuichi, N. Satoh, K. Tsujii, Super-Water-Repellent Fractal Surfaces, Langmuir. 12 (1996) 2125–2127. doi:10.1021/la950418o.

[19] S.H. Kim, Fabrication of superhydrophobic surfaces, Journal of Adhesion Science and Technology. 22 (2008) 235–250. doi:10.1163/156856108X305156.

[20] X. Zhang, F. Shi, J. Niu, Y. Jiang, Z. Wang, Superhydrophobic surfaces: from structural control to functional application, J. Mater. Chem. 18 (2008) 621–633. doi:10.1039/B711226B.

[21] M. Ma, R.M. Hill, Superhydrophobic surfaces, Current Opinion in Colloid and Interface Science. 11 (2006) 193–202. doi:10.1016/j.cocis.2006.06.002.

[22] X. Wang, R.A. Weiss, A facile method for preparing sticky, hydrophobic polymer surfaces, Langmuir. 28 (2012) 3298–3305. doi:10.1021/la204564b.

[23] B. Zhang, B. Liu, X. Deng, S. Cao, X. Hou, H. Chen, A novel approach for the preparation of organic-siloxane oligomers and the creation of hydrophobic surface, Applied Surface Science. 254 (2007) 452–458. doi:10.1016/j.apsusc.2007.06.030.

[24] L. Li, V. Breedveld, D.W. Hess, Design and fabrication of superamphiphobic paper surfaces, ACS Applied Materials and Interfaces. 5 (2013) 5381–5386. doi:10.1021/am401436m.

[25] L. Jiang, Z. Tang, R.M. Clinton, V. Breedveld, D.W. Hess, Two-Step Process To Create "Roll-Off" Superamphiphobic Paper Surfaces, ACS Applied Materials and Interfaces. 9 (2017) 9195–9203. doi:10.1021/acsami.7b00829.

[26] M. Nicolas, Acids and alkali resistant sticky superhydrophobic surfaces by one-pot electropolymerization of perfluoroalkyl alkyl pyrrole, Journal of Colloid and Interface Science. 343 (2010) 608–614. doi:10.1016/j.jcis.2009.11.052.

[27] S. Chen, Y. Song, F. Xu, Highly Transparent and Hazy Cellulose Nanopaper Simultaneously with a Self-Cleaning Superhydrophobic Surface, ACS Sustainable Chemistry and Engineering. 6 (2018) 5173–5181. doi:10.1021/acssuschemeng.7b04814.

[28] L. Ejenstam, L. Ovaskainen, I. Rodriguez-Meizoso, L. Wågberg, J. Pan, A. Swerin, P.M. Claesson, The effect of superhydrophobic wetting state on corrosion protection - The AKD example, Journal of Colloid and Interface Science. 412 (2013) 56–64. doi:10.1016/j.jcis.2013.09.006.

[29] H. Zhang, X. Zeng, Y. Gao, F. Shi, P. Zhang, J.F. Chen, A facile method to prepare superhydrophobic coatings by calcium carbonate, Industrial and Engineering Chemistry Research. 50 (2011) 3089–3094. doi:10.1021/ie102149y.

[30]   A.M.A. Mohamed, A.M. Abdullah, N.A. Younan, Corrosion behavior of superhydrophobic surfaces: A review, Arabian Journal of Chemistry. 8 (2015) 749–765. doi:10.1016/j.arabjc.2014.03.006.

[31]   Y. Liu, X. Chen, J.H. Xin, Super-hydrophobic surfaces from a simple coating method: A bionic nanoengineering approach, Nanotechnology. 17 (2006) 3259–3263. doi:10.1088/0957-4484/17/13/030.

[32]   D. Khojasteh, M. Kazerooni, S. Salarian, R. Kamali, Droplet impact on superhydrophobic surfaces: A review of recent developments, Journal of Industrial and Engineering Chemistry. 42 (2016) 1–14. doi:10.1016/j.jiec.2016.07.027.

[33]   N.J. Shirtcliffe, G. McHale, S. Atherton, M.I. Newton, An introduction to superhydrophobicity, Advances in Colloid and Interface Science. 161 (2010) 124–138. doi:10.1016/j.cis.2009.11.001.

[34]   Y. Lin, D. Gritsenko, Q. Liu, X. Lu, J. Xu, Recent Advancements in Functionalized Paper-Based Electronics, ACS Applied Materials and Interfaces. 8 (2016) 20501–20515. doi:10.1021/acsami.6b04854.

[35]   J. Drelich, A. Marmur, Physics and applications of superhydrophobic and superhydrophilic surfaces and coatings, Surface Innovations. 2 (2014) 211–227. doi:10.1680/si.13.00017.

[36]   H. Yang, Y. Deng, Preparation and physical properties of superhydrophobic papers, Journal of Colloid and Interface Science. 325 (2008) 588–593. doi:10.1016/j.jcis.2008.06.034.

[37] P. Samyn, Wetting and hydrophobic modification of cellulose surfaces for paper applications, Journal of Materials Science. 48 (2013) 6455–6498. doi:10.1007/s10853-013-7519-y.

[38] N. Bordenave, S. Grelier, V. Coma, Hydrophobization and antimicrobial activity of chitosan and paper-based packaging material, Biomacromolecules. 11 (2010) 88–96. doi:10.1021/bm9009528.

[39] A.M. Olsson, L. Salmén, The association of water to cellulose and hemicellulose in paper examined by FTIR spectroscopy, Carbohydrate Research. 339 (2004) 813–818. doi:10.1016/j.carres.2004.01.005.

[40] P. Fardim, Fiber Surface and Went End Chemistry, Paper and Surface Chemistry. (n.d.) 1–14.

[41] X. Zhang, W. Batchelor, W. Shen, Building Dual-Scale Roughness Using Inorganic Pigments for Fabrication of Superhydrophobic Paper, Industrial and Engineering Chemistry Research. 56 (2017) 3618–3628. doi:10.1021/acs.iecr.7b00225.

[42] G. Garnier, M. Bertin, M. Smrckova, Wetting dynamics of alkyl ketene dimer on cellulosic model surfaces, Langmuir. 15 (1999) 7863–7869. doi:10.1021/la990297i.

[43] E. Vazirinasab, R. Jafari, G. Momen, Application of superhydrophobic coatings as a corrosion barrier: A review, Surface and Coatings Technology. 341 (2018) 40–56. doi:10.1016/j.surfcoat.2017.11.053.

[44] W. Wang, K. Lockwood, L.M. Boyd, M.D. Davidson, S. Movafaghi, H. Vahabi, S.R. Khetani, A.K. Kota, Superhydrophobic Coatings with Edible Materials, ACS Applied Materials & Interfaces. 8 (2016) 18664–18668. doi:10.1021/acsami.6b06958.

[45] G. Garnier, J. Wright, L. Godbout, L. Yu, Wetting mechanism of alkyl ketene dimers on cellulose films, Colloids and Surfaces A: Physicochemical and Engineering Aspects. 145 (1998) 153–165. doi:10.1016/S0927-7757(98)00668-2.

[46] S. Shibuichi, T. Onda, N. Satoh, K. Tsujii, Super water-repellent surfaces resulting from fractal structure, Journal of Physical Chemistry. 100 (1996) 19512–19517. doi:10.1021/jp9616728.

[47] H. Yokoyama, K. Sugiyama, Surface hydrophobicity of fluorinated block copolymers enhanced by supercritical carbon dioxide annealing, Langmuir. 20 (2004) 10001–10006. doi:10.1021/la0495231.

[48] J. Bravo, L. Zhai, Z. Wu, R.E. Cohen, M.F. Rubner, Transparent superhydrophobic films based on silica nanoparticles, Langmuir. 23 (2007) 7293–7298. doi:10.1021/la070159q.

[49] I. Torun, M.S. Onses, Robust superhydrophobicity on paper: Protection of spray-coated nanoparticles against mechanical wear by the microstructure of paper, Surface and Coatings Technology. 319 (2017) 301–308. doi:10.1016/j.surfcoat.2017.04.009.

[50] T. Arbatan, L. Zhang, X.Y. Fang, W. Shen, Cellulose nanofibers as binder for fabrication of superhydrophobic paper, Chemical Engineering Journal. 210 (2012) 74–79. doi:10.1016/j.cej.2012.08.074.

[51] A. Geissler, F. Loyal, M. Biesalski, K. Zhang, Thermo-responsive superhydrophobic paper using nanostructured cellulose stearoyl ester, Cellulose. 21 (2014) 357–366. doi:10.1007/s10570-013-0160-8.

[52] S. Das, S. Kumar, S.K. Samal, S. Mohanty, S.K. Nayak, A Review on Superhydrophobic Polymer Nanocoatings: Recent Development and Applications, Industrial and Engineering Chemistry Research. 57 (2018) 2727–2745. doi:10.1021/acs.iecr.7b04887.

[53] B.H. Hutton, I.H. Parker, Immediate consolidation behaviour of aqueous pigment coatings applied to porous substrates, Chemical Engineering Science. 63 (2008) 3348–3357. doi:10.1016/j.ces.2008.03.039.

[54] B. Balu, V. Breedveld, D.W. Hess, Fabrication of "roll-off" and "sticky" superhydrophobic cellulose surfaces-via plasma processing, Langmuir. 24 (2008) 4785–4790. doi:10.1021/la703766c.

[55] H.B. Eral, D.J.C.M. 't Mannetje, J.M. Oh, Contact angle hysteresis: a review of fundamentals and applications, Colloid and Polymer Science. 291 (2013) 247–260. doi:10.1007/s00396-012-2796-6.

[56] M. Miwa, A. Nakajima, A. Fujishima, K. Hashimoto, T. Watanabe, Effects of the surface roughness on sliding angles of water droplets on superhydrophobic surfaces, Langmuir. 16 (2000) 5754–5760. doi:10.1021/la991660o.

[57] T. Furuta, M. Sakai, T. Isobe, S. Matsushita, A. Nakajima, Sliding of water droplets on hydrophobic surfaces with various hydrophilic region sizes, Langmuir. 27 (2011) 7307–7313. doi:10.1021/la200396v.

[58] C.W. Extrand, S.I. Moon, Repellency of the lotus leaf: Contact angles, drop retention, and sliding angles, Langmuir. 30 (2014) 8791–8797. doi:10.1021/la5019482.

[59] G. McHale, N.J. Shirtcliffe, M.I. Newton, Contact-angle hysteresis on super-hydrophobic surfaces, Langmuir. 20 (2004) 10146–10149. doi:10.1021/la0486584.

[60] L. Li, V. Breedveld, D.W. Hess, Hysteresis controlled water droplet splitting on superhydrophobic paper, Colloid and Polymer Science. 291 (2013) 417–426. doi:10.1007/s00396-012-2755-2.

[61] L. Gao, T.J. McCarthy, Contact angle hysteresis explained, Langmuir. 22 (2006) 6234–6237. doi:10.1021/la060254j.

[62] C. Lv, C. Yang, P. Hao, F. He, Q. Zheng, Sliding of water droplets on microstructured hydrophobic surfaces, Langmuir. 26 (2010) 8704–8708. doi:10.1021/la9044495.

[63] R. Tadmor, K. Chaurasia, P.S. Yadav, A. Leh, P. Bahadur, L. Dang, W.R. Hoffer, Drop retention force as a function of resting time, Langmuir. 24 (2008) 9370–9374. doi:10.1021/la7040696.

[64] S. Chen, B. Zhang, X. Gao, Z. Liu, X. Zhang, Direction Dependence of Adhesion Force for Droplets on Rough Substrates, Langmuir. 33 (2017) 2472–2476. doi:10.1021/acs.langmuir.6b04668.

[65] P. Olin, C. Hyll, L. Ovaskainen, M. Ruda, O. Schmidt, C. Turner, L. Wågberg, Development of a semicontinuous spray process for the production of superhydrophobic coatings from supercritical carbon dioxide solutions, Industrial and Engineering Chemistry Research. 54 (2015) 1059–1067. doi:10.1021/ie503798k.

[66] M. a Hubbe, Acidic and alkaline sizings for printing, writing, and drawing papers, The Book & Paper Group Annual. 23 (2004) 139–151.

[67] B. Crouse, W. D, Number 361 Alkaline Papermaking: an Overview, Institute of Paper Science and Technology Atlanta, Georgia. 35 (1990). https://smartech.gatech.edu/bitstream/handle/1853/2159/tps-361.pdf.

[68] R. Seppänen, On the internal sizing mechanisms of paper with AKD and ASA related to surface chemistry , wettability and friction, 2007.

[69] Y.H. Guo, J.J. Guo, H. Miao, L.J. Teng, Z. Huang, Properties and paper sizing application of waterborne polyurethane emulsions synthesized with isophorone diisocyanate, Progress in Organic Coatings. 77 (2014) 988–996. doi:10.1016/j.porgcoat.2014.02.003.

[70] B. Excellence, CPL - Chalmers Publication Library, (2014) 2014. doi:10.4208/cicp.161112.230713a.

[71] R. Seppänen, Durability of the sizing degree of AKD and ASA sized papers investigated by contact Angle measurements and ToF-SIMS, Journal of Dispersion Science and Technology. 30 (2009) 937–948. doi:10.1080/01932690802646330.

[72] J. Lindfors, Adhesion of Reactive Sizes and Paper Machine, 2007.

[73] X. Song, F. Chen, F. Liu, Preparation and characterization of alkyl ketene dimer (AKD) modified cellulose composite membrane, Carbohydrate Polymers. 88 (2012) 417–421. doi:10.1016/j.carbpol.2011.10.062.

[74] O. Werner, C. Quan, C. Turner, B. Pettersson, L. Wågberg, Properties of superhydrophobic paper treated with rapid expansion of supercritical CO2 containing a crystallizing wax, Cellulose. 17 (2010) 187–198. doi:10.1007/s10570-009-9374-1.

[75] T. Lindström, T. Larsson, A note on AKD-sizing An investigation of real and apparent spreading / diffusion of AKD on cellulose A Note on AKD-Sizing An Investigation of Real and Apparent, (2010).

[76] W. Shen, I.H. Parker, A preliminary study of the spreading of AKD in the presence of capillary structures, Journal of Colloid and Interface Science. 240 (2001) 172–181. doi:10.1006/jcis.2001.7593.

[77] W. Shen, F. Xu, I.H. Parker, An experimental investigation of the redistribution behaviour of alkyl ketene dimers and their corresponding ketones, Colloids and Surfaces A: Physicochemical and Engineering Aspects. 212 (2003) 197–209. doi:10.1016/S0927-7757(02)00303-5.

[78] W. Shen, N. Brack, H. Ly, I.H. Parker, P.J. Pigram, J. Liesegang, Mechanism of AKD migration studied on glass surfaces, Colloids and Surfaces A: Physicochemical and Engineering Aspects. 176 (2001) 129–137. doi:10.1016/S0927-7757(00)00694-4.

[79] S. Kumar, V.S. Chauhan, S.K. Chakrabarti, Separation and analysis techniques for bound and unbound alkyl ketene dimer (AKD) in paper: A review, Arabian Journal of Chemistry. 9 (2016) S1636–S1642. doi:10.1016/j.arabjc.2012.04.019.

[80] K. Mohlin, K. Holmberg, J. Esquena, C. Solans, Study of low energy emulsification of alkyl ketene dimer related to the phase behavior of the system, Colloids and Surfaces A: Physicochemical and Engineering Aspects. 218 (2003) 189–200. doi:10.1016/S0927-7757(02)00585-X.

[81] X. Song, F. Chen, F. Liu, Study on the reaction of alkyl ketene dimer (AKD) and cellulose fiber, BioResources. 7 (2012) 652–662.

[82] Z. Shi, F. Fu, S. Wang, S. He, R. Yang, Modification of chinese fir with alkyl ketene dimer (AKD): Processing and characterization, BioResources. 8 (2013) 581–591.

[83] A.I. Bolivar, R.A. Venditti, J.J. Pawlak, K. El-Tahlawy, Development and characterization of novel starch and alkyl ketene dimer microcellular foam particles, Carbohydrate Polymers. 69 (2007) 262–271. doi:10.1016/j.carbpol.2006.10.004.

[84]   K. El-Tahlawy, R. Venditti, J. Pawlak, Effect of alkyl ketene dimer reacted starch on the properties of starch microcellular foam using a solvent exchange technique, Carbohydrate Polymers. 73 (2008) 133–142. doi:10.1016/j.carbpol.2007.11.013.

[85]   D. Lin, Y. Kuang, G. Chen, Q. Kuang, C. Wang, P. Zhu, C. Peng, Z. Fang, Enhancing moisture resistance of starch-coated paper by improving the film forming capability of starch film, Industrial Crops and Products. 100 (2017) 12–18. doi:10.1016/j.indcrop.2017.02.013.

[86]   History and Uses of Paraffin Wax, Nature. 135 (1935) 113. http://dx.doi.org/10.1038/135113a0.

[87]   P. Weber, H.L. Dunlap, Solubility of Paraffin Wax in Pure Hydrocarbons, Industrial and Engineering Chemistry. 20 (1928) 383–384. doi:10.1021/ie50220a022.

[88]   S. Kim, H. Moon, J. Kim, Thermal characterizations of the paraffin wax/low density polyethylene blends as a solid fuel, Thermochimica Acta. 613 (2015) 9–16. doi:10.1016/j.tca.2015.05.016.

[89]   T. Chartier, E. Delhomme, J.F. Baumard, P. Marteau, P. Subra, R. Tufeu, Solubility, in supercritical carbon dioxide, of paraffin waxes used as binders for low-pressure injection molding, Industrial and Engineering Chemistry Research. 38 (1999) 1904–1910. doi:10.1021/ie980552e.

[90]   D. Zhang, H. Xiao, Dual-functional beeswaxes on enhancing antimicrobial activity and water vapor barrier property of paper, ACS Applied Materials and Interfaces. 5 (2013) 3464–3468. doi:10.1021/am400585m.

[91]   M.D. Gordillo, M.A. Blanco, C. Pereyra, E.J. Martínez De La Ossa, Thermodynamic modelling of supercritical fluid-solid phase equilibrium data, Computers and Chemical Engineering. 29 (2005) 1885–1890. doi:10.1016/j.compchemeng.2005.04.001.

[92]   S. Jafari Nejad, H. Abolghasemi, M.A. Moosavian, M.G. Maragheh, Prediction of solute solubility in supercritical carbon dioxide: A novel semi-empirical model, Chemical Engineering Research and Design. 88 (2010) 893–898. doi:10.1016/j.cherd.2009.12.006.

[93]   O.H. Nautiyal, Theory of Supercritical Fluid Extraction and its Global Challenges and Strategies for Control , Utilization of CO 2 for Sustainable Development for entire Chemical Processing, (n.d.) 377–430.

[94]   E. Kiran, Supercritical fluids and polymers - The year in review - 2014, Journal of Supercritical Fluids. 110 (2016) 126–153. doi:10.1016/j.supflu.2015.11.011.

[95]   Knez, E. Markočič, M. Leitgeb, M. Primožič, M. Knez Hrnčič, M. Škerget, Industrial applications of supercritical fluids: A review, Energy. 77 (2014) 235–243. doi:10.1016/j.energy.2014.07.044.

[96]   A. Haghtalab, H.S. Panah, Modeling cloud point of soluble polymers in supercritical carbon dioxide fluid using PCP-SAFT equation of state - An application in enhanced oil recovery, Journal of Supercritical Fluids. 97 (2015) 45–50. doi:10.1016/j.supflu.2014.11.005.

[97]   L.M.A.S. Campos, E.M.Z. Michielin, L. Danielski, S.R.S. Ferreira, Experimental data and modeling the supercritical fluid extraction of marigold (Calendula officinalis) oleoresin, Journal of Supercritical Fluids. 34 (2005) 163–170. doi:10.1016/j.supflu.2004.11.010.

[98] N. De Zordi, I. Kikic, M. Moneghini, D. Solinas, Solubility of pharmaceutical compounds in supercritical carbon dioxide, Journal of Supercritical Fluids. 66 (2012) 16–22. doi:10.1016/j.supflu.2011.09.018.

[99] M. Perrut, Supercritical fluid applications: Industrial developments and economic issues, Industrial and Engineering Chemistry Research. 39 (2000) 4531–4535. doi:10.1021/ie000211c.

[100] J. Jin, Y. Wang, H. Liu, Z. Zhang, Determination and calculation of solubility of bisphenol A in supercritical carbon dioxide, Chemical Engineering Research and Design. 91 (2013) 158–164. doi:10.1016/j.cherd.2012.06.013.

[101] S. Do Yeo, E. Kiran, Formation of polymer particles with supercritical fluids: A review, Journal of Supercritical Fluids. 34 (2005) 287–308. doi:10.1016/j.supflu.2004.10.006.

[102] B. Li, W. Guo, W. Song, E.D. Ramsey, Determining the solubility of organic compounds in supercritical carbon dioxide using supercritical fluid chromatography directly interfaced to supercritical fluid solubility apparatus, Journal of Chemical and Engineering Data. 61 (2016) 2128–2134. doi:10.1021/acs.jced.6b00081.

[103] T. Koga, Y.S. Seo, K. Shin, Y. Zhang, M.H. Rafailovich, J.C. Sokolov, B. Chu, S.K. Satija, The role of elasticity in the anomalous swelling of polymer thin films in density fluctuating supercritical fluids, Macromolecules. 36 (2003) 5236–5243. doi:10.1021/ma021265w.

[104] K. Khimeche, P. Alessi, I. Kikic, A. Dahmani, Solubility of diamines in supercritical carbon dioxide. Experimental determination and correlation, Journal of Supercritical Fluids. 41 (2007) 10–19. doi:10.1016/j.supflu.2006.09.004.

[105] A. Jouyban, H.K. Chan, N.R. Foster, Mathematical representation of solute solubility in supercritical carbon dioxide using empirical expressions, Journal of Supercritical Fluids. 24 (2001) 19–35. doi:10.1016/S0896-8446(02)00015-3.

[106] 057 - Introduction to Solid-Fluid Equilibrium Modeling.pdf, (n.d.).

[107] D.L. Sparks, R. Hernandez, L.A. Estévez, Evaluation of density-based models for the solubility of solids in supercritical carbon dioxide and formulation of a new model, Chemical Engineering Science. 63 (2008) 4292–4301. doi:10.1016/j.ces.2008.05.031.

[108] A. Zeinolabedini Hezave, M.H. Khademi, F. Esmaeilzadeh, Measurement and modeling of mefenamic acid solubility in supercritical carbon dioxide, Fluid Phase Equilibria. 313 (2012) 140–147. doi:10.1016/j.fluid.2011.09.031.

[109] Z. Tang, J. Jin, Z. Zhang, H. Liu, New experimental data and modeling of the solubility of compounds in supercritical carbon dioxide, Industrial & Engineering Chemistry Research. 51 (2012) 5515–5526. doi:10.1021/ie2016224.

[110] Y. Masmoudi, L. Ben Azzouk, O. Forzano, J.M. Andre, E. Badens, Supercritical impregnation of intraocular lenses, Journal of Supercritical Fluids. 60 (2011) 98–105. doi:10.1016/j.supflu.2011.08.014.

[111] A. Tabernero, E.M.M. del Valle, M.Á. Galán, A comparison between semiempirical equations to predict the solubility of pharmaceutical compounds in supercritical carbon dioxide, Journal of Supercritical Fluids. 52 (2010) 161–174. doi:10.1016/j.supflu.2010.01.009.

[112] E. Reverchon, R. Adami, Nanomaterials and supercritical fluids, Journal of Supercritical Fluids. 37 (2006) 1–22. doi:10.1016/j.supflu.2005.08.003.

[113] H. Bezaze, A.H. Meniai, A predictive approach for thermodynamic modeling of solubility in supercritical fluids using genetic algorithm, International Journal of Hydrogen Energy. 42 (2017) 12920–12925. doi:10.1016/j.ijhydene.2017.01.041.

[114] S.N. Reddy, G. Madras, An association and Wilson activity coefficient model for solubilities of aromatic solid pollutants in supercritical carbon dioxide, Thermochimica Acta. 541 (2012) 49–56. doi:10.1016/j.tca.2012.04.025.

[115] M. Solana, I. Boschiero, S. Dall'Acqua, A. Bertucco, A comparison between supercritical fluid and pressurized liquid extraction methods for obtaining phenolic compounds from Asparagus officinalis L, Journal of Supercritical Fluids. 100 (2015) 201–208. doi:10.1016/j.supflu.2015.02.014.

[116] H. Sovova, R.P. Stateva, New approach to modeling supercritical CO_2 extraction of cuticular waxes: Interplay between solubility and kinetics, Industrial and Engineering Chemistry Research. 54 (2015) 4861–4870. doi:10.1021/acs.iecr.5b00741.

[117] A. Russler, M. Wieland, M. Bacher, U. Henniges, P. Miethe, F. Liebner, A. Potthast, T. Rosenau, AKD-Modification of bacterial cellulose aerogels in supercritical CO2, Cellulose. 19 (2012) 1337–1349. doi:10.1007/s10570-012-9728-y.

[118] B. Agustin, S.Y. Lin, A. Kurniawan, Y.H. Ju, F.E. Soetaredjo, S. Ismadji, Solubilities of 3-acetylpyridine in supercritical carbon dioxide at several temperatures and pressures: Experimental and modeling, Fluid Phase Equilibria. 354 (2013) 127–132. doi:10.1016/j.fluid.2013.06.036.

[119] B. Li, W. Guo, E.D. Ramsey, Determining the Solubility of Nifedipine and Quinine in Supercritical Fluid Carbon Dioxide Using Continuously Stirred Static Solubility Apparatus Interfaced with Online Supercritical Fluid Chromatography, Journal of Chemical and Engineering Data. 62 (2017) 1530–1537. doi:10.1021/acs.jced.7b00012.

[120] I. Kikic, M. Lora, A. Bertucco, A Thermodynamic Analysis of Three-Phase Equilibria in Binary and Ternary Systems for Applications in Rapid Expansion of a Supercritical Solution (RESS), Particles from Gas-Saturated Solutions (PGSS), and Supercritical Antisolvent (SAS), Industrial and Engineering Chemistry Research. 36 (1997) 5507–5515. doi:10.1021/ie970376u.

[121] C.S. Yoo, A. Sengupta, M. Kim, Phase diagram of carbon dioxide: Update and challenges, High Pressure Research. 31 (2011) 68–74. doi:10.1080/08957959.2010.523000.

[122] V.T. Lieu, A simple experiment for demonstration of phase diagram of carbon dioxide, Journal of Chemical Education. 73 (1996) 837. doi:doi: 10.1021/ed073p837.2.

[123] M. Zorca, I. Găinar, D. Bala, The CO2 density variation in SFE of anet essential oils, Analele Universităţii Din Bucureşti – Chimie, Anul XVI. I (2007) 43–47.

[124] E. Ruckenstein, I. Shulgin, A simple equation for the solubility of a solid in a supercritical fluid cosolvent with a gas or another supercritical fluid, Industrial and Engineering Chemistry Research. 42 (2003) 1106–1110. doi:10.1021/ie020871c.

[125] W. Hutchenson Keith, R. Foster Neil, Innovations in Supercritical Fluid Science and Technology, Innovations in Supercritical Fluids. 608 (1995) 1–31. doi:doi:10.1021/bk-1995-0608.ch001.

[126] S. Focus, E. Application, S. Fluid, Special Focus on Environmental Application of Supercritical Fluid Supercritical fluids : Fundamentals and Applications, (2014).

[127] W. Hayduk, E.B. Walter, P. Simpson, Solubility of Propane and Carbon Dioxide in Heptane, Dodecane, and Hexadecane, Journal of Chemical and Engineering Data. 17 (1972) 59–61. doi:10.1021/je60052a018.

[128] A. Kalaga, M. Trebble, Density Changes in Supercritical Solvent + Hydrocarbon Solute Binary Mixtures, Journal of Chemical & Engineering Data. 44 (1999) 1063–1066. doi:10.1021/je990029m.

[129] A.R.C. Duarte, S. Santiago, H.C. De Sousa, C.M.M. Duarte, Solubility of acetazolamide in supercritical carbon dioxide in the presence of ethanol as a cosolvent, Journal of Chemical and Engineering Data. 50 (2005) 216–220. doi:10.1021/je049722m.

[130] S. Zhan, L. Cui, Q. Zhao, L. Chen, J. Wang, S. Chen, S. Ding, Measurement and correlation of solubility of nitrendipine in supercritical carbon dioxide with and without ethanol cosolvent, Journal of Solution Chemistry. 44 (2015) 1–15. doi:10.1007/s10953-014-0262-4.

[131] A.I. Frolov, M.G. Kiselev, Prediction of cosolvent effect on solvation free energies and solubilities of organic compounds in supercritical carbon dioxide based on fully atomistic molecular simulations, Journal of Physical Chemistry B. 118 (2014) 11769–11780. doi:10.1021/jp505731z.

[132] Q. Li, C. Zhong, Z. Zhang, Q. Zhou, Modeling of the solubility of solid solutes in supercritical CO2with and without cosolvent using solution theory, Korean Journal of Chemical Engineering. 21 (2004) 1173–1177. doi:10.1007/BF02719490.

[133] Q. Li, Z. Zhang, C. Zhong, Y. Liu, Q. Zhou, Solubility of solid solutes in supercritical carbon dioxide with and without cosolvents, Fluid Phase Equilibria. 207 (2003) 183–192. doi:10.1016/S0378-3812(03)00022-0.

[134] S. Goldman, C.G. Gray, W. Li, B. Tomberli, C.G. Joslin, Predicting solubilities in supercritical fluids, Journal of Physical Chemistry. 100 (1996) 7246–7249. doi:10.1021/jp953286g.

[135] K.P. Johnston, J.M. Dobbs, J.M. Wong, Nonpolar Co-Solvents for Solubility Enhancement in Supercritical Fluid Carbon Dioxide, Journal of Chemical and Engineering Data. 31 (1986) 303–308. doi:10.1021/je00045a014.

[136] S. Li, S. Zhang, X. Wang, Fabrication of superhydrophobic cellulose-based materials through a solution-immersion process, Langmuir. 24 (2008) 5585–5590. doi:10.1021/la800157t.

[137] H. Zhang, D. Kannangara, M. Hilder, R. Ettl, W. Shen, The role of vapour deposition in the hydrophobization treatment of cellulose fibres using alkyl ketene dimers and alkenyl succinic acid anhydrides, Colloids and Surfaces A: Physicochemical and Engineering Aspects. 297 (2007) 203–210. doi:10.1016/j.colsurfa.2006.10.059.

[138] W. Shen, H. Zhang, R. Ettl, Chemical composition of "AKD vapour" and its implication to AKD vapour sizing, Cellulose. 12 (2005) 641–652. doi:10.1007/s10570-005-9010-7.

[139] V.K. Rastogi, D. Stanssens, P. Samyn, Mechanism for tuning the hydrophobicity of microfibrillated cellulose films by controlled thermal release of encapsulated wax, Materials. 7 (2014) 7196–7216. doi:10.3390/ma7117196.

[140] X. Ye, C.M. Wai, Making Nanomaterials in Supercritical Fluids: A Review, Journal of Chemical Education. 80 (2003) 198. doi:10.1021/ed080p198.

[141] I. Asghari, F. Esmaeilzadeh, Investigation of key influence parameters for synthesis of submicron carboxymethylcellulose particles via rapid expansion of supercritical CO2solution by Taguchi method, Journal of Supercritical Fluids. 69 (2012) 34–44. doi:10.1016/j.supflu.2012.05.001.

[142] L. Ovaskainen, S. Chigome, N.A. Birkin, S.M. Howdle, N. Torto, L. Wa˚gberg, C. Turner, Superhydrophobic polymeric coatings produced by rapid expansion of supercritical solutions combined with electrostatic deposition (RESS-ED), Journal of Supercritical Fluids. 95 (2014) 610–617. doi:10.1016/j.supflu.2014.09.014.

[143] L. Ovaskainen, I. Rodriguez-Meizoso, N.A. Birkin, S.M. Howdle, U. Gedde, L. Wågberg, C. Turner, Towards superhydrophobic coatings made by non-fluorinated polymers sprayed from a supercritical solution, Journal of Supercritical Fluids. 77 (2013) 134–141. doi:10.1016/j.supflu.2013.02.019.

[144] Q. Shi, L. Jing, W. Qiao, Solubility of n-alkanes in supercritical CO2at diverse temperature and pressure, Journal of CO2 Utilization. 9 (2015) 29–38. doi:10.1016/j.jcou.2014.12.002.

[145] F.H. MacLaren, Evaluation of Quality of Paraffin Wax, Industrial & Engineering Chemistry. 42 (1950) 2134–2141. doi:10.1021/ie50490a036.

[146] S.B. Hozhabr, S.H. Mazloumi, J. Sargolzaei, Correlation of solute solubility in supercritical carbon dioxide using a new empirical equation, Chemical Engineering Research and Design. 92 (2014) 2734–2739. doi:10.1016/j.cherd.2014.01.026.

[147] C. Tang, Y.-X. Guan, S.-J. Yao, Z.-Q. Zhu, Solubility of Dexamethasone in Supercritical Carbon Dioxide with and without a Cosolvent, Journal of Chemical & Engineering Data. 59 (2014) 3359–3364. doi:10.1021/je500345n.

[148] G. Sherman, S. Shenoy, R.A. Weiss, C. Erkey, A static method coupled with gravimetric analysis for the determination of solubilities of solids in supercritical carbon dioxide, Industrial and Engineering Chemistry Research. 39 (2000) 846–848. doi:10.1021/ie9906924.

[149] Y. Bakhbakhi, Phase equilibria prediction of solid solute in supercritical carbon dioxide with and without a cosolvent: The use of artificial neural network, Expert Systems with Applications. 38 (2011) 11355–11362. doi:10.1016/j.eswa.2011.03.003.

[150] Ø. Wilhelmsen, A. Aasen, G. Skaugen, P. Aursand, A. Austegard, E. Aursand, M.A. Gjennestad, H. Lund, G. Linga, M. Hammer, Thermodynamic Modeling with Equations of State: Present Challenges with Established Methods, Industrial and Engineering Chemistry Research. 56 (2017) 3503–3515. doi:10.1021/acs.iecr.7b00317.

[151] J.M. Prausnitz, R.N. Linchtenthaler, G.D.A. A, Molecular Thermodynamics of Fluid-Phase Equilibria, Wiley Subscription Services, Inc., A Wiley Company, 2000. doi:10.1002/cjce.5450780222.

[152] J. Gmehling, D. Constantinescu, B. Schmid, Group Contribution Methods for Phase Equilibrium Calculations, Annual Review of Chemical and Biomolecular Engineering. 6 (2015) 267–292. doi:10.1146/annurev-chembioeng-061114-123424.

[153] W.-Y. Chen, J. Liu, Mathcad Modules for Supercritical Fluid Extraction based on Mixing Rules. Appendix A - Mixing Rules, (2007) 1–10. http://home.olemiss.edu/~cmchengs/Extraction/Appendix A_Mixing Rules.doc.

[154] C.-C. Chen, Y. Song, Solubility Modeling with a Nonrandom Two-Liquid Segment Activity Coefficient Model, Industrial & Engineering Chemistry Research. 43 (2004) 8354–8362. doi:10.1021/ie049463u.

[155] H. Orbey, S.I. Sandler, Modeling Vapor-Liquid Equilibria Cubic Equations of State and Their Mixing Rules, 1998. https://books.google.com/books?id=Gl9C1trxMDYC&pg=PA101&dq=orbey+and+sandler+bibliography&hl=en&sa=X&ved=0ahUKEwiTg5_rj6PXAhUK6YMKHYrtCZQQ6AEIJjAA#v=onepage&q=orbey and sandler bibliography&f=false (accessed November 3, 2017).

[156] Y.S. Ting, C.M. Hsieh, Prediction of solid solute solubility in supercritical carbon dioxide with organic cosolvents from the PR+COSMOSAC equation of state, Fluid Phase Equilibria. 431 (2017) 48–57. doi:10.1016/j.fluid.2016.10.008.

[157] J. Marrero, R. Gani, Group-contribution based estimation of pure component properties, Fluid Phase Equilibria. 183–184 (2001) 183–208. doi:10.1016/S0378-3812(01)00431-9.

[158] A. Vetere, Methods to predict the critical constants of organic compounds, Fluid Phase Equilibria. 109 (1995) 17–27. doi:10.1016/0378-3812(95)02715-Q.

[159] R.C. Reid, Estimation of Critical Properties with Group Contribution Methods, 30 (1984) 137–142.

[160] S. Gracin, T. Brinck, Å.C. Rasmuson, Prediction of solubility of solid organic compounds in solvents by UNIFAC, Industrial & Engineering Chemistry Research. 41 (2002) 5114–5124. doi:10.1021/ie011014w.

[161] S. Tanveer, Y. Hao, C.-C. Chen, Introduction to Solid-Fluid Equilibrium Modeling, 2014.

[162] J. Ahlers, J. Gmehling, J. Menke, M. Schiller, J. Ahlers, T. Yamaguchi, Development of a Universal Group Contribution Equation of State. 5. Prediction of the Solubility of High-Boiling Compounds in Supercritical Gases with the Group Contribution Equation of State Volume-Translated Peng-Robinson, Industrial & Engineering Chemistry Research. 5 (2004) 5890–5899. doi:10.1021/ie040037i.

[163] H. Benmekki, No Title, (n.d.).

[164] G. Li, Z. Song, W. Liu, D. Yu, H. Wang, Alkyl Ketene Dimer Emulsions Stabilized by Layered Double Hydroxide Particles Modified with Glutamic Acid, Industrial and Engineering Chemistry Research. 56 (2017) 11435–11442. doi:10.1021/acs.iecr.7b02532.

[165] M. Asgarpour Khansary, F. Amiri, A. Hosseini, A. Hallaji Sani, H. Shahbeig, Representing solute solubility in supercritical carbon dioxide: A novel empirical model, Chemical Engineering Research and Design. 93 (2015) 355–365. doi:10.1016/j.cherd.2014.05.004.

[166] B. Schmid, J. Gmehling, Revised parameters and typical results of the VTPR group contribution equation of state, Fluid Phase Equilibria. 317 (2012) 110–126. doi:10.1016/j.fluid.2012.01.006.

[167] S.I. Orbey, H., & Sandler, Modeling vapor-liquid equilibria: Cubic equations of state and their mixing rules., 1998.

[168] G.M. Kontogeorgis, D.P. Tassios, Critical constants and acentric factors for long-chain alkanes suitable for corresponding states applications. A critical review, Chemical Engineering Journal. 66 (1997) 35–49. doi:10.1016/S1385-8947(96)03146-4.

[169] K.G. Joback, R.C. Reid, Estimation of Pure-Component Properties from Group-Contributions, Chemical Engineering Communications. 57 (1987) 233–243. doi:10.1080/00986448708960487.

[170] J.O. Valderrama, W.W. Sanga, J.A. Lazzús, Critical properties, normal boiling temperature, and acentric factor of another 200 ionic liquids, Industrial and Engineering Chemistry Research. 47 (2008) 1318–1330. doi:10.1021/ie071055d.

[171] J.F. Brennecke, M.A. Stadtherr, Solubility measurements and modeling of molecules of biological and pharmaceutical interest with supercritical CO 2, 220 (2004) 57–69. doi:10.1016/j.fluid.2004.01.036.

[172] S. Lee, J. Jeon, W. Kim, A New Model Approach for the Near-Critical Point Region : 1 . Construction of the Generalized van der Waals Equation of State, (2008) 15725–15741.

[173] P.P. Bezverkhii, V.G. Martynets, E. V Matizen, A scaling equation of state near the critical point and the stability boundary of a liquid, Journal of Engineering Thermophysics. 16 (2007) 164–168. doi:10.1134/S1810232807030083.

[174] F. Fornasiero, L. Lue, A. Bertucco, Improving cubic EOSs near the critical point by a phase-space cell approximation, AIChE Journal. 45 (1999) 906–915. doi:10.1002/aic.690450421.

[175] R.D. Hagenmaier, R.A. Baker, Edible Coatings from Morpholine-Free Wax Microemulsions, Journal of Agricultural and Food Chemistry. 45 (1997) 349–352. doi:10.1021/jf9604551.

[176] S.E. Stein, R.L. Brown, Estimation of Normal Boiling Points from Group Contributions, Journal of Chemical Information and Computer Sciences. 34 (1994) 581–587. doi:10.1021/ci00019a016.

[177] N.M. Hancock, M.E.P. De Fernandez, D. Ph, No Title, (n.d.).

[178] C.H. Tu, Group-contribution method for the estimation of vapor pressures, Fluid Phase Equilibria. 99 (1994) 105–120. doi:10.1016/0378-3812(94)80025-1.

[179] D.H. Chen, M. V. Dinivahi, C.Y. Jeng, New Acentric Factor Correlation Based on the Antoine Equation, Industrial and Engineering Chemistry Research. 32 (1993) 241–244. doi:10.1021/ie00013a034.

[180] Y. Zhao, W. Liu, Z. Wu, Solubility model of solid solute in supercritical fluid solvent based on unifac, Industrial and Engineering Chemistry Research. 49 (2010) 5952–5957. doi:10.1021/ie100656v.

[181] H.S. Ghaziaskar, M. Kaboudvand, Solubility of Tridodecylamine in Supercritical Carbon Dioxide, 2 (n.d.).

[182] N.R. Foster, G.S. Gurdial, J.S.L. Yun, K.K. Liong, K.D. Tilly, S.S.T. Ting, H. Singh, J.H. Lee, Significance of the Crossover Pressure in Solid-Supercritical Fluid Phase Equilibria, Industrial and Engineering Chemistry Research. 30 (1991) 1955–1964. doi:10.1021/ie00056a044.

[183] S. Junsophonsri, Solubility of Biocides in Pure and Modified Supercritical Carbon Dioxide., (2004) 1–69.

[184] R. Span, W. Wagner, A New Equation of State for Carbon Dioxide Covering the Fluid Region from the Triple-Point Temperature to 1100 K at Pressures up to 800 MPa, 25 (1996).

[185] W.F. Reynolds (Ed.), The Sizing of Paper, TAPPI Press, USA. 2nd ed (1989) 135.

[186] O. Werner, C. Turner, Investigation of different particle sizes on superhydrophobic surfaces made by rapid expansion of supercritical solution with in situ laser diffraction (RESS-LD), Journal of Supercritical Fluids. 67 (2012) 53–59. doi:10.1016/j.supflu.2012.03.008.

[187] A. V. Shchukarev, R. Mattsson, L. Ödberg, XPS imaging of surface diffusion of alkylketene dimer on paper surfaces, Colloids and Surfaces A: Physicochemical and Engineering Aspects. 219 (2003) 35–43. doi:10.1016/S0927-7757(03)00009-8.

[188] A. Baiker, Supercritical Fluids in Heterogeneous Catalysis, Chemical Reviews. 99 (1999) 453–474. doi:10.1021/cr970090z.

[189] Z. Yang, X.F. Peng, D.J. Lee, M.Y. Chen, An image-based method for obtaining pore-size distribution of porous media, Environmental Science and Technology. 43 (2009) 3248–3253. doi:10.1021/es900097e.

[190] W.M. Sigmund, S.-H. Hsu, Cassie--Baxter Model, in: E. Drioli, L. Giorno (Eds.), Encyclopedia of Membranes, Springer Berlin Heidelberg, Berlin, Heidelberg, 2016: pp. 310–311. doi:10.1007/978-3-662-44324-8_1381.

[191] J. McMurry, Organic chemistry, Brooks/Cole Cengage Learning, Singapore, 2012.

[192] E.T.J. Nibbering, J. Dreyer, O. Kuhn, J. Bredenbeck, P. Hamm, T. Elsaesser, Vibrational dynamics of hydrogen bonds, Analysis and Control of Ultrafast Photoinduced Reactions. (2007).

[193] T. Gonjo, Y. Futami, Y. Morisawa, M.J. Wojcik, Y. Ozaki, Hydrogen Bonding Effects on the Wavenumbers and Absorption Intensities of the OH Fundamental and the First, Second, and Third Overtones of Phenol and 2,6-Dihalogenated Phenols Studied by Visible/Near-Infrared/Infrared Spectroscopy, The Journal of Physical Chemistry A. 115 (2011) 9845–9853. doi:10.1021/jp201733n.

[194] S.L. Dhere, U.K.H. Bangi, S.S. Latthe, A.V. Rao, Journal of Physics and Chemistry of Solids Enhancement in hydrophobicity of silica films using metal acetylacetonate and heat treatment, Journal of Physical and Chemistry of Solids. 72 (2011) 45–49. doi:10.1016/j.jpcs.2010.10.086.

[195] P. Wang, X. Qian, J. Shen, Superhydrophobic coatings with edible biowaxes for reducing or eliminating liquid residues of foods and drinks in containers, BioResources. 13 (2018) 1–2. doi:10.1021/acsami.6b06958.

[196] Z. Wang, Y. Li, L. Jiang, B. Qi, L. Zhou, Relationship between Secondary Structure and Surface Hydrophobicity of Soybean Protein Isolate Subjected to Heat Treatment, 2014 (2014).

[197] C.R. Reshmi, S.P. Sundaran, A. Juraij, S. Athiyanathil, RSC Advances Fabrication of superhydrophobic polycaprolactone / beeswax electrospun separation †, RSC Advances. 7 (2016) 2092–2102. doi:10.1039/C6RA26123J.

[198] T. Kameda, Molecular structure of crude beeswax studied by solid-state 13 C NMR, (2004).

[199] A.P. Tulloch, Beeswax — Composition and Analysis, (2016). doi:10.1080/0005772X.1980.11097776.

[200] S. Abdikheibari, R. Parvizi, M.H. Moayed, S.M. Zebarjad, S.A. Sajjadi, Beeswax-Colophony Blend: A Novel Green Organic Coating for Protection of Steel Drinking Water Storage Tanks, (2015) 1645–1664. doi:10.3390/met5031645.

[201] E.W. Repellency, P. Separation, Facile Fabrication of Superhydrophobic Paper with Excellent Water Repellency and Moisture Resistance by Phase Separation, 11 (2016) 6552–6565.

[202] P. Properties, Physical , Thermal , and Barrier Characterization of Casein-Wax-Based Edible Films, (1993).

[203] V. Puttalingamma, Edible Coatings of Carnauba Wax — A Novel Method For Preservation and Extending Longevity of Fruits and Vegetables- A Review ., 16 (2014) 1–5.

[204] L. Ren, Y. Cai, L. Ren, H. Yang, Preparation of Modified Beeswax and Its Influence on the Surface Properties of Compressed Poplar Wood, (2016). doi:10.3390/ma9040230.

[205] L. Eynard, S. Iametti, P. Relkin, F. Bonomi, Surface Hydrophobicity Changes and Heat-Induced Modifications of, (1992) 1731–1736. doi:10.1021/jf00022a002.

[206] S. He, Y. Huang, G. Chen, M. Feng, H. Dai, B. Yuan, X. Chen, Effect of heat treatment on hydrophobic silica aerogel, Journal of Hazardous Materials. 362 (2019) 294–302. doi:10.1016/j.jhazmat.2018.08.087.

[207] J. Shin, S. Nouranian, A.E. Smith, Dynamic mechanical and thermal properties of cellulose nanocrystal / epoxy nanocomposites, 5 (2017) 123–134.

[208] B.V. Chechik, R.M. Crooks, C.J.M. Stirling, Reactions and Reactivity in Self-Assembled Monolayers **, (2000) 1161–1171.

[209] B. Bhushan, 25.1 Introduction, 1 (2001).

[210] N. Saba, P.M. Tahir, A Review on Dynamic mechanical analysis of natural fibre reinforced polymer composites, Construcction and Building Materials. 106 (2016) 149–159. doi:10.1016/j.conbuildmat.2015.12.075.

[211] G. and I. Rashid, Leman, Jawaid, Dynamic Mechanical Analysis of Treated and Untreated, 12 (2017) 3448–3462.

[212] N. Saba, A. Safwan, M.L. Sanyang, F. Mohammad, M. Pervaiz, M. Jawaid, O.Y. Alothman, M. Sain, International Journal of Biological Macromolecules Thermal and dynamic mechanical properties of cellulose nanofibers reinforced epoxy composites, International Journal of Biological Macromolecules. 102 (2017) 822–828. doi:10.1016/j.ijbiomac.2017.04.074.

[213] © 1967 Nature Publishing Group, (1967).

[214] I.I.A. Qamhia, Experimental and Analytical Characterization of Regenerated / nano Cellulose Composites, (2014).

LIST OF APPENDICES

LIST OF APPENDICES

APPENDIX A: THERMODYBNAMIC MODEL (MATHCAD)

$T := 313.15 K$

Modeling of extraction data

1. **Solubilities of AKD in supercritical carbon dioxide using PREOS at 313.13 K**

$R := 8.314 \dfrac{J}{mol \cdot K}$

$bar := 10^5 Pa \qquad \omega_1 := 0.225$

$T_{c1} := 304.11 K \qquad P_{c1} := 73.74 bar$

$T_{c2} := 900.95 K \qquad P_{c2} := 7.54 bar$

$\omega_2 := 1.91 \qquad MPa := 10^6 Pa$

$1 = \text{Carbon Dioxide}$

$2 = \text{AKD}$

$P1_{sat} := \dfrac{\left[10^3 \cdot \exp\left[8.5759 - \dfrac{95.5979(100K)}{T} - 3.744 \ln\left(\dfrac{T}{100K}\right) - 0.5834 \dfrac{T}{100K}\right]\right] Pa}{504} \rightarrow 1.3015183246933155355e-2 \, Pa$

$k1 := 0.378893 + 1.4897153\omega_1 - 0.26992\omega_1^2$

$a_1 := \dfrac{0.457235 R^2 \cdot T_{c1}^2}{P_{c1}} \cdot \left[1 + k1 \cdot \left[1 - \left(\dfrac{T}{T_{c1}}\right)^{0.5}\right]\right]^2 \qquad b_1 := \dfrac{0.077796 R \cdot T_{c1}}{P_{c1}}$

$k2 := 0.378893 + 1.4897153\omega_2 - 0.26992\omega_2^2$

$a_2 := \dfrac{0.457235 R^2 \cdot T_{c2}^2}{P_{c2}} \cdot \left[1 + k2 \cdot \left[1 - \left(\dfrac{T}{T_{c2}}\right)^{0.5}\right]\right]^2 \qquad b_2 := \dfrac{0.077796 R \cdot T_{c2}}{P_{c2}}$

$a_{12}(k12) := \left(a_1 \cdot a_2\right)^{0.5} \cdot (1 - k12) \qquad\qquad b(y2) := (1 - y2) \cdot b_1 + y2 \cdot b_2$

$a(y2, k12) := (1 - y2)^2 \cdot a_1 + 2 \cdot (1 - y2) \cdot y2 \cdot a_{12}(k12) + y2^2 \cdot a_2$

$A(y2, k12, P) := \dfrac{a(y2, k12) \cdot P}{(R \, T)^2} \qquad\qquad B(y2, P) := \dfrac{b(y2) \cdot P}{R \cdot T}$

$$Z(y2, k12, P) := \text{polyroots} \begin{pmatrix} -A(y2, k12, P) \cdot B(y2, P) + B(y2, P)^2 + B(y2, P)^3 \\ A(y2, k12, P) - 3 \cdot B(y2, P)^2 - 2 \cdot B(y2, P) \\ -1 + B(y2, P) \\ 1 \end{pmatrix}$$

$$Z(y2, k12, P) := \begin{vmatrix} Z1 \leftarrow Z(y2, k12, P) \\ \text{for } i \in 0..2 \\ \quad Z1_i \leftarrow 0 \text{ if } \text{Im}(Z1_i) \neq 0 \qquad\qquad \text{set complex roots to zero} \\ Z1 \leftarrow \text{sort}(Z1) \qquad\qquad\qquad \text{sort the roots} \\ Z1_0 \leftarrow Z1_2 \text{ if } |Z1_0| < 10^{-5} \qquad \text{set values of any complex root} \\ Z1_2 \leftarrow Z1_0 \text{ if } |Z1_2| < 10^{-5} \qquad \text{to the value of the real root} \\ Z1 \end{vmatrix}$$

$$Z(y2, k12, P) := Z(y2, k12, P)_2$$

$$Vvap(y2, k12, P) := \frac{Z(y2, k12, P) \cdot R \cdot T}{P}$$

$$\phi(y2, k12, P) := \exp\left[\frac{b_2}{b(y2)} \cdot (Z(y2, k12, P) - 1) - \ln(Z(y2, k12, P) - B(y2, P)) \ldots \right.$$
$$\left. + \frac{-a(y2, k12)}{2 \cdot \sqrt{2} \cdot b(y2) \cdot R \cdot T} \cdot \left[\left[\frac{2 \cdot [(1 - y2) \cdot a_{12}(k12) + y2 \cdot a_2]}{a(y2, k12)} - \frac{b_2}{b(y2)} \right] \cdot \ln\left[\frac{Vvap(y2, k12, P) + (1 + \sqrt{2}) \cdot b(y2)}{Vvap(y2, k12, P) + (1 - \sqrt{2}) \cdot b(y2)} \right] \right] \right]$$

$$i := 0..3$$

$$v1_s := 656.3 \cdot 10^{-6} \frac{m^3}{mol}$$

Guess

$$P0_i :=$$

98.69atm
148.035atm
197.38atm
246.332atm

$$y0_i :=$$

0.00012
0.0022
0.0037
0.0064

$$k12 := -0.01$$

Given

$$\sum_{i=0}^{3} \left[\frac{P1_{sat}}{P0_i} \cdot \frac{1}{\phi(y0_i, k12, P0_i)} \cdot \exp\left[\frac{v1_s \cdot (P0_i - P1_{sat})}{R \cdot T} \right] - y0_i \right]^2 = 0$$

$$k12 := \text{Find}(k12)$$

<mark>$k12 = -0.05957$</mark>

$$k_{12} := k12$$

$$R := 8.314 \frac{J}{mol \cdot K} \qquad MPa := 10^6 Pa$$

$$k1(T) := 0.378893 + 1.4897153\omega_1 - 0.26992\omega_1^{\;2}$$

$$a_1(T) := \frac{0.457235 R^2 \cdot T_{c1}^{\;2}}{P_{c1}} \cdot \left[1 + k1(T) \cdot \left[1 - \left(\frac{T}{T_{c1}} \right)^{0.5} \right] \right]^2 \qquad b_1 := \frac{0.077796 R \cdot T_{c1}}{P_{c1}}$$

$$k2(T) := 0.378893 + 1.4897153\omega_2 - 0.26992\omega_2^{\;2}$$

$$a_2(T) := \frac{0.457235 R^2 \cdot T_{c2}^{\;2}}{P_{c2}} \cdot \left[1 + k2(T) \cdot \left[1 - \left(\frac{T}{T_{c2}} \right)^{0.5} \right] \right]^2 \qquad b_2 := \frac{0.077796 R \cdot T_{c2}}{P_{c2}}$$

$$a_{12}(T) := \left(a_1(T) \cdot a_2(T) \right)^{0.5} \cdot \left(1 - k_{12} \right)$$

$$a(y2, T) := (1 - y2)^2 \cdot a_1(T) + 2 \cdot (1 - y2) \cdot y2 \cdot a_{12}(T) + y2^2 \cdot a_2(T)$$

$$b(y2) := (1 - y2) \cdot b_1 + y2 \cdot b_2 \qquad B(y2, P, T) := \frac{b(y2) \cdot P}{R \cdot T} \qquad A(y2, P, T) := \frac{a(y2, T) \cdot P}{(R\,T)^2}$$

$$Z(y2, P, T) := polyroots \begin{pmatrix} -A(y2, P, T) \cdot B(y2, P, T) + B(y2, P, T)^2 + B(y2, P, T)^3 \\ A(y2, P, T) - 3 \cdot B(y2, P, T)^2 - 2 \cdot B(y2, P, T) \\ -1 + B(y2, P, T) \\ 1 \end{pmatrix}$$

$$Z(y2, P, T) := \begin{vmatrix} Z1 \leftarrow Z(y2, P, T) \\ \text{for } i \in 0..2 \\ \quad Z1_i \leftarrow 0 \;\; \text{if } Im\left(Z1_i\right) \neq 0 \\ Z1 \leftarrow sort(Z1) \\ Z1_0 \leftarrow Z1_2 \;\; \text{if } \left| Z1_0 \right| < 10^{-5} \\ Z1_2 \leftarrow Z1_0 \;\; \text{if } \left| Z1_2 \right| < 10^{-5} \\ Z1 \end{vmatrix}$$

set complex roots to zero

sort the roots

set values of any complex root

to the value of the real root

144

$$\underset{\sim}{Z}(y2, P, T) := Z(y2, P, T)_2$$

$$\underset{\sim}{Vvap}(y2, P, T) := \frac{Z(y2, P, T) \cdot R \cdot T}{P}$$

$$\underset{\sim}{\phi}(y2, P, T) := \exp\left[\frac{b_2}{b(y2)} \cdot (Z(y2, P, T) - 1) - \ln(Z(y2, P, T) - B(y2, P, T)) \dots \right.$$
$$\left. + \frac{-a(y2, T)}{2 \cdot \sqrt{2} \cdot b(y2) \cdot R \cdot T} \cdot \left[\left[\frac{2 \cdot \left[(1 - y2) \cdot a_{12}(T) + y2 \cdot a_2(T)\right]}{a(y2, T)} - \frac{b_2}{b(y2)}\right] \cdot \ln\left[\frac{Vvap(y2, P, T) + \left(1 + \sqrt{2}\right) \cdot b(y2)}{Vvap(y2, P, T) + \left(1 - \sqrt{2}\right) \cdot b(y2)}\right]\right]\right]$$

$P := 1MPa, 2MPa .. 30MPa$ \qquad $y := 0.01$

Given

$$y = \frac{P1_{sat}}{P} \cdot \frac{1}{\phi(y, P, T)} \cdot \exp\left[\frac{v1_s \cdot (P - P1_{sat})}{R \cdot T}\right]$$

$$\underset{\sim}{F}(y, P, T) := Find(y)$$

$$i := 0 .. 30$$

$y1_i :=$

0.00012
0.0022
0.0037
0.0064

$P1_i :=$

98.69
148.035
197.38
246.725

$F(y, P, T) =$

0
0
0
$3.435 \cdot 10^{-15}$
$4.428 \cdot 10^{-14}$
$8.465 \cdot 10^{-13}$
$3.01 \cdot 10^{-11}$
$3.814 \cdot 10^{-9}$
$5.31 \cdot 10^{-6}$
$1.925 \cdot 10^{-4}$
$8.352 \cdot 10^{-4}$
$1.745 \cdot 10^{-3}$
$2.544 \cdot 10^{-3}$
$3.14 \cdot 10^{-3}$
$3.571 \cdot 10^{-3}$
...

$\overline{F(y, P, T)}$

$\underset{\circ\circ\circ}{y1_i}$

$$\frac{P}{10^5}, P1_i$$

2. Solubilities of AKD in supercritical carbon dioxide using PREOS at 333.15K

$$1 = \text{Carbon Dioxide} \qquad T := 333.15K$$

$$2 = \text{AKD}$$

$$R := 8.314 \frac{J}{mol \cdot K} \qquad MPa := 10^6 Pa \qquad bar := 10^5 Pa$$

$$T_{c1} := 304.12K \qquad P_{c1} := 73.74 bar \qquad \omega_1 := 0.225$$

$$T_{c2} := 900.95K \qquad P_{c2} := 7.54 bar \qquad \omega_2 := 1.91$$

$$P1_{sat} := \frac{\left[10^3 \cdot \exp\left[8.5759 - \frac{95.5979(100K)}{T} - 3.744\ln\left(\frac{T}{100K}\right) - 0.5834\frac{T}{100K}\right]\right]Pa}{504} \rightarrow 5.7415906010855907017e-12 \cdot Pa$$

$$k1 := 0.378893 + 1.4897153\omega_1 - 0.26992\omega_1^2$$

$$a_1 := \frac{0.457235 R^2 \cdot T_{c1}^2}{P_{c1}} \cdot \left[1 + k1 \cdot \left[1 - \left(\frac{T}{T_{c1}}\right)^{0.5}\right]\right]^2 \qquad b_1 := \frac{0.077796 R \cdot T_{c1}}{P_{c1}}$$

$$k2 := 0.378893 + 1.4897153\omega_2 - 0.26992\omega_2^2$$

$$a_2 := \frac{0.457235 R^2 \cdot T_{c2}^2}{P_{c2}} \cdot \left[1 + k2 \cdot \left[1 - \left(\frac{T}{T_{c2}}\right)^{0.5}\right]\right]^2 \qquad b_2 := \frac{0.077796 R \cdot T_{c2}}{P_{c2}}$$

$$a_{12}(k12) := \left(a_1 \cdot a_2\right)^{0.5} \cdot (1 - k12) \qquad b(y2) := (1 - y2) \cdot b_1 + y2 \cdot b_2$$

$$a(y2, k12) := (1 - y2)^2 \cdot a_1 + 2 \cdot (1 - y2) \cdot y2 \cdot a_{12}(k12) + y2^2 \cdot a_2$$

$$A(y2, k12, P) := \frac{a(y2, k12) \cdot P}{(R T)^2} \qquad B(y2, P) := \frac{b(y2) \cdot P}{R \cdot T}$$

$$Z(y2, k12, P) := \text{polyroots}\begin{pmatrix} -A(y2, k12, P) \cdot B(y2, P) + B(y2, P)^2 + B(y2, P)^3 \\ A(y2, k12, P) - 3 \cdot B(y2, P)^2 - 2 \cdot B(y2, P) \\ -1 + B(y2, P) \\ 1 \end{pmatrix}$$

$$Z(y2, k12, P) := \begin{vmatrix} Z1 \leftarrow Z(y2, k12, P) \\ \text{for } i \in 0..2 \\ \quad Z1_i \leftarrow 0 \text{ if } Im(Z1_i) \neq 0 \\ Z1 \leftarrow sort(Z1) \\ Z1_0 \leftarrow Z1_2 \text{ if } |Z1_0| < 10^{-5} \\ Z1_2 \leftarrow Z1_0 \text{ if } |Z1_2| < 10^{-5} \\ Z1 \end{vmatrix}$$

set complex roots to zero

sort the roots

set values of any complex root

to the value of the real root

$$Z(y2, k12, P) := Z(y2, k12, P)_2$$

$$Vvap(y2, k12, P) := \frac{Z(y2, k12, P) \cdot R \cdot T}{P}$$

$$\phi(y2, k12, P) := exp\left[\frac{b_2}{b(y2)} \cdot (Z(y2, k12, P) - 1) - \ln(Z(y2, k12, P) - B(y2, P)) \ldots \right.$$
$$\left. + \frac{-a(y2, k12)}{2 \cdot \sqrt{2} \cdot b(y2) \cdot R \cdot T} \cdot \left[\left[\frac{2 \cdot \left[(1 - y2) \cdot a_{12}(k12) + y2 \cdot a_2 \right]}{a(y2, k12)} - \frac{b_2}{b(y2)} \right] \cdot \ln\left[\frac{Vvap(y2, k12, P) + \left(1 + \sqrt{2}\right) \cdot b(y2)}{Vvap(y2, k12, P) + \left(1 - \sqrt{2}\right) \cdot b(y2)} \right] \right] \right]$$

$$i := 0..3$$

$$P0_i :=$$

$$v1_s := 656.3 \cdot 10^{-6} \frac{m^3}{mol} \qquad \text{Guess}$$

$$y0_i :=$$

$$k12 := 0.01$$

98.69atm
148.035atm
197.38atm
246.332atm

0.00012
0.0022
0.0037
0.0064

Given

$$\sum_{i=0}^{3} \left[\frac{P1_{sat}}{P0_i} \cdot \frac{1}{\phi\left(y0_i, k12, P0_i\right)} \cdot exp\left[\frac{v1_s \cdot \left(P0_i - P1_{sat}\right)}{R \cdot T} \right] - y0_i \right]^2 = 0 \qquad k12 := Find(k12)$$

$$k12 = -0.12633 \qquad k_{12} := k12$$

$$R := 8.314 \frac{J}{mol \cdot K}$$

$$\text{MPa} := 10^6 \, \text{Pa}$$

$$k1(T) := 0.378893 + 1.4897153\omega_1 - 0.26992\omega_1^2$$

$$a_1(T) := \frac{0.457235 R^2 \cdot T_{c1}^2}{P_{c1}} \cdot \left[1 + k1(T) \cdot \left[1 - \left(\frac{T}{T_{c1}} \right)^{0.5} \right] \right]^2 \qquad b_1 := \frac{0.077796 R \cdot T_{c1}}{P_{c1}}$$

$$k2(T) := 0.378893 + 1.4897153\omega_2 - 0.26992\omega_2^2$$

$$a_2(T) := \frac{0.457235 R^2 \cdot T_{c2}^2}{P_{c2}} \cdot \left[1 + k2(T) \cdot \left[1 - \left(\frac{T}{T_{c2}} \right)^{0.5} \right] \right]^2 \qquad b_2 := \frac{0.077796 R \cdot T_{c2}}{P_{c2}}$$

$$a_{12}(T) := \left(a_1(T) \cdot a_2(T) \right)^{0.5} \cdot \left(1 - k_{12} \right)$$

$$a(y2,T) := (1 - y2)^2 \cdot a_1(T) + 2 \cdot (1 - y2) \cdot y2 \cdot a_{12}(T) + y2^2 \cdot a_2(T)$$

$$b(y2) := (1 - y2) \cdot b_1 + y2 \cdot b_2 \qquad B(y2,P,T) := \frac{b(y2) \cdot P}{R \cdot T} \qquad A(y2,P,T) := \frac{a(y2,T) \cdot P}{(R\,T)^2}$$

$$Z(y2,P,T) := \text{polyroots} \begin{pmatrix} -A(y2,P,T) \cdot B(y2,P,T) + B(y2,P,T)^2 + B(y2,P,T)^3 \\ A(y2,P,T) - 3 \cdot B(y2,P,T)^2 - 2 \cdot B(y2,P,T) \\ -1 + B(y2,P,T) \\ 1 \end{pmatrix}$$

$$Z(y2,P,T) := \begin{vmatrix} Z1 \leftarrow Z(y2,P,T) \\ \text{for } i \in 0..2 \\ \quad Z1_i \leftarrow 0 \text{ if } \text{Im}\left(Z1_i\right) \neq 0 & \text{set complex roots to zero} \\ Z1 \leftarrow \text{sort}(Z1) & \text{sort the roots} \\ Z1_0 \leftarrow Z1_2 \text{ if } \left| Z1_0 \right| < 10^{-5} & \text{set values of any complex root} \\ Z1_2 \leftarrow Z1_0 \text{ if } \left| Z1_2 \right| < 10^{-5} & \text{to the value of the real root} \\ Z1 \end{vmatrix}$$

$$\underset{\sim}{Z}(y2,P,T) := Z(y2,P,T)_2$$

$$\underset{\sim}{Vvap}(y2,P,T) := \frac{Z(y2,P,T) \cdot R \cdot T}{P}$$

$$\underset{\sim}{\phi}(y2,P,T) := \exp\left[\frac{b_2}{b(y2)} \cdot (Z(y2,P,T) - 1) - \ln(Z(y2,P,T) - B(y2,P,T)) \ldots \right.$$
$$\left. + \frac{-a(y2,T)}{2 \cdot \sqrt{2} \cdot b(y2) \cdot R \cdot T} \cdot \left[\left[\frac{2 \cdot \left[(1-y2) \cdot a_{12}(T) + y2 \cdot a_2(T)\right]}{a(y2,T)} - \frac{b_2}{b(y2)}\right] \cdot \ln\left[\frac{Vvap(y2,P,T) + \left(1+\sqrt{2}\right) \cdot b(y2)}{Vvap(y2,P,T) + \left(1-\sqrt{2}\right) \cdot b(y2)}\right]\right]\right]$$

$P := 1MPa, 2MPa .. 30MPa$ $\qquad \underset{\sim}{y} := 0.01$

Given

$$y = \frac{P1_{sat}}{P} \cdot \frac{1}{\phi(y,P,T)} \cdot \exp\left[\frac{v1_s \cdot (P - P1_{sat})}{R \cdot T}\right]$$

$$\underset{\sim}{F}(y,P,T) := Find(y)$$

$$i := 0..30$$

$$y1_i :=$$

0.00012
0.0022
0.0037
0.0064

$$P1_i :=$$

98.69
148.035
197.38
246.725

$$F(y,P,T) =$$

0
0
0
$4.388 \cdot 10^{-15}$
$3.264 \cdot 10^{-14}$
$2.863 \cdot 10^{-13}$
$2.994 \cdot 10^{-12}$
$3.808 \cdot 10^{-11}$
$5.964 \cdot 10^{-10}$
$1.115 \cdot 10^{-8}$
$2.117 \cdot 10^{-7}$
$2.951 \cdot 10^{-6}$
$2.373 \cdot 10^{-5}$
$1.144 \cdot 10^{-4}$
$3.849 \cdot 10^{-4}$
...

$$F(y,P,T)$$
$$y1_i$$
$$\frac{P}{10^5}, P1_i$$

149

3. Solubilities of AKD in supercritical carbon dioxide using PREOS at 353.15K

$$1 = \text{Carbon Dioxide}$$
$$T := 353.15 K$$
$$2 = \text{AKD}$$

$$R := 8.314 \frac{J}{mol \cdot K} \qquad MPa := 10^6 Pa \qquad bar := 10^5 Pa$$

$$T_{c1} := 304.11 K \qquad P_{c1} := 73.74 bar \qquad \omega_1 := 0.225$$

$$T_{c2} := 900.95 K \qquad P_{c2} := 7.54 bar \qquad \omega_2 := 1.91$$

$$P1_{sat} := \frac{\left[10^3 \cdot \exp\left[8.5759 - \frac{95.5979(100K)}{T} - 3.744 \ln\left(\frac{T}{100K}\right) - 0.5834 \frac{T}{100K}\right]\right] Pa}{504} \rightarrow 2.0860929004004097295e\text{-}Pa$$

$$k1 := 0.378893 + 1.4897153\omega_1 - 0.26992\omega_1^2$$

$$a_1 := \frac{0.457235 R^2 \cdot T_{c1}^2}{P_{c1}} \cdot \left[1 + k1 \cdot \left[1 - \left(\frac{T}{T_{c1}}\right)^{0.5}\right]\right]^2 \qquad b_1 := \frac{0.077796 R \cdot T_{c1}}{P_{c1}}$$

$$k2 := 0.378893 + 1.4897153\omega_2 - 0.26992\omega_2^2$$

$$a_2 := \frac{0.457235 R^2 \cdot T_{c2}^2}{P_{c2}} \cdot \left[1 + k2 \cdot \left[1 - \left(\frac{T}{T_{c2}}\right)^{0.5}\right]\right]^2 \qquad b_2 := \frac{0.077796 R \cdot T_{c2}}{P_{c2}}$$

$$a_{12}(k12) := (a_1 \cdot a_2)^{0.5} \cdot (1 - k12) \qquad b(y2) := (1 - y2) \cdot b_1 + y2 \cdot b_2$$

$$a(y2, k12) := (1 - y2)^2 \cdot a_1 + 2 \cdot (1 - y2) \cdot y2 \cdot a_{12}(k12) + y2^2 \cdot a_2$$

$$A(y2, k12, P) := \frac{a(y2, k12) \cdot P}{(R T)^2} \qquad B(y2, P) := \frac{b(y2) \cdot P}{R \cdot T}$$

$$Z(y2, k12, P) := \text{polyroots} \begin{pmatrix} -A(y2, k12, P) \cdot B(y2, P) + B(y2, P)^2 + B(y2, P)^3 \\ A(y2, k12, P) - 3 \cdot B(y2, P)^2 - 2 \cdot B(y2, P) \\ -1 + B(y2, P) \\ 1 \end{pmatrix}$$

150

$$\underset{\sim}{Z}(y2, k12, P) := \begin{vmatrix} Z1 \leftarrow Z(y2, k12, P) \\ \text{for } i \in 0..2 \\ \quad Z1_i \leftarrow 0 \text{ if } \text{Im}(Z1_i) \neq 0 \\ Z1 \leftarrow \text{sort}(Z1) \\ Z1_0 \leftarrow Z1_2 \text{ if } |Z1_0| < 10^{-5} \\ Z1_2 \leftarrow Z1_0 \text{ if } |Z1_2| < 10^{-5} \\ Z1 \end{vmatrix}$$

set complex roots to zero

sort the roots

set values of any complex root

to the value of the real root

$$\underset{\sim}{Z}(y2, k12, P) := Z(y2, k12, P)_2$$

$$\underset{\sim}{Vvap}(y2, k12, P) := \frac{Z(y2, k12, P) \cdot R \cdot T}{P}$$

$$\underset{\sim}{\phi}(y2, k12, P) := \exp\left[\frac{b_2}{b(y2)} \cdot (Z(y2, k12, P) - 1) - \ln(Z(y2, k12, P) - B(y2, P)) \ldots \right. \\ \left. + \frac{-a(y2, k12)}{2 \cdot \sqrt{2} \cdot b(y2) \cdot R \cdot T} \cdot \left[\left[\frac{2 \cdot [(1 - y2) \cdot a_{12}(k12) + y2 \cdot a_2]}{a(y2, k12)}\right] - \frac{b_2}{b(y2)}\right] \cdot \ln\left[\frac{Vvap(y2, k12, P) + (1 + \sqrt{2}) \cdot b(y2)}{Vvap(y2, k12, P) + (1 - \sqrt{2}) \cdot b(y2)}\right]\right]$$

$$i := 0..3$$

$$\underset{\sim}{v1}_s := 656.3 10^{-6} \frac{m^3}{mol}$$

Guess

$$P0_i :=$$

98.69atm
148.035atm
197.38atm
246.332atm

$$y0_i :=$$

0.00012
0.0022
0.0037
0.0064

Given

$$k12 := 0.01$$

$$\sum_{i=0}^{3} \left[\frac{P1_{sat}}{P0_i} \cdot \frac{1}{\phi(y0_i, k12, P0_i)} \cdot \exp\left[\frac{v1_s \cdot (P0_i - P1_{sat})}{R \cdot T}\right] - y0_i\right]^2 = 0$$

$$\underset{\sim}{k12} := \text{Find}(k12)$$

$$\underset{\sim}{k12} := k12 \qquad \boxed{k12 = -0.20893}$$

151

$$R := 8.314 \frac{J}{mol \cdot K}$$

$$MPa := 10^6 Pa$$

$$k1(T) := 0.378893 + 1.4897153\omega_1 - 0.26992\omega_1^2$$

$$a_1(T) := \frac{0.457235 R^2 \cdot T_{c1}^2}{P_{c1}} \cdot \left[1 + k1(T) \cdot \left[1 - \left(\frac{T}{T_{c1}}\right)^{0.5}\right]\right]^2 \qquad b_1 := \frac{0.077796 R \cdot T_{c1}}{P_{c1}}$$

$$k2(T) := 0.378893 + 1.4897153\omega_2 - 0.26992\omega_2^2$$

$$a_2(T) := \frac{0.457235 R^2 \cdot T_{c2}^2}{P_{c2}} \cdot \left[1 + k2(T) \cdot \left[1 - \left(\frac{T}{T_{c2}}\right)^{0.5}\right]\right]^2 \qquad b_2 := \frac{0.077796 R \cdot T_{c2}}{P_{c2}}$$

$$a_{12}(T) := \left(a_1(T) \cdot a_2(T)\right)^{0.5} \cdot \left(1 - k_{12}\right)$$

$$a(y2, T) := (1 - y2)^2 \cdot a_1(T) + 2 \cdot (1 - y2) \cdot y2 \cdot a_{12}(T) + y2^2 \cdot a_2(T)$$

$$b(y2) := (1 - y2) \cdot b_1 + y2 \cdot b_2 \qquad B(y2, P, T) := \frac{b(y2) \cdot P}{R \cdot T} \qquad A(y2, P, T) := \frac{a(y2, T) \cdot P}{(R T)^2}$$

$$Z(y2, P, T) := \text{polyroots} \begin{pmatrix} -A(y2, P, T) \cdot B(y2, P, T) + B(y2, P, T)^2 + B(y2, P, T)^3 \\ A(y2, P, T) - 3 \cdot B(y2, P, T)^2 - 2 \cdot B(y2, P, T) \\ -1 + B(y2, P, T) \\ 1 \end{pmatrix}$$

$$Z(y2, P, T) := \begin{vmatrix} Z1 \leftarrow Z(y2, P, T) \\ \text{for } i \in 0..2 \\ \quad Z1_i \leftarrow 0 \text{ if } Im(Z1_i) \neq 0 \qquad\qquad \text{set complex roots to zero} \\ Z1 \leftarrow \text{sort}(Z1) \qquad\qquad \text{sort the roots} \\ Z1_0 \leftarrow Z1_2 \text{ if } |Z1_0| < 10^{-5} \qquad \text{set values of any complex root} \\ Z1_2 \leftarrow Z1_0 \text{ if } |Z1_2| < 10^{-5} \qquad \text{to the value of the real root} \\ Z1 \end{vmatrix}$$

$$Z(y2, P, T) := Z(y2, P, T)_2$$

$$Vvap(y2, P, T) := \frac{Z(y2, P, T) \cdot R \cdot T}{P}$$

$$\phi(y2, P, T) := \exp\left[\frac{b_2}{b(y2)} \cdot (Z(y2, P, T) - 1) - \ln(Z(y2, P, T) - B(y2, P, T)) \dots \right.$$
$$\left. + \frac{-a(y2, T)}{2 \cdot \sqrt{2} \cdot b(y2) \cdot R \cdot T} \cdot \left[\left[\frac{2 \cdot [(1 - y2) \cdot a_{12}(T) + y2 \cdot a_2(T)]}{a(y2, T)} - \frac{b_2}{b(y2)} \right] \cdot \ln\left[\frac{Vvap(y2, P, T) + (1 + \sqrt{2}) \cdot b(y2)}{Vvap(y2, P, T) + (1 - \sqrt{2}) \cdot b(y2)} \right] \right] \right]$$

$$P := 1MPa, 2MPa .. 30MPa \qquad\qquad y := 0.01$$

Given

$$y = \frac{P1_{sat}}{P} \cdot \frac{1}{\phi(y, P, T)} \cdot \exp\left[\frac{v1_s \cdot (P - P1_{sat})}{R \cdot T} \right]$$

$$F(y, P, T) := Find(y)$$

$$i := 0 .. 30$$

$y1_i :=$

0.00012
0.0022
0.0037
0.0064

$F(y, P, T) =$

0
0
$1.402 \cdot 10^{-15}$
$6.739 \cdot 10^{-15}$
$3.631 \cdot 10^{-14}$
$2.147 \cdot 10^{-13}$
$1.378 \cdot 10^{-12}$
$9.512 \cdot 10^{-12}$
$6.978 \cdot 10^{-11}$
$5.34 \cdot 10^{-10}$
$4.136 \cdot 10^{-9}$
$3.099 \cdot 10^{-8}$
$2.122 \cdot 10^{-7}$
$1.254 \cdot 10^{-6}$
$6.141 \cdot 10^{-6}$
...

$P1_i :=$

98.69
148.035
197.38
246.725

F(y, P, T)
y1_i

$\frac{P}{10^5}, P1_i$

153
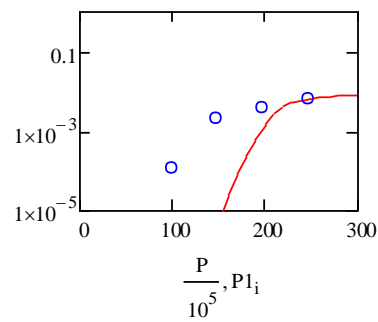
Modeling of cloud-point pressure solubility determination of method

1. Solubilities of AKD in supercritical carbon dioxide based on PREOS at 323.15K

$$1 = \text{Carbon Dioxide}$$
$$T := 323.15 K$$

$$2 = \text{AKD}$$

$$R := 8.314 \frac{J}{mol \cdot K} \qquad MPa := 10^6 Pa \qquad bar := 10^5 Pa$$

$$T_{c1} := 304.11 K \qquad P_{c1} := 73.74 bar \qquad \omega_1 := 0.225$$

$$T_{c2} := 900.95 K \qquad P_{c2} := 7.54 bar \qquad \omega_2 := 1.91$$

$$P1_{sat} := \frac{\left(10^3 \cdot \exp\left(8.5759 - \frac{95.5979}{\frac{T}{100 \cdot K}} - 3.744 \ln\left(\frac{T}{100K}\right) - 0.5834 \frac{T}{100K}\right)\right) Pa}{504} \rightarrow 2.8072260973058480705e\text{-}2 \, Pa$$

$$k1 := 0.378893 + 1.4897153 \omega_1 - 0.26992 \omega_1^2$$

$$a_1 := \frac{0.457235 R^2 \cdot T_{c1}^2}{P_{c1}} \cdot \left[1 + k1 \cdot \left[1 - \left(\frac{T}{T_{c1}}\right)^{0.5}\right]\right]^2 \qquad b_1 := \frac{0.077796 R \cdot T_{c1}}{P_{c1}}$$

$$k2 := 0.378893 + 1.4897153 \omega_2 - 0.26992 \omega_2^2$$

$$a_2 := \frac{0.457235 R^2 \cdot T_{c2}^2}{P_{c2}} \cdot \left[1 + k2 \cdot \left[1 - \left(\frac{T}{T_{c2}}\right)^{0.5}\right]\right]^2 \qquad b_2 := \frac{0.077796 R \cdot T_{c2}}{P_{c2}}$$

$$a_{12}(k12) := \left(a_1 \cdot a_2\right)^{0.5} \cdot (1 - k12)$$

$$a(y2, k12) := (1 - y2)^2 \cdot a_1 + 2 \cdot (1 - y2) \cdot y2 \cdot a_{12}(k12) + y2^2 \cdot a_2 \qquad b(y2) := (1 - y2) \cdot b_1 + y2 \cdot b_2$$

154

$$A(y2, k12, P) := \frac{a(y2, k12) \cdot P}{(R\,T)^2} \qquad\qquad B(y2, P) := \frac{b(y2) \cdot P}{R \cdot T}$$

$$Z(y2, k12, P) := \text{polyroots} \begin{pmatrix} -A(y2, k12, P) \cdot B(y2, P) + B(y2, P)^2 + B(y2, P)^3 \\ A(y2, k12, P) - 3 \cdot B(y2, P)^2 - 2 \cdot B(y2, P) \\ -1 + B(y2, P) \\ 1 \end{pmatrix}$$

$$Z(y2, k12, P) := \begin{vmatrix} Z1 \leftarrow Z(y2, k12, P) \\ \text{for } i \in 0..2 \\ \quad Z1_i \leftarrow 0 \text{ if } \text{Im}(Z1_i) \neq 0 \\ Z1 \leftarrow \text{sort}(Z1) \\ Z1_0 \leftarrow Z1_2 \text{ if } |Z1_0| < 10^{-5} \\ Z1_2 \leftarrow Z1_0 \text{ if } |Z1_2| < 10^{-5} \\ Z1 \end{vmatrix}$$

set complex roots to zero

sort the roots

set values of any complex root

to the value of the real root

$$Z(y2, k12, P) := Z(y2, k12, P)_2$$

$$Vvap(y2, k12, P) := \frac{Z(y2, k12, P) \cdot R \cdot T}{P}$$

$$\phi(y2, k12, P) := \exp\left[\frac{b_2}{b(y2)} \cdot (Z(y2, k12, P) - 1) - \ln(Z(y2, k12, P) - B(y2, P)) \ldots \\ + \frac{-a(y2, k12)}{2 \cdot \sqrt{2} \cdot b(y2) \cdot R \cdot T} \cdot \left[\left[\frac{2 \cdot [(1 - y2) \cdot a_{12}(k12) + y2 \cdot a_2]}{a(y2, k12)} - \frac{b_2}{b(y2)} \right] \cdot \ln\left[\frac{Vvap(y2, k12, P) + (1 + \sqrt{2}) \cdot b(y2)}{Vvap(y2, k12, P) + (1 - \sqrt{2}) \cdot b(y2)} \right] \right] \right]$$

$$i := 0..5 \qquad\qquad v1_s := 656.3 \cdot 10^{-6} \frac{m^3}{mol}$$

Guess

$$P0_i :=$$

$$y0_i :=$$

$$k12 := 0.01$$

108.559atm
167.773atm
207.249atm
226.987atm
246.725atm

0.0009
0.0017
0.0032
0.0027
0.0048

Given

$$\sum_{i=0}^{4} \left[\frac{P1_{sat}}{P0_i} \cdot \frac{1}{\phi(y0_i, k12, P0_i)} \cdot \exp\left[\frac{v1_s \cdot (P0_i - P1_{sat})}{R \cdot T} \right] - y0_i \right]^2 = 0$$

$$k12 := \text{Find}(k12)$$

$$k12 = -0.08134$$

$$k_{12} := k12$$

$$R := 8.314 \frac{J}{mol \cdot K} \qquad MPa := 10^6 Pa$$

$$k1(T) := 0.378893 + 1.4897153\omega_1 - 0.26992\omega_1^2$$

$$a_1(T) := \frac{0.457235 R^2 \cdot T_{c1}^2}{P_{c1}} \cdot \left[1 + k1(T) \cdot \left[1 - \left(\frac{T}{T_{c1}}\right)^{0.5}\right]\right]^2 \qquad b_1 := \frac{0.077796 R \cdot T_{c1}}{P_{c1}}$$

$$k2(T) := 0.378893 + 1.4897153\omega_2 - 0.26992\omega_2^2$$

$$a_2(T) := \frac{0.457235 R^2 \cdot T_{c2}^2}{P_{c2}} \cdot \left[1 + k2(T) \cdot \left[1 - \left(\frac{T}{T_{c2}}\right)^{0.5}\right]\right]^2 \qquad b_2 := \frac{0.077796 R \cdot T_{c2}}{P_{c2}}$$

$$a_{12}(T) := \left(a_1(T) \cdot a_2(T)\right)^{0.5} \cdot \left(1 - k_{12}\right)$$

$$a(y2, T) := (1 - y2)^2 \cdot a_1(T) + 2 \cdot (1 - y2) \cdot y2 \cdot a_{12}(T) + y2^2 \cdot a_2(T)$$

$$b(y2) := (1 - y2) \cdot b_1 + y2 \cdot b_2$$

$$A(y2, P, T) := \frac{a(y2, T) \cdot P}{(R T)^2} \qquad B(y2, P, T) := \frac{b(y2) \cdot P}{R \cdot T}$$

$$Z(y2, P, T) := \text{polyroots} \begin{pmatrix} -A(y2,P,T) \cdot B(y2,P,T) + B(y2,P,T)^2 + B(y2,P,T)^3 \\ A(y2,P,T) - 3 \cdot B(y2,P,T)^2 - 2 \cdot B(y2,P,T) \\ -1 + B(y2,P,T) \\ 1 \end{pmatrix}$$

$$Z(y2, P, T) := \begin{vmatrix} Z1 \leftarrow Z(y2,P,T) \\ \text{for } i \in 0..2 \\ \quad Z1_i \leftarrow 0 \text{ if } \text{Im}\left(Z1_i\right) \neq 0 \\ Z1 \leftarrow \text{sort}(Z1) \\ Z1_0 \leftarrow Z1_2 \text{ if } \left|Z1_0\right| < 10^{-5} \\ Z1_2 \leftarrow Z1_0 \text{ if } \left|Z1_2\right| < 10^{-5} \\ Z1 \end{vmatrix} \qquad \text{set complex roots to zero}$$

sort the roots

set values of any complex root

to the value of the real root

$$Z(y2, P, T) := Z(y2, P, T)_2$$

$$Vvap(y2, P, T) := \frac{Z(y2, P, T) \cdot R \cdot T}{P}$$

$$\phi(y2, P, T) := \exp\left[\frac{b_2}{b(y2)} \cdot (Z(y2, P, T) - 1) - \ln(Z(y2, P, T) - B(y2, P, T)) \dots \right. $$
$$\left. + \frac{-a(y2, T)}{2 \cdot \sqrt{2} \cdot b(y2) \cdot R \cdot T} \cdot \left[\left[\frac{2 \cdot \left[(1 - y2) \cdot a_{12}(T) + y2 \cdot a_2(T)\right]}{a(y2, T)} - \frac{b_2}{b(y2)}\right] \cdot \ln\left[\frac{Vvap(y2, P, T) + \left(1 + \sqrt{2}\right) \cdot b(y2)}{Vvap(y2, P, T) + \left(1 - \sqrt{2}\right) \cdot b(y2)}\right]\right]\right]$$

$$P := 1MPa, 2MPa .. 30MPa \qquad y := 0.01$$

Given

$$y = \frac{P1_{sat}}{P} \cdot \frac{1}{\phi(y, P, T)} \cdot \exp\left[\frac{v1_s \cdot \left(P - P1_{sat}\right)}{R \cdot T}\right]$$

$$F(y, P, T) =$$

0
$1.005 \cdot 10^{-15}$
$7.809 \cdot 10^{-15}$
$7.921 \cdot 10^{-14}$
$1.035 \cdot 10^{-12}$
$9.597 \cdot 10^{-3}$
$7.429 \cdot 10^{-3}$
$5.277 \cdot 10^{-3}$
$1.513 \cdot 10^{-6}$
$2.799 \cdot 10^{-4}$
0.047
0.047
0.046
0.046
0.046
...

$$i := 0 .. 30$$

$$y1_i :=$$

0.0009
0.0017
0.0032
0.0027
0.0048

$$F(y, P, T) := Find(y)$$

$$P1_i :=$$

108.551
167.773
207.249
226.987
246.725

157
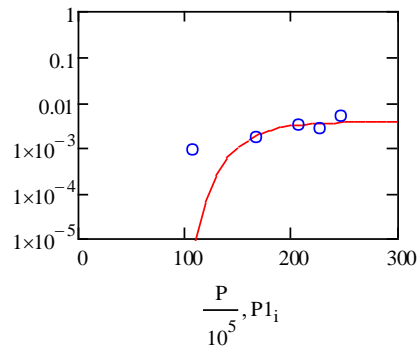
2. Solubilities of AKD in supercritical carbon dioxide based on PREOS at 333.15K

$$1 = \text{Carbon Dioxide} \qquad T := 333.15 K$$

$$2 = \text{AKD}$$

$$R := 8.314 \frac{J}{mol \cdot K} \qquad MPa := 10^6 Pa \qquad bar := 10^5 Pa$$

$$T_{c1} := 304.1 K \qquad P_{c1} := 73.74 bar \qquad \omega_1 := 0.225$$

$$T_{c2} := 900.95 K \qquad P_{c2} := 7.54 bar \qquad \omega_2 := 1.91$$

$$P1_{sat} := \frac{\left(10^3 \cdot \exp\left(8.5759 - \frac{95.5979}{\frac{T}{100 \cdot K}} - 3.744 \ln\left(\frac{T}{100K}\right) - 0.5834 \frac{T}{100K}\right)\right) Pa}{504} \rightarrow 5.7415906010855907017e-1 Pa$$

$$k1 := 0.378893 + 1.4897153 \omega_1 - 0.26992 \omega_1^2$$

$$a1 := \frac{0.457235 R^2 \cdot T_{c1}^2}{P_{c1}} \cdot \left[1 + k1 \cdot \left[1 - \left(\frac{T}{T_{c1}}\right)^{0.5}\right]\right]^2 \qquad b1 := \frac{0.077796 R \cdot T_{c1}}{P_{c1}}$$

$$k2 := 0.378893 + 1.4897153 \omega_2 - 0.26992 \omega_2^2$$

$$a2 := \frac{0.457235 R^2 \cdot T_{c2}^2}{P_{c2}} \cdot \left[1 + k2 \cdot \left[1 - \left(\frac{T}{T_{c2}}\right)^{0.5}\right]\right]^2 \qquad b2 := \frac{0.077796 R \cdot T_{c2}}{P_{c2}}$$

$$a_{12}(k12) := \left(a_1 \cdot a_2\right)^{0.5} \cdot (1 - k12)$$

$$a(y2, k12) := (1 - y2)^2 \cdot a_1 + 2 \cdot (1 - y2) \cdot y2 \cdot a_{12}(k12) + y2^2 \cdot a_2$$

$$b(y2) := (1 - y2) \cdot b_1 + y2 \cdot b_2$$

$$A(y2, k12, P) := \frac{a(y2, k12) \cdot P}{(R T)^2} \qquad B(y2, P) := \frac{b(y2) \cdot P}{R \cdot T}$$

$$Z(y2,k12,P) := \text{polyroots} \begin{pmatrix} -A(y2,k12,P) \cdot B(y2,P) + B(y2,P)^2 + B(y2,P)^3 \\ A(y2,k12,P) - 3 \cdot B(y2,P)^2 - 2 \cdot B(y2,P) \\ -1 + B(y2,P) \\ 1 \end{pmatrix}$$

$$Z(y2,k12,P) := \begin{vmatrix} Z1 \leftarrow Z(y2,k12,P) \\ \text{for } i \in 0..2 \\ \quad Z1_i \leftarrow 0 \text{ if } \text{Im}(Z1_i) \neq 0 \qquad \text{set complex roots to zero} \\ Z1 \leftarrow \text{sort}(Z1) \qquad\qquad \text{sort the roots} \\ Z1_0 \leftarrow Z1_2 \text{ if } |Z1_0| < 10^{-5} \qquad \text{set values of any complex root} \\ Z1_2 \leftarrow Z1_0 \text{ if } |Z1_2| < 10^{-5} \qquad \text{to the value of the real root} \\ Z1 \end{vmatrix}$$

$$Z(y2,k12,P) := Z(y2,k12,P)_2$$

$$Vvap(y2,k12,P) := \frac{Z(y2,k12,P) \cdot R \cdot T}{P}$$

$$\phi(y2,k12,P) := \exp\left[\frac{b_2}{b(y2)} \cdot (Z(y2,k12,P) - 1) - \ln(Z(y2,k12,P) - B(y2,P)) \dots \right.$$
$$\left. + \frac{-a(y2,k12)}{2 \cdot \sqrt{2} \cdot b(y2) \cdot R \cdot T} \cdot \left[\left[\frac{2 \cdot [(1 - y2) \cdot a_{12}(k12) + y2 \cdot a_2]}{a(y2,k12)} - \frac{b_2}{b(y2)}\right] \cdot \ln\left[\frac{Vvap(y2,k12,P) + (1 + \sqrt{2}) \cdot b(y2)}{Vvap(y2,k12,P) + (1 - \sqrt{2}) \cdot b(y2)}\right]\right]\right]$$

$$i := 0..4$$

Guess

$$v1_s := 656.3 \cdot 10^{-6} \frac{m^3}{mol}$$

$$P0_i :=$$

118.42atm
207.249atm
217.118atm
226.987atm
246.725atm

$$y0_i :=$$

0.0009
0.0017
0.0032
0.0027
0.0048

$$k12 := -0.01$$

Given

$$\sum_{i=0}^{4} \left[\frac{P1_{sat}}{P0_i} \cdot \frac{1}{\phi(y0_i, k12, P0_i)} \cdot \exp\left[\frac{v1_s \cdot (P0_i - P1_{sat})}{R \cdot T}\right] - y0_i\right]^2 = 0$$

$$R := 8.314 \frac{J}{\text{mol} \cdot K} \qquad\qquad MPa := 10^6 \, Pa \qquad\qquad k_{12} := k12$$

$$k1(T) := 0.378893 + 1.4897153\omega_1 - 0.26992\omega_1^2$$

$$a_1(T) := \frac{0.457235 R^2 \cdot T_{c1}^2}{P_{c1}} \cdot \left[1 + k1(T) \cdot \left[1 - \left(\frac{T}{T_{c1}} \right)^{0.5} \right] \right]^2 \qquad b_1 := \frac{0.077796 R \cdot T_{c1}}{P_{c1}}$$

$$k2(T) := 0.378893 + 1.4897153\omega_2 - 0.26992\omega_2^2$$

$$a_2(T) := \frac{0.457235 R^2 \cdot T_{c2}^2}{P_{c2}} \cdot \left[1 + k2(T) \cdot \left[1 - \left(\frac{T}{T_{c2}} \right)^{0.5} \right] \right]^2 \qquad b_2 := \frac{0.077796 R \cdot T_{c2}}{P_{c2}}$$

$$a_{12}(T) := \left(a_1(T) \cdot a_2(T) \right)^{0.5} \cdot \left(1 - k_{12} \right)$$

$$a(y2, T) := (1 - y2)^2 \cdot a_1(T) + 2 \cdot (1 - y2) \cdot y2 \cdot a_{12}(T) + y2^2 \cdot a_2(T)$$

$$b(y2) := (1 - y2) \cdot b_1 + y2 \cdot b_2$$

$$A(y2, P, T) := \frac{a(y2, T) \cdot P}{(R\,T)^2} \qquad\qquad B(y2, P, T) := \frac{b(y2) \cdot P}{R \cdot T}$$

$$Z(y2, P, T) := \text{polyroots} \begin{pmatrix} -A(y2, P, T) \cdot B(y2, P, T) + B(y2, P, T)^2 + B(y2, P, T)^3 \\ A(y2, P, T) - 3 \cdot B(y2, P, T)^2 - 2 \cdot B(y2, P, T) \\ -1 + B(y2, P, T) \\ 1 \end{pmatrix}$$

$$Z(y2, P, T) := \begin{vmatrix} Z1 \leftarrow Z(y2, P, T) \\ \text{for } i \in 0..2 \\ \quad Z1_i \leftarrow 0 \text{ if } \text{Im}(Z1_i) \neq 0 \\ Z1 \leftarrow \text{sort}(Z1) \\ Z1_0 \leftarrow Z1_2 \text{ if } |Z1_0| < 10^{-5} \\ Z1_2 \leftarrow Z1_0 \text{ if } |Z1_2| < 10^{-5} \\ Z1 \end{vmatrix}$$

set complex roots to zero

sort the roots

set values of any complex root

to the value of the real root

$$\underset{\sim}{Z}(y2,P,T) := Z(y2,P,T)_2$$

$$\underset{\sim}{Vvap}(y2,P,T) := \frac{Z(y2,P,T) \cdot R \cdot T}{P}$$

$$\underset{\sim}{\phi}(y2,P,T) := \exp\left[\frac{b_2}{b(y2)} \cdot (Z(y2,P,T) - 1) - \ln(Z(y2,P,T) - B(y2,P,T)) \ldots \right.$$
$$\left. + \frac{-a(y2,T)}{2 \cdot \sqrt{2} \cdot b(y2) \cdot R \cdot T} \cdot \left[\left[\frac{2 \cdot \left[(1 - y2) \cdot a_{12}(T) + y2 \cdot a_2(T)\right]}{a(y2,T)} - \frac{b_2}{b(y2)}\right] \cdot \ln\left[\frac{Vvap(y2,P,T) + \left(1 + \sqrt{2}\right) \cdot b(y2)}{Vvap(y2,P,T) + \left(1 - \sqrt{2}\right) \cdot b(y2)}\right]\right]\right]$$

$$P := 1MPa, 2MPa .. 30MPa \qquad \underset{\sim}{y} := 0.01$$

Given

$$y = \frac{P1_{sat}}{P} \cdot \frac{1}{\phi(y,P,T)} \cdot \exp\left[\frac{v1_s \cdot \left(P - P1_{sat}\right)}{R \cdot T}\right]$$

$$\underset{\sim}{F}(y,P,T) := Find(y)$$

$$i := 0 .. 30$$

$y1_i :=$

0.0009
0.0017
0.0032
0.0027
0.0048

$P1_i :=$

108.551
167.773
207.249
226.987
246.725

$F(y,P,T) =$

0
0
0
$3.909 \cdot 10^{-15}$
$2.808 \cdot 10^{-14}$
$2.369 \cdot 10^{-13}$
$2.373 \cdot 10^{-12}$
$2.874 \cdot 10^{-11}$
$4.256 \cdot 10^{-10}$
$7.463 \cdot 10^{-9}$
$1.32 \cdot 10^{-7}$
$1.713 \cdot 10^{-6}$
$1.283 \cdot 10^{-5}$
$5.714 \cdot 10^{-5}$
$1.742 \cdot 10^{-4}$
...

$F(y,P,T)$
$y1_i$

$$\frac{P}{10^5}, P1_i$$
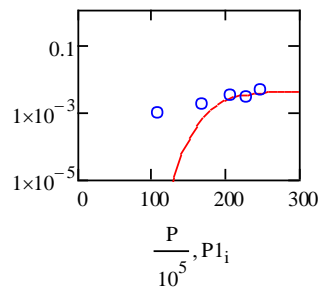
$$b(y2) := (1 - y2) \cdot b_1 + y2 \cdot b_2$$

3. Solubilities of AKD in supercritical carbon dioxide based on PREOS at 343.15K

$$1 = \text{Carbon Dioxide} \qquad T := 343.15 K$$

$$2 = \text{AKD}$$

$$R := 8.314 \frac{J}{mol \cdot K} \qquad MPa := 10^6 Pa \qquad bar := 10^5 Pa$$

$$T_{c1} := 304.12 K \qquad P_{c1} := 73.74 bar \qquad \omega_1 := 0.225$$

$$T_{c2} := 900.95 K \qquad P_{c2} := 7.54 bar \qquad \omega_2 := 1.91$$

$$P1_{sat} := \frac{\left(10^3 \cdot \exp\left(8.5759 - \frac{95.5979}{\frac{T}{100 \cdot K}} - 3.744 \ln\left(\frac{T}{100K}\right) - 0.5834 \frac{T}{100K}\right)\right) Pa}{504} \rightarrow 1.1188604227197116741 e - 1 Pa$$

$$k1 := 0.378893 + 1.4897153\omega_1 - 0.26992\omega_1^2$$

$$a_1 := \frac{0.457235 R^2 \cdot T_{c1}^2}{P_{c1}} \cdot \left[1 + k1 \cdot \left[1 - \left(\frac{T}{T_{c1}}\right)^{0.5}\right]\right]^2 \qquad b_1 := \frac{0.077796 R \cdot T_{c1}}{P_{c1}}$$

$$k2 := 0.378893 + 1.4897153\omega_2 - 0.26992\omega_2^2$$

$$a_2 := \frac{0.457235 R^2 \cdot T_{c2}^2}{P_{c2}} \cdot \left[1 + k2 \cdot \left[1 - \left(\frac{T}{T_{c2}}\right)^{0.5}\right]\right]^2 \qquad b_2 := \frac{0.077796 R \cdot T_{c2}}{P_{c2}}$$

$$a_{12}(k12) := \left(a_1 \cdot a_2\right)^{0.5} \cdot (1 - k12)$$

$$a(y2, k12) := (1 - y2)^2 \cdot a_1 + 2 \cdot (1 - y2) \cdot y2 \cdot a_{12}(k12) + y2^2 \cdot a_2$$

$$A(y2, k12, P) := \frac{a(y2, k12) \cdot P}{(R\,T)^2} \qquad\qquad B(y2, P) := \frac{b(y2) \cdot P}{R \cdot T}$$

$$Z(y2, k12, P) := \text{polyroots} \begin{pmatrix} -A(y2, k12, P) \cdot B(y2, P) + B(y2, P)^2 + B(y2, P)^3 \\ A(y2, k12, P) - 3 \cdot B(y2, P)^2 - 2 \cdot B(y2, P) \\ -1 + B(y2, P) \\ 1 \end{pmatrix}$$

$$Z(y2, k12, P) := \begin{vmatrix} Z1 \leftarrow Z(y2, k12, P) \\ \text{for } i \in 0..2 \\ \quad Z1_i \leftarrow 0 \text{ if } \text{Im}(Z1_i) \neq 0 \\ Z1 \leftarrow \text{sort}(Z1) \\ Z1_0 \leftarrow Z1_2 \text{ if } |Z1_0| < 10^{-5} \\ Z1_2 \leftarrow Z1_0 \text{ if } |Z1_2| < 10^{-5} \\ Z1 \end{vmatrix}$$

set complex roots to zero

sort the roots

set values of any complex root

to the value of the real root

$$Z(y2, k12, P) := Z(y2, k12, P)_2$$

$$Vvap(y2, k12, P) := \frac{Z(y2, k12, P) \cdot R \cdot T}{P}$$

$$\phi(y2, k12, P) := \exp\left[\frac{b_2}{b(y2)} \cdot (Z(y2, k12, P) - 1) - \ln(Z(y2, k12, P) - B(y2, P)) \dots \right.$$
$$\left. + \frac{-a(y2, k12)}{2 \cdot \sqrt{2} \cdot b(y2) \cdot R \cdot T} \cdot \left[\left[\frac{2 \cdot [(1 - y2) \cdot a_{12}(k12) + y2 \cdot a_2]}{a(y2, k12)} - \frac{b_2}{b(y2)} \right] \cdot \ln\left[\frac{Vvap(y2, k12, P) + (1 + \sqrt{2}) \cdot b(y2)}{Vvap(y2, k12, P) + (1 - \sqrt{2}) \cdot b(y2)} \right] \right] \right]$$

$$i := 0..4$$

$$v1_s := 656.3 10^{-6} \frac{m^3}{mol}$$

Guess

$$k12 := 0.01$$

$$P0_i :=$$

148.035atm
246.725atm
246.725atm
246.725atm
266.463atm

$$y0_i :=$$

0.0009
0.0017
0.0027
0.0037
0.0048

Given

$$\sum_{i=0}^{4} \left[\frac{P1_{sat}}{P0_i} \cdot \frac{1}{\phi(y0_i, k12, P0_i)} \cdot \exp\left[\frac{v1_s \cdot (P0_i - P1_{sat})}{R \cdot T} \right] - y0_i \right]^2 = 0$$

$$k12 := \text{Find}(k12)$$

$$k_{12} := k12$$

$$R := 8.314 \frac{J}{\text{mol} \cdot K} \qquad\qquad MPa := 10^6 Pa$$

$$k1(T) := 0.378893 + 1.4897153\omega_1 - 0.26992\omega_1^2$$

$$a_1(T) := \frac{0.457235R^2 \cdot T_{c1}^2}{P_{c1}} \cdot \left[1 + k1(T) \cdot \left[1 - \left(\frac{T}{T_{c1}}\right)^{0.5}\right]\right]^2 \qquad b_1 := \frac{0.077796R \cdot T_{c1}}{P_{c1}}$$

$$k2(T) := 0.378893 + 1.4897153\omega_2 - 0.26992\omega_2^2$$

$$a_2(T) := \frac{0.457235R^2 \cdot T_{c2}^2}{P_{c2}} \cdot \left[1 + k2(T) \cdot \left[1 - \left(\frac{T}{T_{c2}}\right)^{0.5}\right]\right]^2 \qquad b_2 := \frac{0.077796R \cdot T_{c2}}{P_{c2}}$$

$$a_{12}(T) := \left(a_1(T) \cdot a_2(T)\right)^{0.5} \cdot \left(1 - k_{12}\right)$$

$$a(y2, T) := (1 - y2)^2 \cdot a_1(T) + 2 \cdot (1 - y2) \cdot y2 \cdot a_{12}(T) + y2^2 \cdot a_2(T)$$

$$b(y2) := (1 - y2) \cdot b_1 + y2 \cdot b_2$$

$$A(y2, P, T) := \frac{a(y2, T) \cdot P}{(RT)^2} \qquad\qquad B(y2, P, T) := \frac{b(y2) \cdot P}{R \cdot T}$$

$$Z(y2, P, T) := \text{polyroots} \begin{pmatrix} -A(y2, P, T) \cdot B(y2, P, T) + B(y2, P, T)^2 + B(y2, P, T)^3 \\ A(y2, P, T) - 3 \cdot B(y2, P, T)^2 - 2 \cdot B(y2, P, T) \\ -1 + B(y2, P, T) \\ 1 \end{pmatrix}$$

$$Z(y2, P, T) := \begin{vmatrix} Z1 \leftarrow Z(y2, P, T) \\ \text{for } i \in 0..2 \\ \quad Z1_i \leftarrow 0 \text{ if } \text{Im}(Z1_i) \neq 0 \\ Z1 \leftarrow \text{sort}(Z1) \\ Z1_0 \leftarrow Z1_2 \text{ if } |Z1_0| < 10^{-5} \\ Z1_2 \leftarrow Z1_0 \text{ if } |Z1_2| < 10^{-5} \\ Z1 \end{vmatrix}$$

set complex roots to zero

sort the roots

set values of any complex root

to the value of the real root

$$Z(y2, P, T) := Z(y2, P, T)_2$$

$$Vvap(y2, P, T) := \frac{Z(y2, P, T) \cdot R \cdot T}{P}$$

$$\phi(y2, P, T) := \exp\left[\frac{b_2}{b(y2)} \cdot (Z(y2, P, T) - 1) - \ln(Z(y2, P, T) - B(y2, P, T)) \dots \right.$$
$$\left. + \frac{-a(y2, T)}{2 \cdot \sqrt{2} \cdot b(y2) \cdot R \cdot T} \cdot \left[\left[\frac{2 \cdot \left[(1 - y2) \cdot a_{12}(T) + y2 \cdot a_2(T)\right]}{a(y2, T)} - \frac{b_2}{b(y2)}\right] \cdot \ln\left[\frac{Vvap(y2, P, T) + \left(1 + \sqrt{2}\right) \cdot b(y2)}{Vvap(y2, P, T) + \left(1 - \sqrt{2}\right) \cdot b(y2)}\right]\right]\right]$$

$$P := 1MPa, 2MPa .. 30MPa \qquad\qquad y := 0.01$$

Given

$$i := 0 .. 30 \qquad y = \frac{P1_{sat}}{P} \cdot \frac{1}{\phi(y, P, T)} \cdot \exp\left[\frac{v1_s \cdot \left(P - P1_{sat}\right)}{R \cdot T}\right]$$

$F(y, P, T) =$

$F(y, P, T) := Find(y)$

$y1_i :=$

0.0009
0.0017
0.0032
0.0027
0.0048

0
0
0
$1.867 \cdot 10^{-15}$
$1.035 \cdot 10^{-14}$
$6.42 \cdot 10^{-14}$
$4.422 \cdot 10^{-13}$
$3.371 \cdot 10^{-12}$
$2.817 \cdot 10^{-11}$
$2.519 \cdot 10^{-10}$
$2.282 \cdot 10^{-9}$
$1.904 \cdot 10^{-8}$
$1.301 \cdot 10^{-7}$
$6.684 \cdot 10^{-7}$
$2.536 \cdot 10^{-6}$
...

$P1_i :=$

148.035
246.725
246.725
246.725
266.463

$F(y, P, T)$

$y1_i$

$$\frac{P}{10^5}, P1_i$$
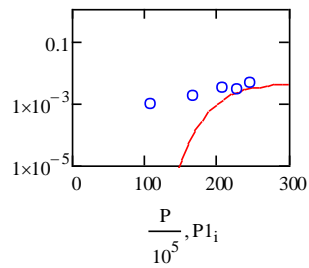
4. Solubilities of AKD in supercritical carbon dioxide based on PREOS at 353.15K

$$1 = \text{Carbon Dioxide}$$
$$T := 353.15K$$
$$2 = \text{AKD}$$

$$R := 8.314\frac{J}{mol \cdot K} \qquad MPa := 10^6 Pa \qquad bar := 10^5 Pa$$

$$T_{c1} := 304.12K \qquad P_{c1} := 73.74 bar \qquad \omega_1 := 0.225$$

$$T_{c2} := 900.95K \qquad P_{c2} := 7.54 bar \qquad \omega_2 := 1.91$$

$$P1_{sat} := \frac{\left(10^3 \cdot \exp\left(8.5759 - \frac{95.5979}{\frac{T}{100 \cdot K}} - 3.744\ln\left(\frac{T}{100K}\right) - 0.5834\frac{T}{100K}\right)\right)Pa}{504} \to 2.0860929004004097295e-5 Pa$$

$$k1 := 0.378893 + 1.4897153\omega_1 - 0.26992\omega_1^2$$

$$a1 := \frac{0.457235R^2 \cdot T_{c1}^2}{P_{c1}} \cdot \left[1 + k1\cdot\left[1 - \left(\frac{T}{T_{c1}}\right)^{0.5}\right]\right]^2 \qquad b1 := \frac{0.077796R \cdot T_{c1}}{P_{c1}}$$

$$k2 := 0.378893 + 1.4897153\omega_2 - 0.26992\omega_2^2$$

$$a2 := \frac{0.457235R^2 \cdot T_{c2}^2}{P_{c2}} \cdot \left[1 + k2\cdot\left[1 - \left(\frac{T}{T_{c2}}\right)^{0.5}\right]\right]^2 \qquad b2 := \frac{0.077796R \cdot T_{c2}}{P_{c2}}$$

$$a_{12}(k12) := \left(a_1 \cdot a_2\right)^{0.5} \cdot (1 - k12)$$

$$a(y2, k12) := (1 - y2)^2 \cdot a_1 + 2 \cdot (1 - y2) \cdot y2 \cdot a_{12}(k12) + y2^2 \cdot a_2 \qquad b(y2) := (1 - y2) \cdot b_1 + y2 \cdot b_2$$

$$A(y2, k12, P) := \frac{a(y2, k12) \cdot P}{(R\,T)^2} \qquad B(y2, P) := \frac{b(y2) \cdot P}{R \cdot T}$$

$$Z(y2, k12, P) := polyroots\left(\begin{array}{c} -A(y2, k12, P) \cdot B(y2, P) + B(y2, P)^2 + B(y2, P)^3 \\ A(y2, k12, P) - 3 \cdot B(y2, P)^2 - 2 \cdot B(y2, P) \\ -1 + B(y2, P) \\ 1 \end{array}\right)$$

166

$$\underset{\sim}{\text{Z}}(y2,k12,P) := \begin{vmatrix} Z1 \leftarrow Z(y2,k12,P) \\ \text{for } i \in 0..2 \\ \quad Z1_i \leftarrow 0 \text{ if } \text{Im}\left(Z1_i\right) \neq 0 \\ Z1 \leftarrow \text{sort}(Z1) \\ Z1_0 \leftarrow Z1_2 \text{ if } \left|Z1_0\right| < 10^{-5} \\ Z1_2 \leftarrow Z1_0 \text{ if } \left|Z1_2\right| < 10^{-5} \\ Z1 \end{vmatrix}$$

set complex roots to zero

sort the roots

set values of any complex root

to the value of the real root

$$\underset{\sim}{\text{Z}}(y2,k12,P) := \text{Z}(y2,k12,P)_2$$

$$\underset{\sim\sim\sim}{\text{Vvap}}(y2,k12,P) := \frac{Z(y2,k12,P) \cdot R \cdot T}{P}$$

$$\underset{\sim}{\phi}(y2,k12,P) := \exp\left[\frac{b_2}{b(y2)} \cdot (Z(y2,k12,P) - 1) - \ln(Z(y2,k12,P) - B(y2,P)) \dots \right.$$
$$\left. + \frac{-a(y2,k12)}{2 \cdot \sqrt{2} \cdot b(y2) \cdot R \cdot T} \cdot \left[\left[\frac{2 \cdot \left[(1 - y2) \cdot a_{12}(k12) + y2 \cdot a_2 \right]}{a(y2,k12)} - \frac{b_2}{b(y2)} \right] \cdot \ln\left[\frac{Vvap(y2,k12,P) + \left(1 + \sqrt{2}\right) \cdot b(y2)}{Vvap(y2,k12,P) + \left(1 - \sqrt{2}\right) \cdot b(y2)} \right] \right] \right]$$

$$i := 0..4 \qquad\qquad \underset{\sim\sim\sim}{v1_s} := 656.3 \cdot 10^{-6} \frac{m^3}{mol}$$

Guess

$$P0_i := \qquad\qquad\qquad y0_i := \qquad\qquad\qquad \underset{\sim\sim\sim\sim}{k12} := 0.01$$

148.035atm
256.594atm
266.463atm
275.332atm
246.725atm

0.0009
0.0017
0.0027
0.0037
0.0048

Given

$$\sum_{i=0}^{4} \left[\frac{P1_{sat}}{P0_i} \cdot \frac{1}{\phi\left(y0_i, k12, P0_i\right)} \cdot \exp\left[\frac{v1_s \cdot \left(P0_i - P1_{sat}\right)}{R \cdot T} \right] - y0_i \right]^2 = 0$$

$$\underset{\sim\sim\sim\sim}{k12} := \text{Find}(k12)$$

$$\boxed{k12 = -0.1779}$$

$$\underset{\sim\sim\sim}{k_{12}} := k12$$

$$\underset{\sim}{R} := 8.314 \frac{J}{mol \cdot K} \qquad\qquad \underset{\sim\sim\sim\sim}{MPa} := 10^6 Pa$$

$$k1(T) := 0.378893 + 1.4897153\omega_1 - 0.26992\omega_1^2$$

$$a_1(T) := \frac{0.457235R^2 \cdot T_{c1}^2}{P_{c1}} \cdot \left[1 + k1(T) \cdot \left[1 - \left(\frac{T}{T_{c1}}\right)^{0.5}\right]\right]^2 \qquad b_1 := \frac{0.077796R \cdot T_{c1}}{P_{c1}}$$

$$k2(T) := 0.378893 + 1.4897153\omega_2 - 0.26992\omega_2^2$$

$$a_2(T) := \frac{0.457235R^2 \cdot T_{c2}^2}{P_{c2}} \cdot \left[1 + k2(T) \cdot \left[1 - \left(\frac{T}{T_{c2}}\right)^{0.5}\right]\right]^2 \qquad b_2 := \frac{0.077796R \cdot T_{c2}}{P_{c2}}$$

$$a_{12}(T) := \left(a_1(T) \cdot a_2(T)\right)^{0.5} \cdot \left(1 - k_{12}\right)$$

$$a(y2,T) := (1 - y2)^2 \cdot a_1(T) + 2 \cdot (1 - y2) \cdot y2 \cdot a_{12}(T) + y2^2 \cdot a_2(T)$$

$$b(y2) := (1 - y2) \cdot b_1 + y2 \cdot b_2$$

$$A(y2,P,T) := \frac{a(y2,T) \cdot P}{(R\,T)^2} \qquad\qquad B(y2,P,T) := \frac{b(y2) \cdot P}{R \cdot T}$$

$$Z(y2,P,T) := \text{polyroots} \begin{pmatrix} -A(y2,P,T) \cdot B(y2,P,T) + B(y2,P,T)^2 + B(y2,P,T)^3 \\ A(y2,P,T) - 3 \cdot B(y2,P,T)^2 - 2 \cdot B(y2,P,T) \\ -1 + B(y2,P,T) \\ 1 \end{pmatrix}$$

$$Z(y2,P,T) := \begin{vmatrix} Z1 \leftarrow Z(y2,P,T) \\ \text{for } i \in 0..2 \\ \quad Z1_i \leftarrow 0 \text{ if } \text{Im}\left(Z1_i\right) \neq 0 \\ Z1 \leftarrow \text{sort}(Z1) \\ Z1_0 \leftarrow Z1_2 \text{ if } \left|Z1_0\right| < 10^{-5} \\ Z1_2 \leftarrow Z1_0 \text{ if } \left|Z1_2\right| < 10^{-5} \\ Z1 \end{vmatrix}$$

set complex roots to zero

sort the roots

set values of any complex root

to the value of the real root

$$Z(y2,P,T) := Z(y2,P,T)_2$$

168

$$Vvap(y2, P, T) := \frac{Z(y2, P, T) \cdot R \cdot T}{P}$$

$$\phi(y2, P, T) := \exp\left[\frac{b_2}{b(y2)} \cdot (Z(y2, P, T) - 1) - \ln(Z(y2, P, T) - B(y2, P, T)) \ldots \right.$$
$$\left. + \frac{-a(y2, T)}{2 \cdot \sqrt{2} \cdot b(y2) \cdot R \cdot T} \cdot \left[\left[\frac{2 \cdot \left[(1 - y2) \cdot a_{12}(T) + y2 \cdot a_2(T)\right]}{a(y2, T)}\right] - \frac{b_2}{b(y2)}\right] \cdot \ln\left[\frac{Vvap(y2, P, T) + (1 + \sqrt{2}) \cdot b(y2)}{Vvap(y2, P, T) + (1 - \sqrt{2}) \cdot b(y2)}\right]\right]$$

$$P := 1MPa, 2MPa \ldots 30MPa \qquad\qquad y := 0.01$$

Given

$$y = \frac{P1_{sat}}{P} \cdot \frac{1}{\phi(y, P, T)} \cdot \exp\left[\frac{v1_s \cdot (P - P1_{sat})}{R \cdot T}\right]$$

$$f(y, P, T) := Find(y)$$

$$P1_i := \qquad\qquad i := 0..30$$

108.551
167.773
207.249
226.987
246.725

$F(y, P, T) =$

0
0
0
$2.337 \cdot 10^{-15}$
$1.111 \cdot 10^{-14}$
$5.756 \cdot 10^{-14}$
$3.208 \cdot 10^{-13}$
$1.905 \cdot 10^{-12}$
$1.19 \cdot 10^{-11}$
$7.681 \cdot 10^{-11}$
$4.973 \cdot 10^{-10}$
$3.095 \cdot 10^{-9}$
$1.756 \cdot 10^{-8}$
$8.632 \cdot 10^{-8}$
$3.541 \cdot 10^{-7}$
...

$$y1_i :=$$

0.0009
0.0017
0.0032
0.0027
0.0048

169
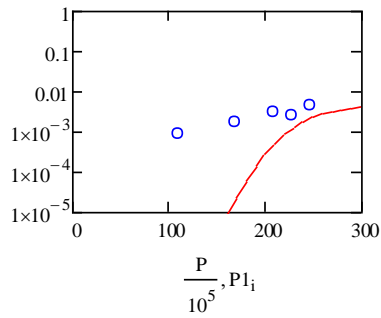
Appendix B: CO$_2$ density

Temp (C)/Pressure (bar)	15	16	17	18	19	20	21	22	23
40	102.95	101.85	100.76	99.672	98.581	97.49	96.717	95.944	95.171
50	167.4	162.04	156.68	151.32	145.96	140.6	138.94	137.28	135.62
60	832.2	822.3	812.4	802.5	792.6	782.7	763.76	310.54	293.16
70	850.85	842.4	833.95	825.5	817.05	808.6	787.07	765.54	744.01
80	865.4	857.86	850.32	842.78	835.24	827.7	815.1	802.5	789.9
90	877.7	870.8	863.9	857	850.1	843.2	833.31	823.42	813.53
100	888.4	881.98	875.56	869.14	862.72	856.3	847.82	839.34	830.86
110	896.55	890.41	884.27	878.12	871.98	865.84	857.92	849.99	842.07
120	904.7	898.84	892.97	887.11	881.24	875.38	868.01	860.64	853.28
130	912.85	907.26	901.68	896.09	890.51	884.92	878.11	871.3	864.48
140	921	915.69	910.38	905.08	899.77	894.46	888.2	881.95	875.69
150	929.15	924.12	919.09	914.06	909.03	904	898.3	892.6	886.9
160	935.07	930.18	925.3	920.41	915.53	910.64	905.15	899.66	894.16
170	940.99	936.25	931.51	926.76	922.02	917.2	912	906.71	901.43
180	946.91	942.31	937.71	933.12	928.52	923.92	918.84	913.77	908.69
190	952.83	948.38	943.92	939.47	935.01	930.56	925.69	920.82	915.96
200	958.75	954.44	950.13	945.82	941.51	937.2	932.54	927.88	923.22
210	963.51	959.28	955.06	950.83	946.61	942.38	937.84	933.3	928.76
220	968.27	964.13	959.99	955.84	951.7	947.56	943.14	938.72	934.3
230	973.03	968.97	964.91	960.86	956.8	952.74	948.44	944.14	939.84
240	977.79	973.82	969.84	965.87	961.89	957.92	953.74	949.56	945.38
250	982.55	978.66	974.77	970.88	966.99	963.1	959.05	954.98	950.92
260	986.51	982.69	978.87	975.06	971.24	967.42	963.44	959.46	955.48
270	990.47	986.72	982.98	979.23	975.49	971.74	967.84	963.94	960.04

280	994.43	990.76	987.08	983.41	979.73	976.06	972.24	968.42	964.6
290	998.39	994.79	991.19	987.58	983.98	980.38	976.64	972.9	969.16
300	1002.4	998.82	995.29	991.76	988.23	984.7	981.04	977.38	973.72

Temp (C)/ Pressure (bar)	24	25	26	27	28	29	30	31	32
40	94.398	93.625	92.852	92.079	91.306	90.533	89.76	89.16	88.56
50	133.96	132.3	130.64	128.98	127.32	125.66	124	122.9	121.8
60	275.78	258.4	241.02	223.64	206.26	188.88	171.5	169.28	167.06
70	722.48	700.95	679.42	657.89	636.36	274.38	266.5	259.65	252.8
80	777.3	764.7	752.1	739.5	726.9	714.3	701.7	659.32	616.94
90	803.64	793.75	783.86	773.97	764.08	754.19	744.3	718.43	692.56
100	822.38	813.9	805.42	796.94	788.46	779.98	771.5	757.22	742.94
110	834.14	826.22	818.3	810.37	802.45	794.52	786.6	773.84	761.08
120	845.91	838.54	831.17	823.8	816.44	809.07	801.7	790.46	779.23
130	857.67	850.86	844.05	837.24	830.42	823.61	816.8	807.09	797.37
140	869.44	863.18	856.92	850.67	844.41	838.16	831.9	823.71	815.52
150	881.2	875.5	869.8	864.1	858.4	852.7	847	840.33	833.66
160	888.67	883.18	877.69	872.2	866.7	861.21	855.72	849.37	843.02
170	896.14	890.86	885.58	880.29	875.01	869.72	864.44	858.41	852.38
180	903.62	898.54	893.46	888.39	883.31	878.24	873.16	867.45	861.74
190	911.09	906.22	901.35	896.48	891.62	886.75	881.88	876.49	871.1
200	918.56	913.9	909.24	904.58	899.92	895.26	890.6	885.53	880.46
210	924.22	919.68	915.14	910.6	906.06	901.52	896.98	892.07	887.15
220	929.88	925.46	921.04	916.62	912.2	907.78	903.36	898.6	893.84
230	935.54	931.24	926.94	922.64	918.34	914.04	909.74	905.14	900.54
240	941.2	937.02	932.84	928.66	924.48	920.3	916.12	911.67	907.23
250	946.86	942.8	938.74	934.68	930.62	926.56	922.5	918.21	913.92
260	951.5	947.52	943.54	939.56	935.58	931.6	927.62	923.43	919.23
270	956.14	952.24	948.34	944.44	940.54	936.64	932.74	928.64	924.54
280	960.78	956.96	953.14	949.32	945.5	941.68	937.86	933.86	929.86
290	965.42	961.68	957.94	954.2	950.46	946.72	942.98	939.07	935.17
300	970.06	966.4	962.74	959.08	955.42	951.76	948.1	944.29	940.48

Temp (C)/ Pressure (bar)	33	34	35	36	37	38	39	40
40	87.96	87.36	86.76	86.16	85.56	84.96	84.36	83.76
50	120.7	119.6	118.5	117.4	116.3	115.2	114.1	113
60	164.84	162.62	160.4	158.18	155.96	153.74	151.52	149.3
70	245.95	239.1	232.25	225.4	218.55	211.7	204.85	198
80	574.56	532.18	489.8	447.42	405.04	362.66	320.28	277.9
90	666.69	640.82	614.95	589.08	563.21	537.34	511.47	485.6
100	728.66	714.38	700.1	685.82	671.54	657.26	642.98	628.7
110	748.33	735.57	722.81	710.05	697.29	684.54	671.78	659.02
120	767.99	756.76	745.52	734.28	723.05	711.81	700.58	689.34
130	787.66	777.94	768.23	758.52	748.8	739.09	729.37	719.66
140	807.32	799.13	790.94	782.75	774.56	766.36	758.17	749.98
150	826.99	820.32	813.65	806.98	800.31	793.64	786.97	780.3
160	836.67	830.32	823.97	817.62	811.27	804.92	798.57	792.22
170	846.35	840.32	834.29	828.26	822.23	816.2	810.17	804.14
180	856.03	850.32	844.61	838.9	833.19	827.48	821.77	816.06
190	865.71	860.32	854.93	849.54	844.15	838.76	833.37	827.98
200	875.39	870.32	865.25	860.18	855.11	850.04	844.97	839.9
210	882.24	877.32	872.41	867.5	862.58	857.67	852.75	847.84
220	889.09	884.33	879.57	874.81	870.05	865.3	860.54	855.78
230	895.93	891.33	886.73	882.13	877.53	872.92	868.32	863.72
240	902.78	898.34	893.89	889.44	885	880.55	876.11	871.66
250	909.63	905.34	901.05	896.76	892.47	888.18	883.89	879.6
260	915.04	910.84	906.65	902.46	898.26	894.07	889.87	885.68
270	920.45	916.35	912.25	908.15	904.05	899.96	895.86	891.76
280	925.85	921.85	917.85	913.85	909.85	905.84	901.84	897.84
290	931.26	927.36	923.45	919.54	915.64	911.73	907.83	903.92
300	936.67	932.86	929.05	925.24	921.43	917.62	913.81	910

172

Appendix C: Symbols and Notations for Chapter Two

Nomenclature	
a, b	PREOS mixture parameters
A, B	dimensionless parameters of EOS
F	fugacity
$k_{i,j}$	binary interaction parameters
P	pressure
P^{vap}	vapor pressure of AKD
R	gas constant
T	temperature
v	molar volume of the SCF-AKD mixture
y	mole fraction
Z	compressibility factor
Greek letters	
α	interaction parameter
ρ	density
ϕ	fugacity coefficient
ω	acentric factor
Subscripts	
AKD	alkyl ketene dimer
c	critical
cal	calculated
exp	experimental
i, j	component index
m	mixture
r	reduced
1	scCO$_2$
2	AKD
Superscripts	
vap	vapor
s	solute
sup	supercritical
Abbreviations	
AKD	alkyl ketene dimer
EOS	equation of state
GCEM	group contribution estimation method
MW	molecular weight
PREOS	Peng-Robinson equation of state
scCO$_2$	supercritical carbon dioxide
SCF	supercritical fluid

VITAE

Kolawole Adenekan

Address: 228 CR 235, Abbeville, MS 38601

Mobile: +1 362-228-4114

E-mail: kola.adenekan@gmail.com

Education

- **PhD:** *Chemical Engineering,* University of Mississippi*, Oxford, Mississippi, (2015 – 2019).*

  Dissertation: **"Hydrophobization of Cellulose-based Fibers for Packaging Applications with Alkyl Ketene Dimers (AKD) and Food-grade Waxes via Supercritical Impregnation with Carbon Dioxide – Experimental and Thermodynamic Modeling Approaches".**

- **M.S.** (partially completed): *Chemical Engineering,* University of Mississippi, *Oxford, Mississippi, (2014 – 2015).*

- **B.Sc.:** *Chemical Engineering, Process Design,* University of Tehran, *Tehran, Iran, (2004 – 2009).*

  Thesis: "Implosion Demolition of High-rise Buildings".

JOURNAL PUBLICATIONS (PUBLISHED, UNDER REVIEW OR IN PREPARATION)

1. **K. Adenekan** and B. Hutton-Prager, Sticky Hydrophobic Behavior of Cellulose Substrates Impregnated with Alkyl Ketene Dimer (AKD) via Sub- and Supercritical Carbon Dioxide, Colloids Surfaces A Physicochem. Eng. Asp. 560 (2018)

2. **K. Adenekan** and B. Hutton-Prager "Thermodynamic Models of Alkyl Ketene Dimer Dissolved in Supercritical Carbon Dioxide". (Under review)

3. **K. Adenekan** and B. Hutton-Prager*. "High-pressure Impregnation and Annealing of Cellulose Fibers with Food-grade Waxes: Hydrophobic and Mechanical properties. (To be submitted for publication)

4. **Kolawole Adenekan** and Brenda Hutton-Prager*. "Fabrication of Hydrophobic Surfaces on Cellulose Fibers via Heat Treatment-Assisted Supercritical Impregnation of Vegetable Wax Natural". (In preparation)

DEPARMENTAL/SEMINAR RESENTATIONS

1. **K. Adenekan**. "Sticky hydrophobic surfaces", University of Mississippi, graduate school 3-minute Thesis, 23th, October 2018.

2. **K. Adenekan** "Use of Hydrocarbon Screen Spill Screening Model to assess gasoline vertical migration and spreading in vadose upon ozone remediation", University of Mississippi, Original Research Proposal, 10th, May 2017

3. **K. Adenekan** "Hydrophobization of Cellulose-based Fibers for Packaging Applications with Alkyl Ketene Dimers (AKD) and Food-grade Waxes via Supercritical Impregnation **with** Carbon Dioxide – Experimental and Thermodynamic Modeling Approaches", University of Mississippi, Dissertation Prospectus, 17th, November 2017

175

4. **K. Adenekan** "Study of paper substrates impregnated with supercritical CO_2 in alkyl ketene dimers (AKD) for paper and packaging application", University of Mississippi, chemical engineering department, graduate seminar, 14th October 2016.

5. **K. Adenekan** "Hydrophobization of paper substrates with alkyl ketene dimers (AKD) via sub/supercritical CO_2 for packaging applications", University of Mississippi, chemical engineering department, graduate seminar, 10th February 2016.

6. **K. Adenekan**. "Intelligent coatings for package applications", University of Mississippi, graduate school 3-minute Thesis, 20th, November 2016.

7. **K. Adenekan**. "Selective flocculation and dispersion of Hematite Ore", Michigan Tech. University, 13th December 2014.

CONFERENCE PRESENTATIONS

1. **B. Hutton-Prager*** and K. Adenekan. "High Pressure Impregnation of Alkyl Ketene Dimers (AKD) in Cellulose Substrates, Creating Novel Sticky Hydrophobic Surfaces", AlChE, Orlando, FL. 2019.

2. **K. Adenekan** and Brenda Hutton-Prager*. "Coating of Cellulose Fibers with Alkyl Ketene Dimers (AKD) for Hydrophobic Development and Study of Its Coating Mechanism using Supercritical Technique". (PaperCon, Charlotte, (2018)**.**

WORK EXPERIENCE

♦ **Research Assistant –** Chemical Engineering Dept., The University of Mississippi (2015-2019)

- **Teaching Assistant –** Chemical Engineering Dept., The University of Mississippi (2015-2019)

- **Tutorial Support Staff –** Student-Athlete Support Center, The University of Mississippi (2018)

- **Research Assistant –** Chemical Engineering Dept., Michigan Tech University (2014-2015)

- *Logistics and Distribution Manager–* Olowo Ijeun Woods, Abeokuta, Nigeria (2011-2013)

EDITORIAL BOARD MEMBER /REVIWER

- Journal of Colloid and Surface Science

AWARDS/SCHOLARSHIPS AND GRANTS

- Fulfilling the Legacy *Scholarship (*2018 – 2019) – National Society of Black Engineers

- Summer Graduate Research Assistantship Program - 2018. *University of Mississippi, Oxford, MS*

- Fulfilling the Legacy *Scholarship (*2016 – 2017) – National Society of Black Engineers

- BCA/Major/Fellows Scholarship (2016 – 2017) – National Society of Black Engineers

- ORSP Grant: Graduate Student Council Research Grants Program - 2016. *University of Mississippi, Oxford, MS*

Professional MEMBERSHIP

- ♦ National Society of Black Engineers

- ♦ Society of Manufacturing Engineers

- ♦ TAPPI – PaperCon

- ♦ Association of Plastic Engineers